CONSTITUTIVE AND MACHINE LEARNING BASED MICROSTRUCTURE AND MECHANICAL PROPERTIES PREDICTION MODELS FOR THIXO EXTRUDED Al/Si ALLOYS

A thesis submitted in partial fulfilment of the requirements for the award of the Degree of

DOCTOR OF PHILOSOPHY
in
MECHANICAL ENGINEERING

Abeyram M Nithin
(Roll No: 716127)

Supervisor
Dr. M. Joseph Davidson
and
Co-Supervisor
Prof. C. S. P Rao

DEPARTMENT OF MECHANICAL ENGINEERING
NATIONAL INSTITUTE OF TECHNOLOGY,
WARANGAL (TS) - 506004, INDIA.
2022

CERTIFICATE

This is to certify that the dissertation work entitled **"Constitutive and Machine Learning based Microstructure and Mechanical Properties Prediction Models for Thixo Extruded Al/Si Alloys"**, which is being submitted by **Mr. Abeyram M Nithin** (Roll No. 716127), is a bonafide work submitted to the Department of Mechanical Engineering, National Institute of Technology, Warangal in partial fulfillment of the requirement for the award of the degree of **Doctor of Philosophy in Mechanical Engineering.**

To the best of our knowledge, the work incorporated in this thesis has not been submitted elsewhere for the award of any degree.

Dr. M. Joseph Davidson
Supervisor
Department of Mechanical Engineering
National Institute of Technology
Warangal- 506004

Prof. C. S. P Rao
Co-supervisor
Director
National Institute of Technology
Tadepalligudem-534102

Prof. Adepu Kumar
Head
Department of Mechanical Engineering
National Institute of Technology
Warangal- 506004

Dedicated

To

My beloved parents

APPROVAL SHEET

This Thesis entitled **"Constitutive and Machine Learning based Microstructure and Mechanical Properties Prediction Models for Thixo Extruded Al/Si Alloys"**, by **Abeyram M Nithin** is approved for the **Degree of Doctor Philosophy**

Examiners

Supervisor	**Co-supervisor**
Dr. M. J. Davidson	**Prof. C. S. P Rao**
(Associate Professor. MED)	**(Professor. MED)**

Chairman

Prof. A. Kumar, MED, NIT
WARANGAL

DECLARATION

This is to certify that the work presented in the thesis entitled **"Constitutive and Machine Learning based Microstructure and Mechanical Properties Prediction Models for Thixo Extruded Al/Si Alloys"** is a bonafide work done by me under the supervision of Dr M. J. Davidson and Prof. C. S. P Rao, and was not submitted elsewhere for the award of any degree.

I declare that this written submission represents my ideas in my own words and where others' ideas or words have been included, I adequately cited and referenced the sources. I also declare that I have adhered to all principles of academic honesty and integrity and have not misrepresented or fabricated or falsified any idea/data/fact/source in my submission. I understand that any violation of the above will be a cause for disciplinary action by the Institute and can also evoke penal action from the sources which have thus not been properly cited or from whom proper permission has not been taken when needed.

Abeyram M Nithin

Roll No.: 716127

Date: 03-01-2022

ACKNOWLEDGMENT

I would like to express my sincere thanks and gratitude to my supervisor(s), Dr. M. J. Davidson Mechanical Engineering Department, National Institute of Technology, Warangal and Prof. C. S. P Rao, Director, National Institute of Technology, Andhra Pradesh, for his continuous guidance, support, enthusiasm, and motivation in my Ph.D. research work.

Besides my supervisor, I would like to thank the rest of my Doctoral scrutiny committee: Prof. N. Selvaraj and Prof. V. Suresh Babu (Mechanical Engineering Department), and Dr.Asit Kumar Khanra (Materials and Metallurgical Engineering Department), for their insightful comments and encouragement, but also for the hard questions which incented me to widen my research from various perspectives.

I wish to sincerely thank university authorities, Prof. N.V. RAMANA RAO, Director, National Institute of Technology, Warangal and other top officials who gave me an opportunity to carry out research work.

I also sincerely thank Prof. Adepu Kumar, Head of the Department of Mechanical Engineering, National Institute of Technology, Warangal for his continuous support towards carrying out research work. I would like to extend my thanks to all the faculty members in the Department of Mechanical Engineering Department for their valuable suggestions and encouragement. I am also thankful to all the supporting and technical staff of the Department of Mechanical Engineering who has directly or indirectly helped during the course of my work.

I would like to express my sincere thanks to my fellow lab mates Dr. K. Bharath, Dr. V. Seetharam, Dr. D.T. Sarath Chandra, Mr. R. Rajasekhar, Mr. A. P. Murugesan and Mr. Harikrishna for their wholehearted support during the entire tenure for the successful completion of the work.

I owe a lot to my beloved friends Mr. B. Venkatesh, Mr. Santanu Saisdharan, Mr. K Madhu Kishore Raghunath and Mr. M. Siva Sankar who encouraged and extended their helping arms towards me at every stage of my personal and academic life and longed to see this achievement come true.

Words are inadequate to express my gratitude to all my family members especially S. Jeya (Mother), R. Murugesan (Father), who constantly stood as a source of happiness, encouragement, confidence and untiring support.

(Abeyram M Nithin)

ABSTRACT

Thixoforming is a well-known material processing technology that involves the creation of materials at temperatures ranging from solidus to liquidus. One of the requirements for this process is that the feedstock material's microstructure contains solid, near-globular grains in a liquid matrix and a broad solidus-to-liquidus transition range. Powder Metallurgy (P/M) is a near-net-shaped material processing route that compacts and sinters metal powders into finished products. When produced in this manner, the necessity for final machining is considerably reduced or eliminated. P/M techniques using aluminium alloys are particularly intriguing since they allow for the creation of custom-made, high-strength goods.

In this thesis work, hot compaction studies of Aluminium alloys with different Si and Mg proportions have been studied. Further process parameters like holding temperature and holding time were also optimized. It also deals with the characterization (density, hardness and microstructure) of the alloys before and after extrusion. Extruded samples exhibited improved mechanical properties as compared with the compacted ones. Spheroidal grains were observed throughout the specimens. Dynamic recrystallization of extruded Al-Si-Mg alloys at thixotropic ranges were experienced. Avrami recrystallization model has been used for the calculation and has been compared with the experimentally measured ones. Peak strain, 50% recrystallizes strain, dynamically recrystallized grain size are the parameters that has been identified and validated. DEFORM 2D software has been used to predict the numerically simulated grain size. Larger grains were found at the bottom end of the specimens while the top end had considerably smaller grains. The effect of various Mg/Si ratios on the properties of the Al-Si-Mg alloys and the grain size were investigated. The results revealed that there were significant morphological changes in the silicon structure for Al-Si-Mg alloys beyond certain Mg/Si ratio. In addition to that, the material also started losing the thixotropic property. Further characterization of these alloys before and after extrusion has been performed. The use of computational intelligence techniques to identify the features of interest has been an emerging area in manufacturing process. Deep learning algorithms like FCNN, Unet, Segnet and Resunet++ has been employed to predict the alpha phase present in the optical micrographs. Most of the models were able to predict the alpha phase with varying levels of accuracy.

TABLE OF CONTENTS

LIST OF FIGURES

LIST OF TABLES

Abbreviations and Symbols

Al	Aluminium
CNN	Convolutional neural network
DRV	Dynamic Recovery
DRX	Dynamic Recrystallization
DTA	Differential thermal analysis
EDS	Energy dispersive spectroscopy
FE	Finite Element
FCF	Flow control formed
GB	Grain Boundary
HAZ	Heat Affected Zone
HIP	Hot isostatic pressing
HPDC	High pressure die casting
IM	Ingot metallurgy
MMC	Metal Matrix Composites
OM	Optical microscope
PM	Powder Metallurgy
RSP	Rapid Solidification Processing
RQI	Rheocast Quality Index
SEM	Scanning Electron Microscope
SF	Shape Factor
SFE	Stacking fault energy
SiC	Silicon Carbide
SOD	Slurry on demand
SRX	Static recrystallization
SSF	Semi-Solid Forming
SSM	Semi-Solid metal
SVM	Support vector machines
UTS	Ultimate Tensile strength
WH	Work hardening
α-Al	Alpha aluminium

Chapter 1

Introduction

1.1 Foreword of the present work

Manufacturing industry professionals and researchers have been studying light-weight materials to better understand the nature of processing and the elements that influence their behavior. The primary motivation for this research is to improve the efficiency of light-weight materials in aircraft, automotive, defense, transportation, construction, and architecture. Because of its multiple advantages, including as high strength-to-weight ratio, low density, high hardness, and good corrosion resistance, aluminium alloys have found their applications in various structural and industrial fields[1], [2]. In comparison to other traditional manufacturing processes such as forging, casting, and machining, the pressing-and-sintering powder metallurgy (P/M) process is the most promising technology for developing different engineering components to meet the requirements of the above-mentioned industries with high rates of production at low cost. In general, the P/M process is a very efficient and cost-effective method for creating high-volume components with improved surface polish, precision, near-net shape, and strength. P/M is the best alternative over other traditional manufacturing processes for producing complicated and near-net shape goods with minimal material usage[3].

Due to the constant increase in demand for high-performance parts, the P/M industry has grown fast throughout the decades. The presence of inherent porosity in sintered parts, on the other hand, reduces the mechanical qualities. Thus, the P/M industries usually involve secondary forming processes such as extrusion, rolling, forging, and hot deformation to eradicate maximum porosity. Therefore, investigation of secondary forming of P/M components is the most stimulating new field in metal forming industries due to superior metallurgical and mechanical properties and also because of its flexibility over other conventional production processes. Hot extrusion of light-weight materials is a very new technology to produce near net shaped products with better mechanical properties. Because of the adaptability of applications resulting from the combination of the extruded product shape and the features of light-weight materials, hot extruded light-weight material is widely used. Automotive, aerospace, transportation, electrical, medical, building & construction, domestic, and sports industries all use hot extruded P/M components.

1.2 Introduction to Al and its alloys

Aluminum has proven to be one of the most adaptable and valuable materials found and harvested from the planet from its initial commercial manufacture in 1854. It is the preferred material in various applications related to design and engineering due to its versatility and because of its light weight, formability, corrosion resistance, and high specific strength. It is also the second most commonly used metal after steels. In addition, it is one of the packaging, medicinal, and electrical products that are most easily recyclable uses, as well as the production of motors and automobiles. Almost three-quarters of the aluminum ever manufactured in the world is still in use today because of its recyclable nature. New techniques of employing aluminium in manufacturing processes and manufactured products are the hot topics studied around the world due to its inherent qualities and potential as a sustainable resource When looking at the nature of aluminium studies over the last decades or two, it becomes clear that there have been focused push towards the primary production and related technology development with an increased thrust on the environment and energy efficiency, composite materials, wrought alloys and foundry, and forming technologies [4].

.

The discovery of novel alloys to fill demanding applications aided growth in Al consumption. Future, they were frequently altered to improve processing or to employ them for a wider range of applications. Magnesium, Copper, Silicon, Iron, Nickel, Cobalt, Chromium, Zirconium, Lithium, and Strontium are among the almost 20 alloying elements now available. Specific alloys are made from primary aluminium / secondary metal that has been upgraded with enough primary aluminium[5]. Aluminum and its simpler alloys have high ductility and low flow stress, making cold working possible. As the temperature rises, the strength decreases and the ductility increases. Steel tooling was exposed to heat cycles, minimal stresses, and temperatures below the softening range, even at the operational maximum of roughly 500°C. This last attribute made extrusion much easier, especially for hollow portions, than it was for copper or iron alloys[6]–[10].

1.3 Effects of alloy additions to Al

Alloys are classified according to their presence of important elements and are given 4 digits for wrought alloys and 3 digits for cast alloys. The AA 1000 series classifies aluminium of various purities that has not been intentionally alloyed. The 2000 series of precipitation hardening alloys, which include up to 4.5 percent Cu and produce $CuAl_2$ were the first to be

found (in 1910) and have been widely employed in airplanes[11], [12]. These are substantially stronger than the 6000 series, and deformation and further alloying can make them much stronger. The 3000 series belongs to alloys that have Mn as the most abundant element which is dispersion strengthened by (<0.5 μm) Al_6Mn, while other impurity elements (Fe) may be present [5]. Constituent particles are small particles that form during the solidification process. Fine precipitate of particles in the solid can be manipulated to a degree by annealing at lower temperatures, possibly after homogenizing close to the melting point. The fine precipitate particles do not disintegrate after deformation during annealing recrystallization (SRX). They have an important role in strain hardening and grain size control. Although the 4000 alloys are based on Si and are not commonly utilized the corresponding casting alloys categorized as 300 series are widely used. The above mentioned heat resistant alloys have better qualities than age-hardenable alloys, which expand the particles and have uses in the 300–400°C range. The alloys are classified as 5000 series because they are reinforced by Mg in solid solution up to around 5%. These alloys, like the 3000 and 4000, are not precipitation hardenable and are sometimes referred to as non-heat treatable or non-age hardenable [5]. For this reason, they can be easily welded without the problems of large fluctuations in the amount of precipitation in the heat affected zone (HAZ).Deformation (cold or hot) strengthens these alloys to a significant degree because of Mg solute in comparison with pure Al.

The 6000 series alloys containing Mg (1%) and Si (0.5%) are precipitation hardenable due to the production of Mg_2Si particles. They are not as strong as other age-hardening alloys and are significantly more hot or cold workable since they have the lowest amount of additives. As part of the thermo-mechanical process (TMP), working and precipitation mechanisms are frequently coupled. There can be surplus Si or Mg, along with Cu or other elements, in addition to varying quantities of Mg_2Si.

The 7000 series, which includes alloys containing Zn, Mg, and potentially Cu is known for including the strongest aerospace alloys [13]. There are numerous alloys that do not contain Cu, such as 7004, 7005, and 7039, that have lower strengths but better processing and corrosion resistance for ground-based applications.

1.4 Phase diagrams of Al-Si alloys

As this alloy series (known as A3XX.X) constitutes 95% of the global market for semisolid processing (SSP) technology, the binary Al-Si phase diagram presented in Fig. 1.1 provides a profound knowledge of the essential components of semisolid forming [15]. The

liquid, Al_{FCC}, and silicon phases are all depicted in this phase diagram. At 576.92 ^{o}C, the highest amount of silicon dispersed into the Al_{FCC} phase creating an $\boldsymbol{\alpha}$-phase structure which is estimated to be 1.56 wt%. The solubility of silicon reduces as temperature drops, resulting in the formation of free silicon particles. The predicted microstructure is a mix of $\boldsymbol{\alpha}$ (Al_{FCC} with residual silicon in solid solution) and precipitated alpha silicon particles.

At 576.92 C, the eutectic structure, which is a lamellar mixture of 88.86 percent $\boldsymbol{\alpha}$ plus 11.14 percent silicon, will likewise form, but with a Si concentration of 12.53 wt percent. At ambient temperature, a mixture of 87.5 percent lamellar $\boldsymbol{\alpha}$ plus 12.5 percent silicon is expected due to the low solubility of silicon in the Al_{FCC} structure decaying.

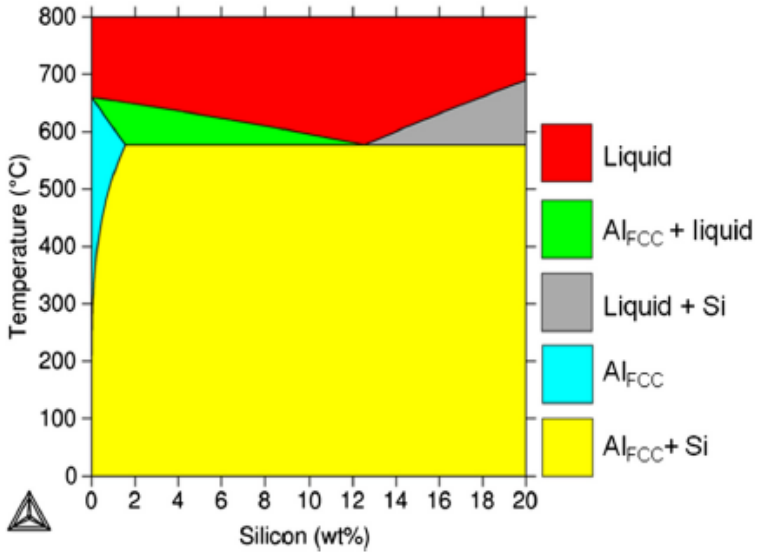

Fig. 1.1: Al-Si phase diagram [15]

1.5 Powder metallurgy (P/M) of Al-alloys

Powder metallurgy (PM) is described as the technique of forming monolithic or solid components from fine powders (typically powders less than 40 μm)[16]. The better qualities that result from the precise and homogeneous microstructure that forms during processing make this approach appealing. The method's versatility in terms of manufacturability and the capability to produce high-quality, complicated, clean net-shaped parts with tight tolerances are also advantages [17]. When compared to the benefits that can be acquired, the procedure is usually cost-effective. Al-Si alloys are the most commonly used alloys among the family of

aluminium alloys next to steel, accounting for over 90% of all aluminium castings [18]. Its supremacy might be traced to the fact that it has wide spread applications in the automobile and aerospace industries. These alloys have great castability, crack resistance, abundance, cost-effectiveness, and a positive technical impact, to name a few advantages. The casting technique, composition, and melt treatment all have an impact on the characteristics of Al-Si alloys.

The automotive industry is P/M aluminum's most lucrative market. However, as compared to other materials, its low wear resistance prevents it from being used in components (such as sprockets) where wear resistance is critical. As a result, numerous P/M aluminium alloys have been created in the past, specifically intended for sintering and reinforced with silicon or hard ceramic particles (e.g. alumina, zirconium silicate, fly ash)[19]. Powder metallurgy alloys have a more uniform microstructure than cast alloys, and the size and number of silicon particles can be better regulated, preventing silicon segregation, which causes undesired wear consequences.

For manufacturing different components, powder metallurgy processing techniques range from pressing and sintering to hot isostatic pressing, powder forging, metal injection molding, and rapid prototyping. Many aluminium castings, extrusions, and screw machine parts that need costly and tedious finishing operations are competitive with powdered aluminium parts. Furthermore, sintered aluminium P/M parts compete with other metal powder components in applications where some of aluminum's appealing physical and mechanical features can be utilized.

1.6 Advantages of P/M over castings

Powder metallurgy's advantages over conventional casting

1) The P/M technique can manufacture goods with a near-net form. The powder mix is fused into a fully hardened piece during sintering of powder compacted pieces.
2) During the casting process, porosity and blowholes develop. The blowholes and porosity are most likely to blame for the localized cracking.
3) During deformation of P/M alloys, shear forces shatter the oxide coatings (produced during the atomization process) covering the particle surfaces of powders, resulting in a well-bonded microstructure.

4) Another benefit of the Al alloys produced by P/M is the microstructure control. In the formation of finer microstructures, P/M can provide more control and consistency. Cast materials have substantially lower mechanical characteristics than products with fine microstructure.
5) During and after sintering, intermetallic phases and precipitates develop, which improve the mechanical characteristics of P/M Al alloys.
6) Furthermore, when compared to standard ingot metallurgy (I/M), P/M technology can be utilized in the refinement of microstructures by adding additives or chemical modifiers, resulting in superior mechanical and corrosion properties.
7) Reduced solidification shrinkage

1.7 Development of porous P/M preforms

Powder metallurgy (PM) has been extensively researched and developed for the production of near-net shape Aluminum alloy components. Because of the potential for cost savings and enhanced fuel efficiency, 'press and sinter' technology has piqued the interest of industries such as automotive for the fabrication of tiny high-performance components.

Powder metallurgy parts are made using a variety of techniques, ranging from high-pressure die compaction to pressureless molding techniques like slip casting. Compaction of powders at high pressures, where consolidation and shaping happen at the same time, is the most common method. P/M products, on the other hand, can be shaped utilizing a variety of low-pressure processes that use binders to keep the shape of the parts while they are sintering. Another option is full density processing, which involves applying high pressure at high temperatures to produce powdered preforms with improved mechanical properties or close to that of wrought forms[20]. There are a variety of compaction processes, but the most common method for producing powdered parts is uniaxial compaction process. The advantages of this process are relatively simple tools requirements and highly economical. The compacting of powder in heated dies can be used to produce huge billets. High temperatures and lengthy dwell durations enable densities greater than 95 percent of full density to be reached at compaction pressures ranging from 1/3 to 1/2 of those required for cold pressing. In most cases, full density is not obtained, and the billet has 3 to 5% porosity. Because the characteristics of hot pressed billets are lowered from those of fully dense material, this porosity limits their application. As

a result, hot consolidated billets are frequently utilized as feed in closed die forging, upset forging, and other deformation procedures that remove residual porosity[21].

Sintering at liquid phase produces components with the desired properties in the press sintering process, in which elemental powders or aluminum powders are mixed with master alloy powders of the desired composition. Rapid solidification of powders and subsequent processing by hot pressing, extrusion, forging, or hot isostatic pressing can improve characteristics further[22].

1.8 Semisolid processing of P/M preforms

The bulk of semi-solid processed aluminium alloys are traditional casting alloys like A356 and A357[23]–[25]. Semi-solid processing of higher strength aluminium aerospace alloys such as the 2000 series, 6000 series, and 7000 series, which are generally wrought, has sparked a lot of interest. The tensile strength and yield strength of conventionally wrought aluminium alloys are close to (or even exceed) the wrought goals when semi-solid treated[26], [27] The problem is the ductility, which is usually only a few percent. The wrought alloys are inherently prone to hot cracking and ductility problems are at least partially associated with them [28].

The development of novel melt treatment and alloy manipulation techniques such as semi-solid metal (SSM) procedures has resulted in a fresh focus on aluminium wrought and foundry alloys casting, owing to renewed interest in aluminium intensive vehicles (AIV) and aluminium space frames for passenger automobiles. Due to high defect content, near-net shape casting and forming procedures such as traditional high pressure die casting (HPDC) are insufficient and must be tailored to create load bearing parts [29], [30]

This innovative approach was found on the assumption that if solidified billets are focused to produce a fine spherical grains, an appropriate mixture of solid spherical particles suspended in a liquid melt can be obtained when the solidified billets are reheated to the required liquid fraction

1.9 Microstructure modelling of hot deformation process

Multiple applications, specific to those in the automobile industry, are increasingly driving the control of extruded aluminium alloy grain shapes. After forging aluminium alloys, larger grain can cause a series of issues, including lower fatigue resistance, poor machinability, and poor surface quality. Controlling grain size is critical for maintaining consistent product

quality and ensuring that cold forming is free of orange peel. Rheocast. The Rheocast Quality Index (RQI) is a measure that aids in quantifying the efficacy of the globularization technique in obtaining semi-solid structure with globular structure. The value becomes RQI for a structure to be globular grain size and should be globule, therefore presenting identical RQI equal to 1 in a perfect semi-solid structure where a grain corresponds to a globule and its shape is a perfect sphere[14]. Microstructural studies on aluminium alloys has been an area of study for many scholars[31], [32]. Using mathematical models to predict the mechanical properties can be useful in optimizing the manufacturing parameters of the process

Because grain size, recrystallization fraction, and dislocation density all affect flow stress, microstructural changes caused by metallurgical processes including phase transformation, dynamic recovery, and dynamic recrystallization (DRX) play an essential role in material flow behavior. Furthermore, the microstructure created by warm processing has an impact on mechanical properties of the formed products. As a result, the link between process parameters and material microstructural change must be quantified. Static recrystallisation (SRX) and DRX as well as grain development during interpass and warming time, are all part of the microstructural evolution during thermo-mechanical processing. To forecast the evolution of microstructure during hot working of die steel, a numerical analysis employing a stiff visco-plastic finite element [33], [34] was done. The flow stress modelling equation was a function of strain, strain rate, and temperature. The Zener-Hollomon parameter was used to calculate the impact of these variables.

During heated extrusion, the microstructure undergoes a complex transformation. Under standard extrusion conditions, i.e. constant ram speed, the distribution of microstructure in the cross section and throughout the length of the extrudates varies significantly. This results in a non-uniform distribution of mechanical characteristics, necessitating further post-extrusion processes such cutting away the recrystallized layer[35].

1.10 Finite element aspects of deformation process

Even for complex part geometries, FE models of the compaction and sinter processes, together with proper material laws for the powder, allow quantitative predictions of tool loadings, green density distributions, and sinter distortions. Although there have been several research on powder-forging with non-plastic deformation, particularly using numerical analysis methods [36], numerical analysis of sintered cold-forging with densification and plastic deformation has been limited. To anticipate the final shape, a suitable constitutive model

of powder compaction should incorporate numerous behaviors of the compaction process. Svoboda et al.[37] used a modified porous metal plasticity model that included creep behavior to evaluate the HIPing of APM2390 stainless steel powder. In comparison to experimental work, the results demonstrated very good agreement in terms of the ultimate deformed shape. The traditional metal-formed products development paradigm has shifted from heuristic know-how and trial and error to in-depth scientific calculation, analysis, and simulation to support metal-formed part design, forming process determination and configuration, product quality control and assurance, and the realization of FE-based simulation. The authors demonstrated the capability of modelling the plastic deformation behavior of CuZn37-A6061 composite porous billets during axisymmetric extrusion via conical dies using commercial rigid-plastic finite element (FE) DEFORMTM 2D software[38]. Designers can use the information obtained by FEM simulations about the work piece and tool to optimize the die and process design, saving time and money in the process. The simulation of the extrusion process can also be done with FEM. However, due to the problems involved, such as high temperature gradients, huge deformations, significant strain rate gradients, and transient behavior, the use of FEM simulation in the extrusion industries is limited.

1.11 Deep learning techniques for phase identification

Metallography is a science that studies the structure of alloy materials and reveals critical microstructure information. These microstructures are frequently observed and measured manually by researchers. Convolutional neural network (CNN) models have the potential to improve accuracy. Computer vision is being used in the materials domain, according to recent reports [39]–[41]. The use of machine learning to recognize microstructures has been documented in the literature. The distribution, shape, and size of the microstructures have a significant impact on the characteristics of aluminium alloy. As a result, proper segmentation of these microstructures is essential. Complex microstructure segmentation, on the other hand, is challenging and usually requires material scientists to manually divide microstructures into discrete pieces. This procedure is frequently slow, labor-intensive, and inconsistent. The metal micrograph is a digital image captured through a microscope that contains rich microstructure details and serves as a vital tool for metal microstructure investigation. Microstructure is usually done by hand by specialists, but due to the subjectivity of humans, there will be uncertainties. Various intelligent picture analysis approaches have arisen in recent years as a result of advancements in computer technology, enabling new methods for microstructure analysis. As a result, various attempts have been made to classify

and characterize microstructures using machine learning techniques and related technology, with the goal of enhancing microstructure analysis accuracy and efficiency compared to previous methods. Due to their excellent ability to learn discriminable features [42], deep learning has dramatically enhanced machine learning and achieved amazing results in picture segmentation [43]–[46]. In recent years, many advanced deep-learning metallographic segmentation algorithms have been introduced [47], [48].

1.12 Applications of Al and P/M Al alloys

Aluminium alloys offers a high strength-to-weight ratio, good castability, outstanding corrosion resistance, cosmetic surface quality, resistance to hot ripping, comparatively good thermal conductivity, relatively lower melting temperatures, good machinability, and good weldability, to name a few. Aluminium alloys are commonly employed in

Automobile: Cast engine blocks, wheels, piston rods, and radiators, stamped unibodies, space frame structures, body panels, and bumper systems

Aerospace components: airframe primary-load-carrying structural components, lightweight structures.

Electrical and electronic applications: Heat sinks, substrate/housing for microelectronics package, and spacers on structural electric transmission towers connectors, bus bars.

Defense: Rifle receiver forging, mortar and artillery projectile fuses, cartridge cases, artillery shells, and rocket warheads

Business machines: Drive-belt pulleys, hubs, end caps, connecting collars, and gears

Other Appliances: Sewing machine parts and thermostat control gears, Decorative pen and cover

Sports: A golf driver sole plate, Golf putter

Aluminum P/M alloys have piqued researchers' interest because they have excellent wear resistance, strength, temperature resistance, and a low coefficient of thermal expansion. Al-Si products are extensively used in the automotive sector for powertrain components. A V8 engine block cast in Al, for example, weighs about 32 kg against 68 kg in grey cast iron [49]. Fig. 1.2 shows the real life applications of Aluminium P/M alloys.

Automobile applications: camshaft-bearing, caps, pulleys, oil pump rotors, cylinder liners and shock absorber parts, cam caps, sprocket and rotor

Aerospace components: vane-type and gear-type pumps, the converter turbine hub, clutch plates, the clutch hub, converter clutches, outer and inner races

Defense applications: rocket motor cases in missiles, landing-gear assemblies (link, door actuators) ventral fin for F-16 jet fighter, helicopter rotors

Other: gear rack used on a disc drive, vacuum capacitor, link flexure used on a print tip for a typewriter, header/cavity block used on a high-voltage,

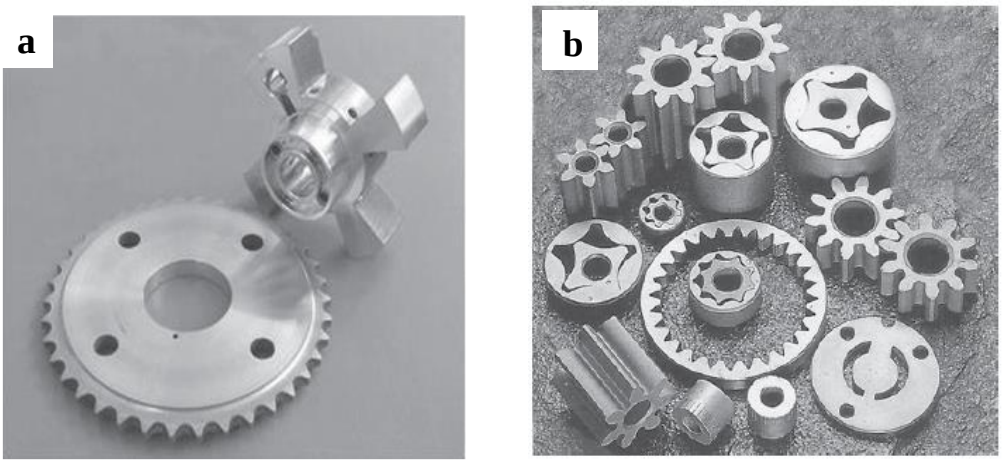

Fig. 1.2: a) Aluminium sprocket and rotors [49] (credit EPMA). b) Oil pump rotors and gears.

1.13 Organization of thesis

The thesis is divided into seven sections. **Chapter 1** deals with a brief introduction to the impacts of elemental additions to Al, as well as the deformation and densification behavior of P/M Al preforms, are presented. It also covers the constitutive modelling and finite element modelling (FEM) features of hot deformed materials.

Chapter 2 gives a thorough review of the literature pertinent to current research. The main goal of the critical review of literature was to thoroughly examine any previous research work that was related to the current work and to identify any gaps in current knowledge of sintering behavior, deformation, densification, microstructural and mechanical property evolution of P/M Al preforms. It also presents a survey of literatures associated to different research works based on structural properties like density, hardness, tensile strength, dynamic recrystallization behavior, FE analysis and the grain size analysis during the extrusion process.

Chapter 3 describes the structural properties evaluation on Al-Si and Al-Si-Mg hot powder compacts before and after extrusion and further characterization studies like XRD and DTA analysis. Further for different regions within the extrudates characterization was done.

Chapter 4 describes the dynamic recrystallization studies on Al-4Si-0.6Mg alloys at semisolid temperature ranges both numerically as well as experimentally. Similarly grain growth modeling was also studied.

Chapter 5 explains the effect of various Mg/Si ratios on the microstructure and structural properties of thixoextruded Al-Si-Mg alloys.

Chapter 6 deals with the prediction of alpha phase present in the OM images using deep learning algorithms and numerical simulation of hot compaction and hot extrusion.

Chapter 7 presents the results gained from the current study work, as well as the scope of future research activity.

CHAPTER 2

Literature Review

On the subject of sintering behavior, semi-solid forming, and hot deformation on Aluminum P/M alloys, several researchers have done outstanding work. The majority of the research has been divided into three categories: developmental research, microstructural and mechanical property evolution research, and simulation and modelling research. The work of different researchers on various areas of semi-solid forming and hot forming technologies is summarized in this chapter.

2.1 Introduction to P/M process

P/M parts can be divided into 3 categories: one in which the P/M approach allows for the production of a lower-cost component, a cost-efficient/high-performance intermediate category, and others in which the P/M approach results in a part with improved mechanical properties [50]. The first procedure usually produces products with inferior mechanical qualities than wrought material, while the third approach is usually more expensive. The first is a more typical commercial method, while the second is a more recent commercial approach, and high-performance parts are improved features of P/M technology. The two primary kinds of P/M manufacturing methods are traditional press-and-sinter methods and full-density procedures. Powder Metallurgy parts are made using a variety of techniques, ranging from high-pressure die compaction to pressureless molding techniques like slipcasting. The most common method is mold compaction at high pressures, compacting and forming at the same time. P/M products, on the other hand, can be shaped utilizing a variety of low-pressure processes that use binders to keep the shape of the parts while they are sintering. Another option is full density processing, which involves applying high pressure and temperatures to produce P/M parts with higher mechanical properties [20].

Metal powder is loaded into the die cavity of predefined shape during the die compaction process. The movement of rams along the axial direction applies pressure in the range of 350 to 700 MPa (50 to 100,000 psi). The metal powder particles gets compressed and cold welded to form a final shape with desired porosity as a result of the pressure. This compacted shape, known as a green component, is next heated to a high temperature (about

595 to 625 °C) for 10 to 30 minutes to sinter the metal powder particles into a solid mass. In uniaxial metal powder compaction, only vertically moving punches are used to provide pressure to the powder. The shape of the parts that can be conveniently manufactured is limited when metal powder parts are compacted in inflexible dies where the punches move along the axial direction. Compacting does not produce asymmetric parts or holes that are at an angle perpendicular to the compaction direction.

In order to attain the physical and mechanical property requirements of aluminum-matrix composites (AMMC's), a suitable matrix material composition must be chosen. Due to unfavorable interfacial reactivity [51] during P/M consolidation, addition of minor alloying elements in wrought alloys are often deleterious to the material characteristics of the composites. Pre-alloyed powder or blending elements with reinforcement, followed by any consolidation technique, such as hot pressing/rolling into a billet is the primary shaping process for producing discontinuously reinforced composites. These billets are then subjected to secondary process like extrusion or rolling for further consolidation. However, during consolidation of billet, the matrix may undergo incipient melting, resulting in significant insoluble and excess soluble intermetallic that form when the aluminium alloy matrix is solidified. The fracture toughness and ductility of the alloy are both harmed by these particles. As a result, leaner variations of the 2xxx and 6xxx series aluminium alloys (e.g., 2019 and 6080) have recently been developed, which contain strengthening components in concentrations no larger than their mutual solubilities, resulting in composites with useful ductility and fracture toughness [52]–[54]. Other sophisticated compaction techniques have been employed to achieve productive powder consolidated products, including frictionless isostatic pressing[55], high speed compaction [56], equal channel angular pressing [57], and rotary die pressing[58] .

2.2 Hot compaction

Cold pressing in rigid dies provides the advantages of dimensional control due to the well-defined cavity. Size constraints owing to press capacity, height-to-diameter limitations due to die wall friction, cracks during ejection, issues with compacts pressed from powders with low green strength, shape limitations like re-entrant angles and holes are all examples of process limitations.

In powder metallurgy, the hot pressing process used on metallic powders is critical. This is a complicated procedure that involves both material thermo mechanical characteristics and microstructural impacts. The technique entails heating the powder bulk to a temperature

below its melting point while applying pressure at the same time. The major consideration is that the material softens at high temperatures, making densification easier. Creep is a term used to describe a phenomenon that occurs in any sort of material.

The compacting of powder in heated dies can be used to produce huge billets. High temperatures and lengthy dwell durations enable densities of >95 percent of full density to be reached at compaction pressures one-third to one-half of those required for cold pressing to lower density levels. In most cases, full density is not obtained, and the billet has 3 to 5% porosity. As the characteristics of hot-pressed billets are lower from those of fully dense material, this porosity limits their application. As a result, hot pressed billets are frequently utilized as stock in upset forging, closed die forging, and other deformation procedures that remove residual porosity.

It is currently possible to use this sort of processing to produce components with mechanical qualities that are comparable to those of commercially available wrought products; however, super solidus liquid phase must be introduced during the sintering cycle to achieve this[59] . The presence of a wetting liquid boosts material transport and improves pore filling while also assisting in the breakdown of the surface oxide that coats each particle. Furthermore, initial particle size, cleanliness, alloying additives, sintering environment, and heating/cooling rates have all been found to affect the mechanical properties of the final sintered material [60], [61]. Higher green densities, stronger green strength, improved mechanical and soft magnetic characteristics, and more density uniformity across the as-sintered part are all advantages of the warm-compaction process[62]–[64].

In order to establish a cost-effective alternative approach for producing high-strength parts with complex forms, the powder forging process of rapidly solidified Al alloys was researched. Powder forged pieces have been found to have mechanical qualities that are comparable to those generated by extrusion[65]. In addition, compared to powder extrusion, powder forging generates a part in its final form immediately from beginning powders, without the need for machining (near net shaping). To ensure that the structural features achieved by rapid solidification are not lost, powder consolidation is often done by solid-phase diffusion at temperatures much below the melt points of the raw material powders.

2.3 Literature Survey on Semisolid Processing

Semi-Solid Metal (SSM) processing is gaining traction as a viable substitute to the traditional casting and forging manufacturing techniques. This category incorporates both

liquid and solid forming techniques. The semi-solid slug behaves like a solid in the absence of shear forces, such as self-standing, but when shear force is applied, the material flows like a liquid, resulting in thixotropic behavior. Because of these distinct characteristics, SSM routes have become popular alternatives to traditional casting on an industrial scale**.** SSM processing technologies are mainly divided into two categories[4].

The rheo-route entails preparing an SSM slurry of alloys from the liquid phase and transferring it directly into a die or mold for component shaping. Industry has invented the term "Slurry-on-Demand," or SoD, to characterize slurry producing processes that take place in the cast shops, ensuring a consistent supply of slurry for shaping operations.

The thixo-route is a three-step process that begins with the creation of a feedstock material of adequate length and weight that is equiaxed or globular, or has the potential to become spherical after further processing. To create a semi-solid structure, the feedstock material is reheated to temperatures between solidus and liquidus (mushy zone). The last stage is to shape the mush with thixotropic properties.

The eutectic volume fraction present in A357 alloys is around 45 percent. This, together with the liquid fraction distribution as a function of temperature, makes processing these alloys to a temperature close to the eutectic temperature for a particular liquid fraction. They also have good casting properties in terms of flow length, flow front joining, and the formation of hot cracks during solidification. These benefits greatly expand the operating window for the process, enabling for the production of defect-free components. In addition, these alloys are highly corrosion resistive and offers a broad range of mechanical characteristics, such as ductility and high strength, which may be changed through heat treatment processes and the Mg content (0.25–0.45 percent in A356 and 0.45 to 0.60 percent in A357). As a result, semi-solid casting dominates industrial manufacturing of these alloys [14].

A challenge in adopting the SSM process is that simply substituting the manufacturing process for a particular geometry is rarely sufficient. In majority of the cases, significant advantages will necessitate a process-specific redesign. This is especially true if the aim is to obtain considerable weight reductions by replacing steel forging with aluminium SSF. The new design leverages the process capabilities of semi-solid castings to minimize weight by forming hollow cross-sections with high rigidity, impossible to achieve through forging. Despite the fact that the AlSi7Mg alloys vast spectrum of mechanical qualities covers a wide variety of technical domains, some applications require specialized properties that are better achieved by

other alloy systems. As a result, several alloys have been developed and demonstration experiments have been conducted to fully leverage the potential of semi-solid forming. These studies reveal that the fine-grained spherical microstructure needed for SSM process may be achieved in principle in most studied aluminium alloys [66]. However, the problems in attaining sound portions during heating and forming vary greatly depending on factors such as reheating behavior, flow behavior, and hot crack sensitivity.

High wear resistance can be accomplished utilizing metal matrix composites (MMCs) or SSF of hypereutectic Al-Si alloys like AlSi17Cu4Mg (A390). Both alloys are not easy to cast using traditional methods and can result in excessive tool wear during machining. A390 has proven to allow good die filling while generating a microstructure with evenly dispersed primary silicon particles in semisolid forming. MHD (Magneto Hydrodynamic) casting can create feedstock billets from SiC particle-reinforced MMCs like Duralcan[67] if particle sedimentation is avoided in the furnace by proper stirring. Because of the stabilizing impact of the non-meltable particles, reheating and semi-solid casting behavior of these samples is comparatively simple. Particle agglomeration or segregation during the solidification does not take place, which is a key advantage of SSF over casting these materials.

The microstructural and mechanical characterization of 6061 Al-based composites supplemented with SiC particles was investigated by Zhang et al.[68]. The microstructure of powder thixoformed 6061 composite was found to be near-spheroidal primary grains and intergranular secondary solidified structures, whereas permanent mold cast 6061 composite had a coarse and equiaxed dendritic morphology. As a result, the UTS and yield strength of the permanent mould cast alloys were higher. The pore-free structure, matrix reinforcement, and increased bonding between matrix and reinforcement are primarily responsible for the reported improvements in microstructure and mechanical performance. The processing procedure has a significant impact on the microstructure and mechanical properties of thixoformed materials.

These forged alloys are noted for their outstanding mechanical qualities at both room and high temperatures. Various attempts have been made to employ these alloys in semi-solid casting[66] but they have a very narrow processing window, a short flow length, and a tendency to create hot fractures. AlMg5Si2Mn alloys composition has been modified to have had some success[69], [70] , for example, the space frame node for an Audi car construction, which requires a yield strength between 120 and 150 MPa, an ultimate strength above 180 MPa, and elongation above 15%. AlSi7Mg was not a viable option because this thin-walled

construction needed to obtain these qualities without heat treatment to avoid deformation. It was successfully semi-solid cast from AlMg5Si2Mn MHD cast billets [69].

P/M and thixoforming technologies work together to create finer, more uniform structures with superior mechanical qualities than casted feedstock semi-solid forming. Unfortunately, very few studies on powder thixoforming technology have been conducted. Wu et al. [71] investigated semi-solid powder processing as well. They looked at the impact of SiC volume fraction, SiC particle size, forming pressure, and matrix particle size on the microstructure and mechanical characteristics of an Al6061-SiC composite. They came to the conclusion that decreasing SiC particle size increased semi-solid compaction pressure, and lowers the SiC loading limit (volume) for a given pressure. When SiC particles were smaller than Al6061 particles, non-uniformity in microstructure was detected. As a result, fracture surfaces and hardness varied greatly. Furthermore, dense components were made using smaller SiC particles, resulting in a microstructure that was uniform and free of microcracks, as well as a higher hardness.

2.4 Literature Survey on Semisolid extrusion

Secondary operations like casting, forging, and hot deformation can improve material density and mechanical qualities. Semi-solid extrusion (SSE), out of all the SSF techniques, has the most advantages and is of particular importance for high productivity. Due to flaws such as fractures and porosity, materials produced using the casting technique have low mechanical strength. Forging methods offers excellent mechanical strength, but they necessitate large forming loads to produce good products, and machining is necessary afterwards, reducing productivity and efficiency[72]. If a semi-solid extrusion method is adopted, the benefits of forging and casting can be combined to make superior Al alloy products. The advantages of semi-solid extrusion over traditional forming procedures like casting and forging are numerous. High pressure and slow extrusion speeds are common problems with traditional extruded materials. For technological and economic reasons, it is therefore more efficient to extrude materials in a semi-solid condition.

Intricate shapes of light metals are industrially manufactured by standard solid-state extrusion, as indicated in the introduction, therefore there is no economic necessity to design a more complicated SSE technique for Al alloys. SSE of lower melting alloys, on the other hand, is a highly interesting option to examine the parameters of the process without having to be content with the subsidiary issues caused by semi-solid steel's high temperature levels.

Considering a general process window diagram for traditional rod extrusion processes (Figure 2.1a), it's evident that using standard extrusion setups to raise the billet temperature to semi-solid condition will result in product faults [73]. If the load necessary to reach a high extrusion ratio is more than the load limit, the billet temperature can only be raised till the maximum extrusion ratio (A_0/A_1) is attained. Local melting caused due to dissipation, leads to additional increase in the billet temperature, which results in local flaws such as heat cracks (Fig. 2.1b).

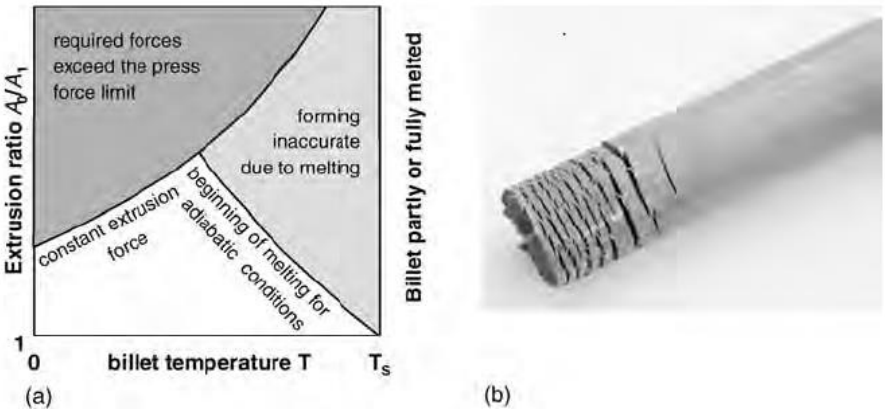

Fig. 2.1: Characteristic features of extrusion [73]

Kiuchi et al.[74] conducted the first semisolid extrusion studies in 1979. They investigated the effects of the desired extrusion load and temperature of the tool for Al and Pb alloys with a billet 40 mm in diameter and 25, 30, or 40 mm in height under various test settings using a horizontal forming equipment. Experiments were done for two conditions of simultaneous heating process (tool and workpiece heated) and no preheating process (tool not heated) The authors noted that the optimal liquid fraction of 5–10 percent were needed for semi-solid extrusion of the examined alloys and the required press load increased with fall in liquid fraction, which was only 1/5th of the necessary press load in conventional extrusion. In terms of process differences, bars extruded with the no-preheating tool arrangement showed more work hardening and less ductility than bars extruded simultaneously.

In terms of tensile strength, both process types produced similar results, however the tensile strength declined as the liquid percentage increased [74]. For all process variations, the extruded bars exhibited better microstructure. Frictional effects between the billet and the die walls was insignificant when the liquid component was greater than 20%.

Later, the same group [75] looked at particle-reinforced aluminium alloy AA-5056 (20 vol. percent) in addition to ordinary aluminium alloys. Al_2O_3 with a liquid fraction of 20–30%

and an extrusion channel diameter ranging from 2 to 10 mm in 2 mm increments. To prevent the billet from cooling in the container, the tool was preheated to the temperature of the billet. The scientists also observed that when profile complexity increased, the extrudable wall thickness dropped. In general, they came to the conclusion that the alloys may be easily extruded with little strain. The yield stress of extruded goods can be improved with heat treatment. The extruded products for particle-reinforced materials had a smooth surface and no extrusion problems. In SSE of this material, the dominating factor is the liquid fraction responsible for the particles' embedding.

Ketabchi et al.[76] investigated the effect of cooling rate during semi-solid extrusion, as well as the evolution of microstructural and mechanical properties of 7075 Al-alloys as temperature and holding time changed. The optimum temperature and holding time for developing appropriate microstructure were discovered to be 580 °C and 10 minutes, respectively. It also demonstrated that when the cooling rate severity increased, the mechanical characteristics of the alloys improved due to a decrease in shrinkage porosity and final grain size. The authors concluded that the optimal semi-solid extrusion process parameters result in mechanical qualities that are comparable to or better than those of traditionally extruded goods.

Neag investigated [77] the influence of experimental circumstances on 7075 Al-alloy during thixoextrusion. Extrusion temperatures of 602°C, 609°C, and 617°C were employed, with solid fractions of 0.82, 0.77, and 0.69 respectively. As the slug temperature dropped and the solid fraction grew, the forming load increased. With increasing temperature, sliding between the solid and liquid phases, as well as grain rearrangement with each other, was seen without any plastic deformation. The importance of solid percentage in simulation results of semi-solid extruded aluminium was highlighted by Neag et al. [78]. During semi-solid extrusion, simulation and modelling findings revealed the evolution of the degree of agglomeration as a function of temperature and strain rate field. The research on semi-solid processing with a high solid fraction (0.5) and a high tool temperature. 600 °C was the ideal temperature for achieving laminar flow without liquid ejection.

The microstructure and mechanical properties of semi-solid extruded bars of ZL116 (ZAlSi8MgBe) cast Al-alloy were studied by Dazhi et al.[79]. The Beryllium presence in the alloy increased the mechanical characteristics and corrosion resistance by enhancing the precipitation hardening phases during age, according to the findings. The extruded samples were likewise smooth with fine and homogenous microstructure, according to the researchers.

2.5 Hot extrusion of Al alloys

Deformation processing (extrusion, forging, or rolling) of the consolidated composites, in addition to generating shaped structures, develops the greatest characteristics possible by breaking up any preexisting oxide on the alloyed powder. When whisker-reinforced composites are extruded, the whiskers are roughly aligned in the extrusion direction. Secondary processing, such as machining and joining, is required for the production of useable shapes, at least to some extent, which is not well established for composites. Because of the great hardness of the ceramic reinforcement, conventional machining of composites is extremely challenging[80].

Extrusion is a versatile method that turns cast billets into long uniform shapes with easily polished surfaces in a single ram stroke. This is especially true for aluminium alloys, where heat-resistant steel dies provide excellent durability, even in sections with several cavities and uneven projections. Over long lengths, extrusions are dimensionally precise, and any straightness lost after cooling can be recovered by cold stretching[81]–[84]. Aluminum extrusions account for more than half of all extrusion volume and nearly a quarter of all aluminium mill output.

2.5.1 Various Material Flow during Extrusion

Extrusion, unlike rolling and wire drawing, is not completely quasi-static due to the significant friction forces involved. In the extrusion of aluminium, friction is exceedingly high; in fact, it is frequently so high that plastic shearing occurs in the billet's subcutaneous areas rather than sliding at the interface. The deformation zone does not remain fixed under these conditions, but instead gradually spreads inwards from the container wall due to the progressive thickening of zones of severe shear. Under very good lubrication, on the other hand, the deformation zone is more confined, and the process becomes more quasi-static. On this basis, it appears to be a useful simplification to consider any individual occurrence of extrusion as working under conditions in the middle: i) entirely unlubricated, causing sticking friction; (ii) lubricated, resulting in frictionless slippage at the billet container contact.

The genuine situation, however, is far more complicated, and Pearson and Parkins [85] had to postulate three forms of metal flow: (i) unlubricated; (ii) lubricated; and (iii) a type characterized by the presence of an extrusion defect or back-end defect at a relatively late point

in the process. Under normal industrial conditions, hot extrusion of aluminium is unlubricated, and it may be considered to approach sticking conditions at the interface.

Pearson and Parkins classified flow during the process as follows (Fig. 2.2):

a - indirect;

b - lubricated;

c - unlubricated;

d - with extrusion defect.

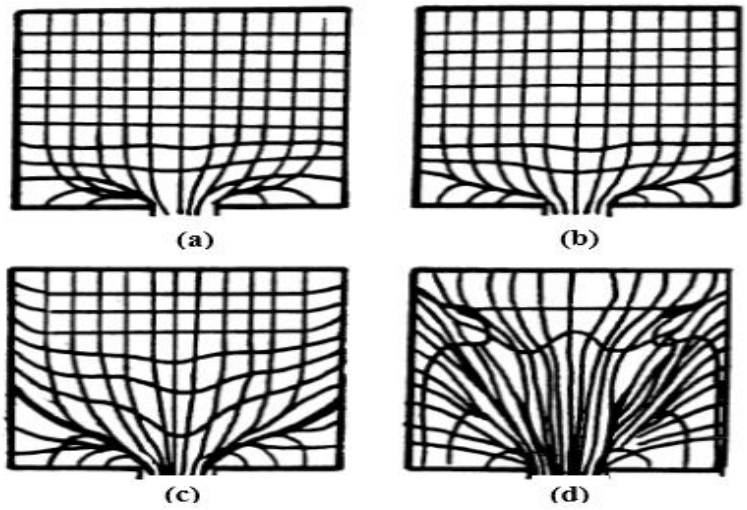

Fig. 2.2: Various metal flow in extrusion **a)** indirect **b)** lubricated **c)** unlubricated **d)** unlubricated with defect

Extrusion pressure has the first impact of compressing or 'upsetting' the billet into firm contact with the cylinder wall. There is no friction between the billet and the container in indirect extrusion, and the flow is streamlined, as shown in Fig. 2.2. (a).

When employing the indirect technique, the surface of the billet becomes the surface of the extrusion, which is why it is common practice to scalp all billets. Of course, this necessitates a separate and costly procedure. Although it is commonly considered that there is no dead metal zone in indirect extrusion, as we will demonstrate later, this is not the case. A conical dead metal zone forms in front of the die in lubricated direct extrusion (Fig. 2.2(b)), but there is little shearing at the container/metal interface; as a result, there is a tendency to extrude part or all of the surface into the surface of the extrude, which is why little or no lubrication is used in aluminium alloy extrusion. When the billet is unlubricated, there is a propensity for relative motion between the container and the skin of the billet as extrusion progresses and the billet

shortens (Fig. 2.2(c)). High friction forces are generated at the interface because to the close contact and lack of lubrication, and zones of significant shearing occur immediately beneath the skin of the billet. A dead metal zone forms at the front of the billet early in the process, and it's commonly thought to extend over the die face to the orifice, forming a 45° angle with the container.

When there is no lubrication, the well-known extrusion problem arises. This fault develops late in the process, when material from the billet's oxidized and contaminated surfaces flows round from the back of the billet to take the place of the billet's core that has passed through the die (Fig. 2.2 d). The impure material eventually travels through the die in the shape of an annulus, separating sound material in the outer half of the cross-section from equally sound material in the center due to the symmetry of the process. At times, the discontinuity is so complete that a portion of the core can be removed from the billet's back end. The problem has been determined due to the friction acting between the billet container interface.

2.5.2 Effects of Temperature

Hinesly and Conrad [86] studied the temperature effects on the metal flow pattern of the extruded AA2024. Their findings showed that a single flow along the principal axis of the extrudates was seen at low temperature extrusions, with a different flow pattern at higher values.

Previous researchers [87], [88] attributed this to lubrication variations, but Conrad [83] et al. proposed that it was due to differences in plastic characteristics and thus temperature disparities inside the deformation zone. Tutcher [23] demonstrated the extrusion effects of AA5456 with a standard flat-surfaced dies, whereas conical dies were used for their experimental information.

When extruding 6060, maximum profile surface temperatures should be expected at 590°C (the eutectic temperature) when the billet contains Mg_2Si particles (assuming the billet is heated straight to temperatures below 475°C, the solvus temperature) before incipient melting occurs. When all of the, the incipient melting will occur At 620°C which is the solidus temperature, random melting happens because of all magnesium and silicon diffusing into solid solution. This is true for billets that have been directly heated to temperatures exceeding 475°C or for billets that have been overheated to temperatures below 475°C.[89]. At hot working temperature of 550°C exposure of AI-Si, AI-Fe and AI-Fe-Si alloys was found to increase dynamic recovery and substructure development, [90].

Preheating of Al 2014 alloys for long periods of time at temperatures below 440°C has little effect on the extrusion-process flexibility or extrudate structure. If the billet is preheated to 500°C and rapidly cooled to the extrusion temperature, some additional solubility must occur, and some soluble elements should be retained in solution; this increase in solubility should be greater at the surface, resulting in increased resistance to deformation at the surface of a directly extruded billet[91]. As a result, the DC cast form would be poorer in terms of machinability and wear. As a result, the homogenization and extrusion processes must remove this inhomogeneity.

Elements can be added to the extruded form to generate solid solutions, precipitates, eutectic, or primary particles. The most typical additives to impart precipitation hardening are Mg and Cu, both of which greatly increase the hardness. These constituents will enter solid solution during the heating process to reach extrusion temperature, potentially increasing flow stress and slowing extrusion speed. Celliers et al. [90] demonstrated that alloys having high Si content have flow stresses comparable to some hard alloys (7XXX) at extrusion temperature of 450°C.

Hot working AI-Mg alloys with high Mg content (5083 and 5465) is difficult. Hence a 2 stage heat treatment process involving holding temperature of 375-425°C for approximately 2 hours succeeded by 500-530°C for roughly 8 hours has been performed. This has brought additional benefits like lowering deformation stress and increasing ductility [92]. The greater the sub grain size and the higher the recrystallization temperature, the higher the extrusion temperature. Recrystallization of the nonhomogenized material demands a much greater temperature than that of the homogenized material.

In the intermediate temperate range, notably at 480°C for Al-Zn-Mg alloys, billet homogenization creates very fine but numerous precipitates: (MnFeSi), Cr, and Zr, respectively. Because the precipitate structure is not fundamentally altered in the short-term warming up to 450°C, or 550°C, these exert a restraining influence on recrystallization at both the lower and higher extrusion temperatures [93], [94]. In terms of manufacturing Al-alloy products, tooling, and press design, hot extrusion is the most sophisticated technique. The 6xxx and 2xxx series alloys are often used materials for hot extrusion because they have the best economic and technical qualities, such as ease of extrudability into any shape, heat treatment resistance, and higher mechanical properties. Hot extrusion is the most cost-effective way to

make high-density P/M components. The management of deformation geometry, as well as the use of optimal temperature and speed parameters, can increase an alloy's extrudability [95].

2.5.3 Effects of Extrusion die geometry

The right mix of extrusion ratio and die included angle is critical for successful hot extrusion of P/M alloys. Failure experiments in extrusion of P/M Iron preforms were investigated by Venugopal et al.[96]. They came to the conclusion that friction between the preform, die, and container raised tensions in the extrusion process and caused differential velocities, which can lead to sample failure. The die approach angle of 40° produced a smooth surface with no cracking, but increasing the die angle to 60° and 90° increased the cracking tendency. Extrusion cracks in P/M preforms can be prevented by reducing friction between tools and preforms, preventing tensile stresses, and ensuring only compression stresses are generated.

Onuh et al. [97] investigated the effect of die angle, area reduction, and extrusion speed on the quality of cold extruded aluminium and lead alloys in an experimental study. The average hardness of extrudates increased as extrusion speed and area were reduced, according to the findings. The influence of die land on flow pattern, extrusion pressure, and hardness variation over the length of the extrudate of lead alloys was studied by Ajiboye and Adeyeni [98]. For any extrusion ratio, the extrusion pressure rose as the die land length grew. Tiernan and Draganescu [99] examined how surface roughness and hardness of cold extruded Al-alloys were affected by changes in area, die angle, and lubrication. The die angle, rather than the reduction ratio or lubrication, influenced the surface roughness of the extrudates, according to statistical modelling studies. Shahzad and Wagner [100] investigated the microstructural evolution of AZ80 Mg-alloy crystallographic texture and mechanical characteristics during extrusion at various extrusion ratios. The finer grain size was shown to produce greater yield and ultimate tensile strengths. Das et al. [101] investigated the effects of die land length, extrusion ratio, and lubrication on the surface roughness and hardness of Al-alloys during extrusion. The average hardness of extruded items produced by 15 mm die land length was 5% higher than dies with 10 mm die land length, according to the findings. At low extrusion ratios, plastic strain and strain hardening were minimal. Huang et al.[102] investigated the microstructure and characteristics of Ti-composite as a function of extrusion die angle. They showed that raising the die angle from 45° to 75° lowered both tensile strength and elongation.

2.5.4 Effects of strain rate during extrusion

Extruded Al-alloy products might be made with large stresses and high friction. These characteristics cause heat to be generated within the extruded components, resulting in

nonuniformity and a decrease in mechanical qualities. Controlling the strain rate or ram speed during extrusion helps reduce the unstable condition of extrusion and nonuniformity in mechanical characteristics. With a lower strain rate, the deformation time increases. Extending the duration to attain the steady state temperature promotes dislocation annihilation, resulting in microstructure irregularity in extruded goods. As a result, the strain rate or ram speed should be tuned to achieve microstructure and mechanical property homogeneity among all extruded products. Peres et al. [103] investigated the hot extrusion of gas-atomized nanostructured Al alloy powders. The results showed that as the strain rate increased, so did the compressive strength and elongation of the extruded samples. They also showed that due to high friction and temperature differences inside the sample, the high strain rate during extrusion may induce cracks on the surface of the samples. The influence of stem speed on metal flow behavior, surface quality, and temperature distribution during extrusion was studied by Zhang et al. [104]. At an ideal ram speed of roughly 0.3 mm/s, they found homogeneity in metal flow and temperature distribution. At higher strain rates, non-uniformity in metal flow during extrusion develops, resulting in cracks, surface burning, and twist deformation in extrudates[105]. With increased strain rate or ram speed, the required extrusion force increases. Extrudates' welding quality and mechanical qualities improve as the strain rate rises.

2.5.5 Strengthening mechanisms during extrusion

a) Grain Size Strengthening

The dislocations interact with the Grain Boundaries (GBs) at low temperatures (under 300°C for Al), generating pileups that induce back stress on the source, resulting in the Hall–Petch relationship (equation 2.1).

$$\sigma y=\sigma_0+k\sqrt{d} \text{---------- (2.1)}$$

where σ_0 denotes a single crystal's yield strength, D the average grain size, and k the strength factor[105]–[108] . Pileups cause stress raisers in a neighboring grain to initiate slide; however, in Al near 20°C, they swiftly undergo DRV into a cellular substructure that is smaller in size and has a bigger disorientation than the cells in the grain center up to 0.3. Because strain hardening is larger for smaller grain sizes, the Hall–Petch effect is preserved, with a decreasing value of k as it approaches 0.5[109] . Heavy working and recrystallization annealing are commonly used to produce fine equiaxed grains. Finer grains result in a more consistent strain. The effective grain size is the short dimension for grains that have been stretched by strong

straining and softened by annealing. The importance of texture is unaffected by grain size. At high T and 10^3–10^1 s^{-1}, very fine (8 m) grains can cause GB sliding with a high strain-rate sensitivity, conferring high resistance to necking; this results in super plasticity with high tensile elongations. The change of austenite to ferrite/pearlite, achieved by low finish rolling, can improve structure refinement in steels.

b) Strain Hardening

The creation of substructure causes strain hardening, which rises with decreasing cell sizes and dislocation spacing in both the walls and the interiors. At higher T, DRV (dislocation annihilation and rearrangement) reduces their decline with strain, and their dimensions stabilize in steady-state deformation in hot working and creep. Other strengthening mechanisms, such as orientation effects that cause deformation bands (at all T) and block wall creation, influence strain hardening (in cold working).

c) Solute Strengthening

Substitutional solute atoms of a different size than the Al hosts may interact with the dislocations in an elastic manner, generating Cottrell atmospheres around the dislocations. The strength of such locking varies depending on the element, with Mg being the strongest and Cu, Zn, and Si being the weakest. The action varies with temperature, resulting in poorly formed cell structure, shear banding at 20°C in Al–5Mg, and sluggish development of much smaller sub grains at higher T compared to Al; preceding chapters are devoted to hot working of alloys with Mg) and alloys that also precipitate As the SFE diminishes, solutes can also segregate to stacking faults between partial dislocations, increasing the separation. The Suzuki effect, which is marked by broad, stacking faults in TEM coupled with straight slip lines observed optically, does not appear to be a major factor in Al alloys, but it has a strong effect in Cu by the addition of Al or Ge; this is called the Suzuki effect and is marked by broad, stacking faults in TEM coupled with straight slip lines observed optically. The ascent or cross-slip of the dislocations is slowed by increased dissociation, which slows healing Solutes also segregate to the GBs, resulting in a reduction in GB mobility and a delay in recrystallization.

d) Dispersion Strengthening

The existence of tiny particulates having a low solvability in solid Al, is referred to as dispersion. In the 3000 and 5000 series alloys, Al_6Mn and Al_3Fe particles are widely used to

adjust grain size. They usually form at a temperature just below melting and can be coalesced by heating near that temperature. Producing very tiny eutectic rods (0.2 μm) such as Al_3Fe by severe heat break up and distribute the rods as equiaxed particles can create effects similar to this. As the dispersed particles have a low solubility up to 400°C, they can improve creep resistance and do so for longer periods of time due to lower diffusion rates of the fundamental constituents. Large component particles (>2 μm) of impurities Fe and Si with Al and other alloying elements may develop with random distributions during solidification in DC casting. These are harmful stress raisers that diminish toughness rather than providing good strengthening.

They can be decreased by better controlled composition and are largely eradicated by atomized powder compaction. Rapid Solidification Processing (RSP) can convert transition metal hypereutectic liquid solutions into very thin particles or ribbons with high densities of dispersed particles, with cooling rates up to 106 K/s preventing segregation. Controlled heating during powder consolidation results in the creation of dispersed particles of appropriate size and dispersion. In a different method, inert particles with the specified composition, size, and volume fraction are mixed with powder particles of any common alloy. After mixing, these are frequently ball milled for even distribution and hammered for intimate contact.

e) Precipitation Strengthening

This is most likely the most well-known and distinctive procedure of hardening various series of Al alloys, such as the 2XXX, 6XXX, 7XXX, and 8XXX [106] . Solution treatment is used to dissolve the individual constituents that will go into the precipitates, followed by subsequent quenching to keep them in solution and a large concentration of vacancies. The components may be final shaped or straightened with the strain adjusted to help the final step, with the strength only slightly enhanced. Aging, which is most usually done artificially at temperatures between 130°C & 190°C, results in a succession of coherent zones of increasing size (0.01 m), hardness, and spacing, as well as a fall in hardness.

Finally, as dislocation loops form around the particles in the Orowan process, the precipitates become noncoherent, resulting in decreased yield strength but significant strain hardening. In the 6000 and 2000 series alloys, the existence of a dislocation substructure improves precipitate distribution, but not in the 7000 series. Extrusion processing can be used to achieve solution with rapid cooling at the die exit for the 6000 series; the substructure and texture are kept to add to the strengthening created by T5 age hardening.

2.6 Constitutive modeling on hot deformation of Al alloys

Determining the constitutive relationship for the material is one of the most difficult aspects of thermo mechanical modelling of the extrusion process. Most techniques of modelling and simulation for hot working research and control of metals require constitutive equations[6], [110]. Constitutive equations, which correlate flow stress, strain rate, and temperature, can be used to simulate the mechanical behavior of pure metals and alloys under heat. Uniaxial compression testing at a variety of temperatures and strain rates is commonly used to determine the values of the variables in these equations. Various constitutive models have been developed in earlier papers to predict the constitutive behavior of a wide range of metals[111]–[115]. The exponential model introduced by Sellars and McTegart[116], which Rokni and Zarei-Hanzaki[114] adapted for several temperature ranges, is one of the most well-known and extensively used models of constitutive equations under hot working conditions [114], [115]. The flow stress of the material is described by this model as a hyperbolic sine-type Arrhenius-type equation. It can be used to treat a variety of stress.

In the hot deformation process, optimal processing parameters can increase material properties [117]. Many factors influence the flow of material during the deformation process, like deformation temperature, strain, strain rate, friction, and so on, all of which affect the characteristics of the deformed specimens [118]. As a result, the processing conditions used during hot deformation must be tuned in order to obtain not only the final shape, along with the needed characteristics and microstructure in the deformed material [119]. Metallurgical phenomena such as Work Hardening, Dynamic Recovery, can impact the flow behavior, microstructure, and energy required for deformation during hot deformation [120], [121]. As a result, various researchers [122], [123][124] studied Al-alloys to better understand hot deformation behavior during compression at high temperatures. The microstructure evolution of 7050 Al-alloy under deformation at increased temperature was studied by Li et al.[125] , who discovered that the presence of DRV and DRX contributed to metal flow softening.

The flow stress of 4032 alloy decreased with increasing temperature and decreasing strain rate, according to the real stress–strain curves. Scanning electron microscopy and transmission electron microscopy were used to view and analyze the alloy's microstructural evolution during hot deformation. The findings of the experiments revealed that Si particles did not engage in deformation and that dynamic recovery was the predominant softening

process. In addition, the hyperbolic sine function can be used to describe the hot deformation behavior of the 4032 alloy[126].

On the Gleeble-1500 thermal simulation machine, hot compression tests of homogenized 7050 aluminium alloy were performed, and the microstructure was investigated using electron back scattered diffraction and transmission electron microscopy. The Zener–Hollomon equation with activation energy of 160.3 kJ/mol was shown to lower peak stress levels as deformation temperatures or strain rates increased. The results showed a steady decrease in very low angle boundaries, exhibiting a disorientation between 2 and 5, associated with substructure, as Z values decreased, and a steady increase in other higher angle boundaries, especially with disorientation angles between 30 and 60, associated with substructure[127]

Because of its high mechanical qualities, stress corrosion resistance, and welding properties, a 2519 aluminium alloy is widely employed as a structural material in many industries (such as aviation and rocket launching systems)[128], [129] . The alloy's micro-alloying, strengthening methods, and thermo mechanical treatment have all been extensively researched. A systematic investigation of the effects of yttrium (Y) inclusion on the precipitation hardening and mechanical properties of 2519 aluminium alloy at extreme temperatures was recently published[130]. The inclusion of Y boosts tensile strength at both room and higher temperatures, according to the study. The high density of fine θ precipitates and the AlCuY intermetallic complex with good thermal stability are responsible for the increased strength of 2519 aluminium alloy.

Complex plastic deformation prior to age, incorporating both cold rolling and stretching, rather than stretching alone, is beneficial for stress corrosion cracking resistance, according to Dymek and Dolla [129]. At higher temperatures, the flow curves tend to exhibit steady state flow, and it's essentially a dynamic competition procedure between working hardening caused by dislocation reduplication, pile up, and tangle, and softening caused by dislocation rearrangement and the counteraction of unlike dislocation. This type of flow pattern is typical of hot working with DRX [131]. Flow stress levels are shown to be dependent on deformation temperature and strain rate, with flow stress increasing as deformation temperature decreases and strain rate increases. Compression tests on the solution-treated ZL109 alloy were carried out at temperatures ranging from 250 to 450 degrees Celsius and strain rates ranging from $0.0005s^{-1}$ to $0.5s^{-1}$. On the basis of flow stress data obtained as a function of temperature

and strain rate, a processing map was developed, revealing two domains of hot working for the alloy: one is located between 270°C and 340°C with strain rate between $0.05s^{-1}$ and $0.5s^{-1}$, and the other is located between 380°C and 450°C with strain rate between $0.0005s^{-1}$ and $0.004s^{-1}$.[132]

Hot deformation compression tests were used to assess the hot flow stress behavior of three Al-Mg-Si alloys at temperatures ranging from 400 to 550 °C and strain rates ranging from 0.01 to 10 s^{1}. Constitutive parameters for predicting the hot flow stress behavior of these distinct alloys were established using the hyperbolic sine constitutive model. The impact of chromium (Cr) addition and increased Mg-Si concentration on average steady-state flow stress, constitutive, and strain rate sensitivity (m) parameters was investigated. The alloy having 0.2 wt percent Cr had a higher average steady flow stress when deformed at low strain rates ($0.01s^{1}$) than the alloy with equal Mg-Si concentration but no Cr addition. A decrease in the strain rate sensitivity parameter (m) and an increase in the activation energy for hot deformation were noticed with the addition of 0.2 wt percent Cr and an increase in Mg-Si content. By comparing the predicted and experimental flow stress behavior of alloy under deformation settings other than the temperature and strain rate conditions used to build the model parameters, the predictive accuracy of the developed models was demonstrated. The results show that the created model can accurately forecast alloy behavior at strain rates and temperatures that are outside of the model's development range, such as when the activation energy for hot deformation increases[133].

2.7 Modeling microstructure evolution during hot deformation of aluminum alloys

The microstructure development of the material during forming processes must be studied in order to obtain the material behavior of the final product. The constitutive model relationship is frequently used to explain any alloy's plastic flow features. As a result, in commercial hot working applications, certain constitutive models of materials have been utilized to describe the sensitivity of the flow stress and microstructure to the forming temperature, strain, strain rate, and Initial Preform Relative Density (IPRD). Mechanical qualities such as strength and hardness have an impact on the end product's productivity and longevity. The grain size of the distorted materials can influence these mechanical properties. As a result, understanding the relationship between process parameters and grain size effect during hot deformation is critical for metal forming process designers. In general, phenomenological models and physically based models are used to simulate microstructure

evolution during forming processes [134]. The final state of the recrystallized structure is described in phenomenological models in a post-processing procedure without taking into account any microstructure evolution laws.

To determine the recrystallized grain size, the empirical Johnson–Mehl–Avrami–Kolmogorov (JMAK) relation is often utilized[135], [136]. For most solid state transformations, the JMAK relation for nucleation and growth transformations works quite well. The use of quantitative models capable of reliably predicting the effect of process parameters on the result can be used to control the microstructure, texture, and characteristics of a material during a thermo-mechanical process [137]. Many different ways to modelling microstructure evolution during and after heat deformation have been presented. Empirical, state variable, statistical approaches, Monte Carlo methods, and cellular automata methods are examples of these.

Microstructure modelling during hot deformation can be done on two levels: at the macro level, where microstructure models are utilized for post-processing of thermo-mechanical history, and at the micro level, where microscopic models are used to model microstructure during hot deformation [138]. The bulk of microstructure models for hot deformation of aluminium alloys involve only dynamic recovery and static recrystallization following deformation. Although, attempts to simulate recrystallization, following extrusion of 2XXX, 6XXX, and 7XXX aluminium alloys have been made [139]–[144] no microstructure models for extrusion of Al-Si-Mg alloys have been attempted yet.

If the existence or lack of deformation (i.e. strain rates) is related to the beginning of dynamic or static recrystallization mechanisms, the dynamic recrystallization mechanism is tightly related to the kind of material: Low stacking fault energy materials promote traditional dynamic recrystallization, DRX (nucleation and growth of new undeformed grains during deformation, as seen in pure aluminium), whereas high stacking fault energy materials (such as aluminium alloys in the 6XXX series) exhibit different behaviors.

The microstructure of aluminium billets extruded at high temperatures is influenced by the alloy, as well as the forming and temperature history. It is becoming increasingly important to forecast grain size and precipitation for an optimal process design by adjusting parameters like ram speed, extrusion temperatures. This research examines the microstructure during the extrusion process of AA6060, AA6082, and AA7075 alloys to provide references for microstructure prediction based on material flow, as well as strain and strain rate history. Billets

were partially extruded into circular profiles. Furthermore, based on macro etchings and visible microstructure, these billets have been examined to indicate flow of material, DRX and SRX, and metallographic features under various conditions, such as near the dead zones in the extrusion die at various strain rates.[145]

Experimental observations and numerical analysis are used to explore the grain size and shape evolution of 6XXX aluminium alloys during hot metal forming procedures. To mimic grain evolution during deformation and subsequent static recrystallization, a unified model is built. To begin, an experimental set was built to replicate a small-scale direct extrusion in order to find grain deformation modes and empirical equations that characterize the evolution. The equations were then linked to modified formulations of static recrystallization found in the literature, and user-routines were used to implement them in the Lagrangian FE program Deform. The created model calculates all phases of the phenomenon in an original way, taking into account not only the static recrystallization but also the prior deformation phase. The effects of geometric dynamic recrystallization, the influence of sub grain size, the distribution of dislocation densities, and the stored energy on succeeding grain static recrystallization were studied[146].

This article looked at the flow lines, microstructure, and mechanical properties of a flow control formed (FCF) 4032 aluminium alloy scroll plate. Back pressure's effect on the formation process was studied, and a scroll plate with optimum shape and size precision was created. The results demonstrate that increasing back pressure improves scroll wrap creation while increasing effective stress and extrusion load rapidly. The use of specific levels of back pressure is limited. The flow lines are commonly distributed along the scroll plate's form. Formed scroll plates were studied for their microstructures and mechanical qualities. The Al grains are extended in the extrusion direction, and the microstructure in the core of the scroll wrap demonstrates clear directionality. Because of the low degrees of deformation, the microstructures of the end plate and top part of the wrap maintain cast structures[147].

True stress true strain curves of 6082 aluminium alloy were generated using high temperature compression experiments at temperatures ranging from 460°C to 560°C and strain rates ranging from 0.01 s^{-1} to 10 s^{-1}. On the basis of the - curve, the effects of deformation temperature and strain rate on the microstructure are explored. The dynamic recrystallization critical stresses of the 6082 aluminium alloy model were determined. Lower strain rates were found to be beneficial in increasing the volume fraction of recrystallization, but the average

recrystallized grain size was coarse; high strain rates were found to be beneficial in refining the average grain size, but the volume fraction of dynamic recrystallized grain was less than when low strain rates were used. As the dislocation density was lowered and the driving power for recrystallization was reduced, coarse grains persisted. The recrystallization critical point of 6082 aluminium alloy during thermal deformation may be accurately predicted using a dynamic recrystallization critical strain model and thermal experiment findings[148].

This report shows findings from a research of Al-2wt percent Si-5wt percent Mg and Al-4wt percent Si-5wt percent Mg alloys produced by conventional casting and ultra-refining. The results are compared to those of a commercial Al-7wt% Si-05wt% Mg alloy. Also shown is the material's morphological progression while re-heating to generate solid fractions of 45 and 60 percent in four different holding durations of 0, 30, 90, and 210 seconds. After re-heating, Rheocast Quality Index (RQI) and Shape Factor (SF), parameters that serve to measure the efficiency of the treatment globularization to generate semi-solid structure with globular structure, were conducted. The morphological evolution of the structure revealed that increasing the holding period resulted in a small increase in the globule size. For alloys with a high proportion of Si, the RQI values show little morphological variation in the treatment of globularization, indicating alloys with a low amount of Si[14]. As a result, it's critical to look at microstructural evolution and modelling in order to predict DRX grain size by taking into account variables like temperature, strain rate, and the impact of porosity.

2.8 FEM aspects in deformation

Extensive technological trials are frequently used to optimize process parameters for extrusion. The Finite Element Method (FEM) is a computer simulation technique that can be used to forecast the best temperature-strain rate conditions in extrusion. In 1941-1942, the first attempt to return FEM data to work was made. It was improved and given a mathematical formulation [149] after decades of development. FEM is a numerical technique that was first used to examine the behavior of structures for diverse real-world applications in structural mechanics [136]. Forging and die forging [150], [151], hot rolling [152], [153], and hot extrusion[154] have all been effectively simulated using FEM. Many studies have utilized FEM models to investigate physical and mechanical characteristics, recrystallization prediction, and grain size evolution in recent years [155], [156]. Nowadays, the FEM technique has progressed to the point that it can be used to analyze, forecast, and simulate the deformation, friction, and densification behavior of materials in a variety of metal forming

processes. It has advanced the level of engineering design by saving time, effort, and money in the production of final engineering goods.

DEFORM is a dependable and useful computer program for simulating complex metal forming operations. The following are three key components of the DEFORM software:

Pre-Processor: is an interactive tool that prepares input data for analysis and guides users through the simulation process. It includes: a) an interactive data input and verification model that includes die surface description, material properties, interface properties, and FEM meshes for the dies and workpiece, b) an automatic mesh generating program, and c) an interpolation module; and d) an automatic mesh generating program.

The simulation engine: To address the problem, it uses numerical calculations. The basic constitutive equations and boundary conditions can be changed to non-linear equations in the simulation engine by using FEM discretization, according to Kodayashi et al. [282]. After solving the problem using data from the data base as input, the answer data is saved in the database and presented or plotted using the post processor.

Post processor: It shows contour plots of field variables, velocity, stress, strain, strain rate, density, damage, and temperature, as well as load-stroke curves, in a graphic or alphanumeric form. The "flow net" module is also used to compute and display the flow path of a specified element, as well as the "fibre" or grain flow in the work piece.

This paper presents an experimental–numerical technique for forecasting the recrystallized structure in aluminium extrusion, as well as its confirmation. The strategy is broken down into three steps: in the first, the evolution of the microstructure of an AA6060 alloy during deformation was investigated using a small-scale laboratory test, with processing parameters chosen to mimic typical industrial conditions. The investigation of microstructure evolution after heat treatment (550°C for 30 minutes and 180°C for 10 hours) was performed in the second step, with the results being utilized to fit a recrystallization model to be applied within the Deform FEM code environment. The simulation results are then compared and discussed with the experimental grain size distribution examined on the extruded remainder in the third phase. A mean inaccuracy of 12% was discovered, with a maximum divergence of 57%, resulting in an intriguing agreement with the experimental results. The most significant differences are frequently found at the lowest temperatures and in the higher sections of the cups, where tool misalignment might result in homogenous deformation [157] and, as a result, a non-symmetric wall thickness distribution in the specimens.

The FEM approach was used to numerically model the densification process of Fe/Al composite powders exposed to uni-axial die compaction. The overall relative density and compaction pressure of compacts with varied Al concentrations were first determined. The effects of compaction pressure on the aforementioned properties with a fixed Al content were then discussed. In addition, the flow characteristics of the composite powders during compaction were studied in depth. When the Al content is fixed, higher compaction pressure can lead to composite compacts with higher relative density [158], and (1) the equivalent Von Mises stress in the central part of the compact increases gradually; (2) the relative density distribution tends to be uniform.

Using the commercial finite element (FE) tool ABAQUS^{TM}, a mathematical model was created to predict the through-thickness thermal and deformation history of a sheet undergoing single stand hot rolling in this study. To forecast the evolution of the material stored energy and subsequent recrystallization after deformation, a physically based internal state variable microstructure model has been introduced into the FE simulation for an AA5083 aluminium alloy [157]. Experimental measurements of an AA5083 aluminium alloy were used to validate the microstructure predictions. Under a variety of industrially relevant hot deformation circumstances, the model was able to forecast the fraction recrystallized as well as the recrystallized grain size quite well. To investigate the impact of modifying the material constants in the microstructure model and deformation circumstances on the expected recrystallization behaviour, a sensitivity analysis was performed. The most sensitive process parameter, according to the investigation, was the entrance temperature.

The purpose of this research was to look into the dynamic recrystallization of a novel Al-2.8Cu-1.4Li alloy [158]. To identify material constants for empirical models, isothermal compression tests were performed at a temperature of 643 K to 723 K (370 °C to 450 °C), a strain rate of 0.001 to 1 s^{-1}, and a deformation degree of 20 to 50 pct. The effect of initial grain size on microstructural evolution was studied using different holding durations ranging from 10 to 30 minutes. The constitutive model and dynamic recrystallization mathematical model of Al-2.8Cu-1.4Li alloy were developed based on the results of stress-strain curves and metallographic research. The microstructural change during hot upsetting was simulated using a coupled thermo mechanical FE method combined with a dynamic recrystallization model. The predicted and experimental results were found to be in good agreement.

The investigation on flow behavior of metals in extrusion billets is essential for comprehending extrusion technology. The behavior of extrusion billet skin and product microstructure must be investigated in order to maintain extrusion quality. Experimental and Finite Elemental analysis of clad billet extrusion were carried out to investigate the behavior [159]. The experimental and analytical results of billet skin deformation were very close. The deformation of the skin and its penetration into the billet are affected by friction between the back end of the billet and the ram. Second, the microstructure of an extruded product may be predicted, as well as the state of recrystallization and grain refinement. The flow of skin material is unaffected by temperature distribution. The skin material flow is affected by the friction coefficient between billet and ram. Because the skin glides at the ram's surface, skin material flow is faster when the friction coefficient is exceptionally low. To increase the yield rate, it is preferable to make the material skin move somewhat across the ram surface. Recrystallization is linked to the distribution of strain rates. If the strain rate is not greater than 6.5 /s when the ram speed is chosen, no recrystallized structure will be obtained. The size of recrystallized grains has been linked to strain distribution. The region where the strain exceeds 3.7 is recrystallized with a single grain size.

Using FEM, Xinjian et al.[160] investigated the effect of process factors on the occurrence of surface fractures. According to the simulation results, a larger extrusion ratio has a greater impact on the start of surface cracks. With rising billet temperature, temperature difference between die and billet, and ram speed, surface fracture propagation increased as well. Marin et al.[161] used FEM to investigate the effect of temperature on the extrusion process. The findings showed that the optimum temperature values for die and billet allowed for an increase in extrusion process efficiency while also improving final product quality. The isothermal extrusion method ensures that characteristics are distributed uniformly throughout the extrudates. Xinjian et al. [144] also stated that using FEM to design extruded profiles is a very efficient and effective method, and that using a single temperature setting during simulation resulted in homogeneous microstructure and mechanical properties during the extrusion process. Transient finite element simulation was used to find the optimal combination of process parameters for isothermal extrusion of Al alloys

2.9 Machine Learning models for phase identification

Aluminum alloy is frequently utilized in manufacturing industries such as aerospace, automobiles, and chemicals as the chosen metal material for lightweight [162]. Low density, high tensile strength, and high elongation are all characteristics of the 6-series aluminium alloy mentioned in this work. The distribution, shape, and size of microstructures all influence these qualities. These microstructures are visible in the metallographic image captured by the microscope. As illustrated in Fig.2.3, the aluminium alloy metallographic picture consists of the foreground (microstructure) and background (aluminium phase). The goal of metallographic image segmentation for aluminium alloys is to accurately distinguish and segment the microstructures from the given image pictures of metallography However, segmenting the microstructures is extremely difficult due to the extreme variety of aluminium alloy microstructures. The largest microstructure has a surface area of around 7330 pixels, while the smallest microstructure has a surface area of only 60 pixels, as shown in Fig. 2.3. Furthermore, microstructures come in a variety of forms. Recently, a growing number of academics have begun to focus on the problem of aluminium alloy metallographic picture segmentation. For metallographic images, a variety of segmentation approaches have been developed.

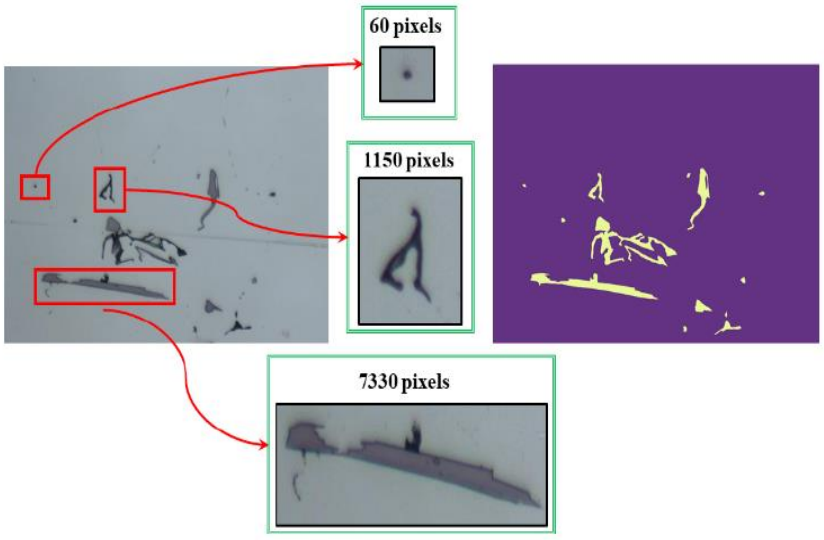

Fig. 2.3: Microscopically observed metallographic image (left), local expanded maps for microstructures (middle), and expert ground truth (right).

Image processing segmentation methods, machine learning segmentation methods, and deep learning segmentation methods have all been classified thus far. For example, Campbell

et al.[163] used a cascaded rule to segment microstructures in SEM and optical microscope pictures, which included filtering, watershed transform, region merging, and phase separation. Sun et al.[164] suggested a segmentation rule for grains and their borders in metallographic pictures by combining double-threshold binarization and morphological transform. These predefined guidelines are advantageous. The design of the established rules, on the other hand, may result in incompatibility between the fixed rule and the dynamically input metallographic images. That is, the rule is predefined and cannot be changed in response to input feedback.

Machine learning metallographic segmentation methods convert the segmentation challenge into a classification task and learn classifiers from a set of features and labels, removing the issue caused by image processing methods. Support vector machine (SVM) [165], multilayer perceptron [166], neural network [167], and optimum-path forest are some of the most often used classifiers in machine learning approaches.

Due to their excellent ability to learn discriminable features , deep learning has dramatically enhanced machine learning and achieved amazing results in picture segmentation [43][46]. More and more deep learning metallographic segmentation algorithms have been presented in recent years [47][48]. Although these metallographic image segmentation methods have shown to be effective, model learning often necessitates a significant number of pixel-level labelled pictures. This pixel-level classification activity frequently necessitates the time and effort of experts. Existing deep learning metallographic segmentation approaches face significant hurdles as a result of this circumstance. Such a problem configuration falls within the category of semi-supervised learning in machine learning[168] .

Semantic segmentation is a common problem in computer vision, and it's being used in a variety of applications such as self-driving cars and virtual reality. For microstructure segmentation, traditional segmentation methods such as thresholding or the watershed algorithm are not as precise. Convolutional neural networks (CNN) are frequently utilized in image processing and analysis, such as picture segmentation and detection. As a result, they've become the cutting-edge method for working with photos. Convolutional, activation, and pooling layers make up the majority of CNN architecture. The layers are placed one on top of the other in a pattern that repeats.

Advanced CNN models take care of the work of finding features and associating them to the desired output variable automatically. Manual interaction is not required to quantify any

features, removing a key source of bias. It can be extremely useful in cases involving complex microstructure aspects.

Qui et al [169], using tailored approaches and machine learning techniques, the microstructures of Al-Si-Mg casting alloy were classified at varied cooling rates. The mechanical characteristics of the samples improved slightly as cooling rates were increased. Because of the identical cooling speeds, the microstructures of the samples were similar. The program was used in conjunction with user-modified machine learning algorithms to get high categorization rates of around 80% to 90%. The effect of the number of photos in training data on classification rates was investigated, and an appropriate number of images for training in the machine learning process was discovered.

The authors [170] suggest a hierarchical parameter transfer learning approach for automatic microstructure segmentation in aluminium alloy micrographs, which is a generalization of the traditional parameter transfer method. Multilayer structure, multinetwork structure, and retraining technology are used in the suggested method. It can take full advantage of the benefits of various networks and transfer network parameters in order of high to low transferability. A number of experiments are presented to demonstrate the efficacy of the proposed strategy. The solution outperforms four common segmentation methods with a segmentation accuracy of 98.88 percent.

A new metallographic picture instance segmentation framework was developed, which can attribute each pixel to a physical instance of a microstructure. The authors[171] employed Mask R-CNN as the basic network in this framework to complete the learning and recognition of an aluminium alloy microstructure's latent feature. Meanwhile, five distinct loss functions based on this architecture have been built, and their impact on metallographic picture segmentation performance has been compared. Several tests were carried out to ensure that the suggested framework was effective. Six alternative evaluation criteria were compared and studied in these trials, and constructive ideas for the evaluation of performance metrics of the metallographic image segmentation approach were presented. The proposed approach may achieve instance segmentation of an aluminium alloy metallographic image, and the segmentation results are acceptable, according to a large number of experimental findings.

2.10 Limitations in the literature survey

A few of the existing gaps in the literature are mentioned below as

1) Semisolid processing of Al alloys starting with powder metallurgy route has been rarely performed.
2) Conventional aluminium alloys like A356 and A357 have been studied extensively but no focus has been given for other Si compositions.
3) Semisolid works concentrating on the solidus temperature range are limited.
4) Microstructure modelling on the extrusion process has been sparse throughout the literature.
5) FE analysis on compaction and extrusion of porous materials has been few.
6) Machine Learning based Prediction Models are few or nil in the Thixo Extrusion of Al-Si Alloys

Chapter 3

Experimental Methods and Characterization Techniques

3.1 Introduction

This chapter discusses the experimental setup and equipment used in the present research. The details of the equipment as well as the specifications used for manufacturing, material selection, sample preparation, hot extrusion testing, metallurgical examination using optical microscopy, and scanning electron microscopy (SEM) and estimation of mechanical properties are presented.

3.2 Materials Selection

The materials selected for the present investigations were pure aluminum (Al), silicon (Si) and magnesium (Mg). Al and Mg powder with 99.9% purity with a maximum of 0.5% insoluble impurities and Mg powder with 99.96% purity with a maximum of 0.5% impurities were supplied by Alfa Aesaer, USA. The mesh sizes of Al, Si and Mg were ~ 325, ~ 200 and ~ 36, respectively. The main reason for choosing these materials was the extensive use of their alloys / composites in numerous structural applications such as aerospace, automotive, defense, transportation, construction, architecture, etc. In addition, literature studies pertained to the deformation and densification of the selected materials are scarce. P / M processed components have a higher practical and industrial importance than the corresponding wrought materials with the same composition. In general, the morphology of the raw powder plays a crucial role in the development of the mechanical properties of materials produced by the P / M process. Therefore, micrographs of Al, Si and Mg powders are shown in Fig. 3.1, 3.2 and 3.3. Al and Si powders consist of particles with a semicircular, spherical and irregular shape. The average particle size (D) of Al was 45 μm (Fig. 3.1) and that of Si 15 μm (Fig. 3.2). Due to the mechanical grinding process, Mg powder particles look like a flaky morphology with an average particle size (D) of 147.0 μm (Fig. 3.3).

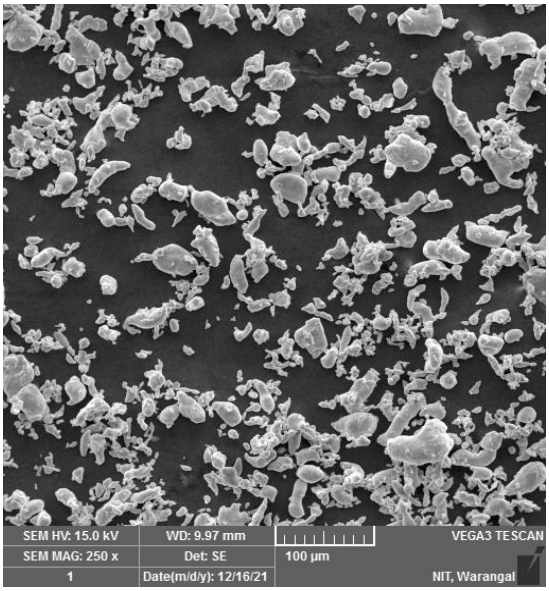

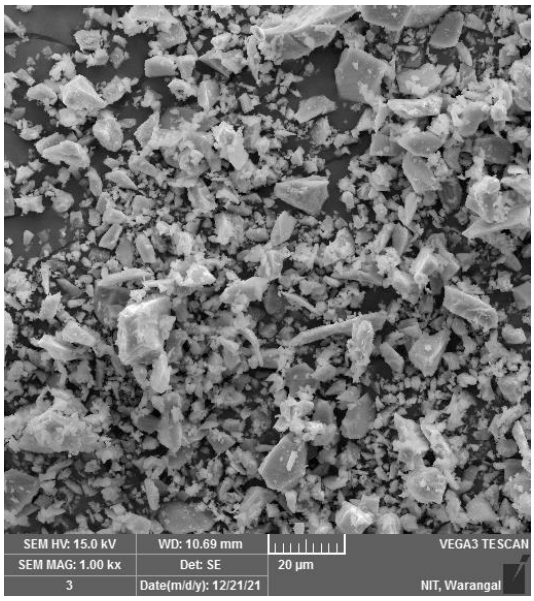

Fig. 3.1 SEM image of Aluminium powder **Fig. 3.2** SEM image of Silicon powder

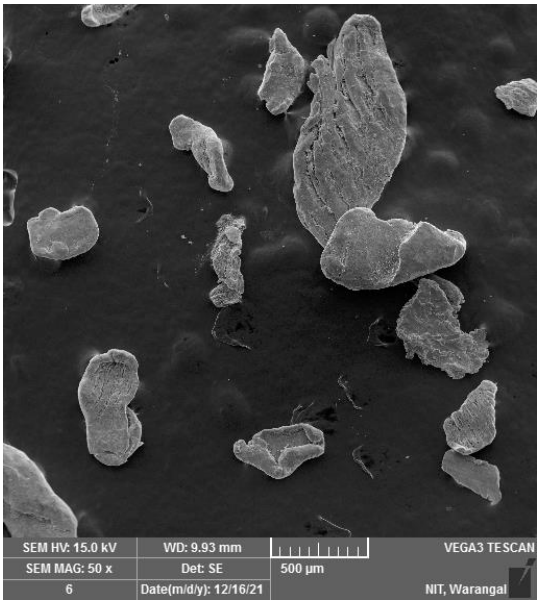

Fig. 3.3 SEM image of Magnesium powder

3.3 Specimen preparation

3.3.1 Mixing

The required mass of Al, Si and Mg powders was accurately weighed using an electronic mass balance (0.01 mg repeatability) and mixed in a mortar and pestle manually

obtain a homogeneous mixture. Aluminum powder was mixed with Silicon (1%-7% by weight) and magnesium (0% by weight, 0.2% by weight, 0.4% by weight, 0.6% by weight and 0.8% by weight) powder to create light and strong aluminum-based powder metallurgical alloys. The homogeneous powder mixture has the advantage that the sinterability of the powder is improved and the ejection of the pellets is made easier.

3.3.2 Hot Compaction

Among several compaction methods, uniaxial compaction has been used to produce powder compacts because it is by far the most economical and important method. Uniaxial compaction involves compressing a powder mixture within a mold cavity by the action of an upper punch at a constant speed while the lower punch remains fixed. Fig. 3.4 shows the image of the uniaxial compaction experimental setup used in the current work for sample preparation. A hydraulic press with a capacity of 25 tons from Kimaya Engineers, India, was used to produce Al-Si-Mg pellets. In this procedure, the required amount of the Al-Si-Mg powder mixture was properly poured into the die with the lower punch inserted from the lower part of the die and the upper punch inserted from the upper side. All green compacts were compacted by applying the recommended compacting pressure of 450 MPa heated to temperature of 570^{o}C and then held at this temperature for about 60 min and finally furnace cooled with the die assembly to obtain compacts with initial preform relative densities (IPRD) of around 90%, respectively. Cylindrical hot compacts with an aspect ratio (diameter 15 mm and height 15 mm) one were produced to obtain good dense compacts. Molybdenum Disulphide was applied to the walls of the die to minimize frictional effects between metal powder and die during compaction. After the hot compacting step was completed, the green compacts were carefully ejected from the die by turning the die upside down and applying an ejection load in the range of 50 MPa to 80 MPa. Molybdenum disulphide should decompose during the sintering cycle due to the low operating temperature / melting point, and small residues of Molybdenum disulphide that remain after sintering do not impart any appreciable effect to the end parts. Fig. 3.5 shows the press die, punch and piston made of high-strength tool steel with a diameter of 15 mm, which are used to manufacture powder compacts for hot extrusion tests. The green compacts were hot compacted at 510 ° C., 530 ° C., 550 ° C. and 570 ° C. with a heating rate of 10 ° C./min in the oven for 1 hour before cooling. The compacts were then allowed to reach room temperature in the oven after completion of the sintering schedule. Fig. 3.6 shows the images of Al-Si hot compacts

Furnace specifications:

Inner diameter: 50-70 mm

Maximum temperature: 600 °C

Working temperature: 500 - 600 °C

Power requirement: 3 kW

Voltage: 220 V/ Single phase/60/50 Hz

Fig. 3.4: Hydraulic press with furnace

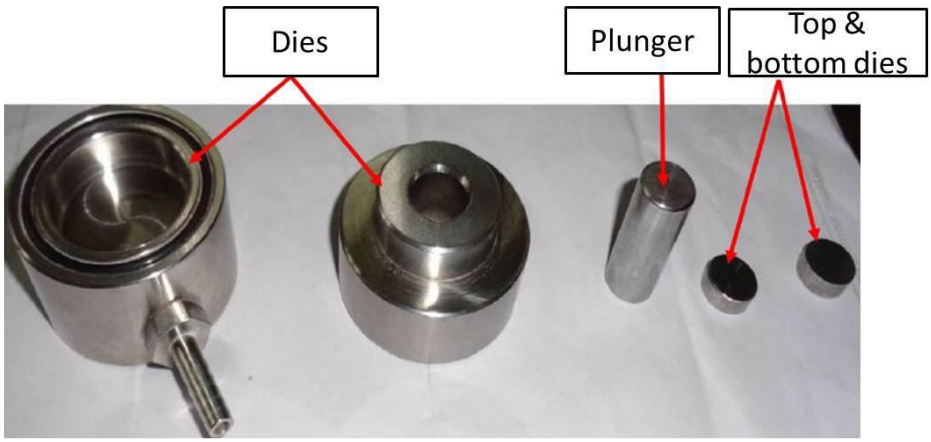

Fig. 3.5: Images of die punch setup

Fig. 3.6: Al-Si hot compacts

3.4 Differential thermal analysis (DTA)

The semi-solid forming process requires 60-80% of the solid content to produce the best quality products. The solids content of a material has a significant role that affects the viscosity of the semi-solid slurry. The end product of the semi-solid extrusion coexists between solidus and liquidus temperatures. Therefore, DTA was used to determine the solidus and liquidus temperatures and the solidification interval of the Al-Si-Mg preforms. Samples weighing 15 mg were cut and placed in the alumina pan in a nitrogen gas atmosphere. The samples were then heated between 200 ° C and 700 ° C at a rate of 2.5 K / min. The curve obtained by DTA was used to calculate the change in solid-liquid proportions with temperature. The semi-solid extrusion tests were carried out in the temperature ranges between solidus and liquidus temperatures, which were obtained from the DTA studies, in order to have a minimum to maximum range of solids content in the specimens. The percentage of solids at any given temperature within the freezing limit is given by the Scheil equation. Fig. 3.7 shows the photo

of the DTA instrument from Ametek Scientific Instruments, USA (software: Versa Studio 2.52.3).

Fig. 3.7: Photograph of TG/DTA equipment

3.5 Semi-solid extrusion/Hot extrusion test

Semi-solid extrusion tests were conducted to understand the effect of the solid content and the liquid content in the preforms during deformation, and the effect of strain rate on the specimens. A sequence of semi-solid extrusion tests were conducted using a hydraulic press with a capacity of 50 tons supplied by SVS Hydraulics (P) Ltd, Hyderabad, India. First, semi-solid extrusion tests were carried out on optimized Al-4% Si P / M preforms in the temperature range between solidus (550 °C) and liquidus (600 °C) temperatures, which were found from the DTA experiments and then on Al-4% Si-0.6% Mg P / M preforms . Extrusions of the sintered preforms were performed with extrusion ratios of 4, chamber diameter of 15 mm, exit diameter of 7.5, contact length of 2.5 mm and approach angles of 60 for 3 different operating temperatures of 550 ° C, 575 ° C and 600 ° C, respectively. Fig. 3.8 shows the images of extrusion die setup. An incremental load was applied until the sintered preforms were fully extruded. The deformation processes were performed by mounting extrusion dies in a split-type electric resistance furnace equipped on the bed of a hydraulic press. To measure the furnace temperature and the billet temperature, two thermocouples were placed in the oven,

one of which was placed in the oven and another near the preform. A holding time of 20 minutes was observed to allow the granules to globulate and to achieve a homogenous temperature in the sample after the required test temperature was reached prior to deformation. The deformation load and displacement were continuously monitored by the data acquisition system connected to the hydraulic press and the data were recorded after each extrusion test.

Fig 3.8: Extrusion die of ratio 4 and approach angle 60° with plunger

3.6 Development of constitutive equations for modeling

Warm extrusion tests were performed to analyze the deformation behavior and establish a mathematical models to predict DRX grain size for preforms that were deformed at various processing temperatures and strain rates. Hot compacted pellets with an aspect ratio (diameter 15 mm and height 15 mm) were fabricated to attain highly dense compacts. All pellets were compacted by applying the recommended pressures to obtain samples with an IPRD of 90%, respectively. Before extrusion, sintered preforms were soaked for 30 minutes at a test temperature in order to ensure a uniform temperature distribution. All samples were then air-cooled in order to obtain a uniform microstructure and also to know the degree of deformation of the DRX grain size. In order to describe the deformation mechanisms of materials and to determine optimal processing sizes, it was essential to examine the constitutive modeling under different deformation conditions

Load-displacement diagrams were obtained using the data logger connected between the computer and hydraulic controller unit. Experimental results and constitutive modeling

results were compared to observe the correctness of the formulated model for P / M fabricated Al-4% Si-0.6% Mg preforms.

3.7 Microstructural investigation

Since most of the material's strength results from recrystallization, precipitations and dispersoids during the sintering and deformation process, all sintered and extruded samples were examined by optical microscopy, SEM / EDS and XRD. Specimens for metallographic studies were initially polished with silicon carbide emery paper of various grain sizes. The specimens were then polished on a disk polishing machine using polishing cloths of different grades and diamond suspensions until they reached a highly polished surface. The polished samples were etched in Keller's reagent for 60 seconds. Optical metallography was performed using a Quasmo ISI microscope with a micrometric digital camera (software: Quasmo iview 3.7) as shown in Fig. 3.9. A VEGA 3 LMU (TESCAN) SEM was used to capture the microstructures of polished samples, where it was operated with a beam current of 10 mA and an accelerating voltage of 20 kV. Elemental analysis was performed by Energy Dispersive Spectroscopy (EDS) supplied by Oxford Instruments, UK (software: INCA 5.03). Fig. 3.10 shows the scanning electron microscope with EDS connection.

Microstructure analyzes were carried out using optical microscopy and SEM for extruded samples with different regions deformation temperature, strain rate. The grain size of all samples was measured using the standard line intercept method. X-ray diffraction (XRD) was also used to obtain a qualitative analysis of the phases that exists in the samples. The XRD unit equipped with a copper X-ray source (CuK) was operated with a voltage of 45 kV and a current of 30 mA.

Fig. 3.9:Photograph of optical microscopy

Fig. 3.10: Photograph of scanning electron microscope

3.8 Mechanical properties evaluation

A systematic study was done to determine the structure-property relationship of Al-Si-Mg-P / M alloys in relation to extrusion temperature and strain rate. Densities of sintered and extruded parts were measured according to the Archimedes principle with an error of 1%. The Shimadzu micro hardness testing machine (Fig. 3.11) was used to measure the hardness of sintered and extruded samples with an applied load of 500 g and holding time of 15 seconds (test force time on the sample).

Fig. 3.11: Photograph of Microhardness tester

3.9 Numerical Modeling

The FEM modeling of hot compaction and hot extrusion tests was carried out with the DEFORM 2D software, as shown in Fig.3.12 and Fig.3.13. An axially symmetrical formulation of the billet was taken into account for the modeling. A square nodded 2000 elements with a size ratio of 3 was used to mesh the billet. An optimized composition was chosen as the sample in the present research topic. The diameter and length of the ingot used for all simulations had an aspect ratio (diameter 15 mm and height 15 mm). The simulation of the hot extrusion process was carried out in DEFORM 2D because it makes sense to simplify the prototype as a flat model with 2D axis symmetry. The samples were modeled as porous materials with initial relative density as 90% entered as inputs into the model, while the die and stem were set as a rigid body. Based on the yield stress curves obtained during extrusion at various deformation temperatures, strain stresses and IPRD, the constitutive yield stress equation was created using a hyperbolic-sine relationship (Arrhenius equation) and imported into the DEFORM 2D software. In all simulations, constant shear friction between tool and work piece and a coefficient of friction m = 0.4 between upper tool and work piece and work piece with lower tool were assumed. In simulation studies, a nozzle with an extrusion ratio of 4 and an approach angle of 60 was used because these gave good experimental results for semi-solid extrusion. .In order to verify the experimental results with simulation results, the same deformation temperature, strain rate and IPRD were used in simulation studies as in the hot extrusion studies. The simulation parameters are shown in Table 3.1.

Simulation parameter	**Value**
Temperature of the billet (°C)	550 °C, 575 °C, 600 °C
Strain rates	$0.1s^{-1}$, $0.2\ s^{-1}$, $0.3\ s^{-1}$
Extrusion ratio	4
Die approach angle	60°
Coefficient of friction	0.4 [172]

Table 3.1: Simulation conditions for hot extrusion

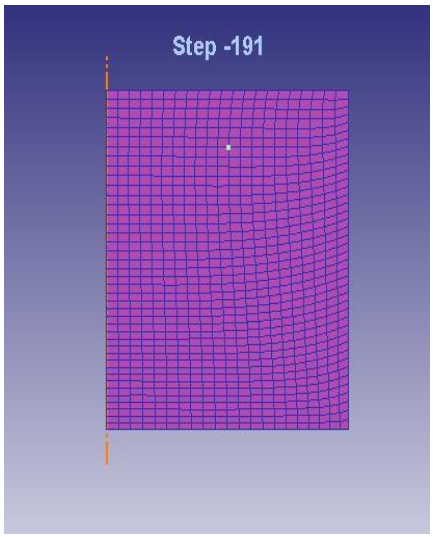

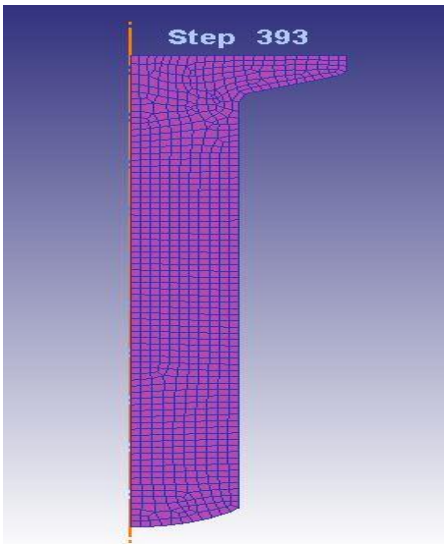

Fig. 3.14: FE model for hot compaction

Fig. 3.15: FE model for hot extrusion

3.10 Microstructure Modelling

The material Al-4Si-0.6Mg alloy powdered compacts were prepared through uniaxial hot compaction process to achieve an average relative density of 90%. Relative density of the specimens were evaluated using Archimedes principle. Firstly, cylindrical specimens with dimensions of 15mm height and diameter 15mm were hot compacted at 550^0C. In order to model the grain growth, hot compression tests have been performed. Specimens were heated to semisolid temperatures namely 560^0C, 580^0C, and 600^0C with a heating rate of 10^0C/s and holding times of 600 s, 1200 s and 1800 s. Following this, the specimens were quenched. Secondly, the dynamic recrystallization model has been formulated by conducting hot extrusion tests at 560^0C, 580^0C, and 600^0C with strain rate of 0.1 s^{-1}, 0.2 s^{-1}, and 0.3 s^{-1}.The extrusion die was a split type with 60^0 approach angle with an extrusion ratio of 4. Molybdenum Disulphide was used as a lubricant to reduce the friction between the walls of the die and work piece. The samples were sectioned along the longitudinal axis, ground, polished and then etched with Keller's reagent to reveal the grain boundaries. Optical microscope was used to view the grains and the grain size was measured using ImageJ software. The measured grain size data were used in the regression equations to predict the dynamic recrystallization

undergone by the samples. Thirdly, numerical simulations were done and the grain size results were compared with the extruded grain sizes.

3.11 Deep learning for phase identification

In this section, from the microscopic images the features of interest are predicted based on deep learning algorithms. Deep learning models can be either supervised (trained by means of known values) or unsupervised. Here, the image segmentation part is done by image labeler software and analysis has been carried out by various deep learning algorithms. In this technique, each image is converted into a labelled image with a label being assigned to each pixel such that pixels within the label have similar characteristics. First step in the process of classification is feature extraction. Feature extraction involves recognizing the interesting areas in the micrograph like particular phases, defects etc. The labelled images are the feature vectors that contain the digital information about the image which can be used for training and testing process. $\boldsymbol{\alpha}$-Al grains (white) are the features of interest excluding the porosity and secondary phases (black) in the micrographs. Image datasets used were the micrographs of the extruded Al-Si-Mg alloys. The dataset consists of 80 images with the pixel size of 1280 by 960. Masking has been done using image labeler toolbox in Matlab software. The new image had a size of 500×500 pixels. Convolutional Neural Networks takes these masked images as the input and uses signal processing operations to encode it into a vector. This vector is utilized by an artificial neural network to draw a conclusion about the image content. The architecture of CNN called Unet has been utilized in this work. It can be divided into two parts with the left side representing the contracting path in which the feature map is encoded by utilizing convolution and max pooling operations. The right side represents the expansive path in which the feature map is decoded into output segmentation image by up sampling it. By utilizing concatenation methods, the feature maps in contraction side are merged with the expansion side. One advantage with this model is that it achieves better accuracy even with small datasets.

Chapter-4

Mechanical and Metallurgical Studies on Thixoextruded Al-Si alloys

4.1 Introduction

The aim of the present work is to study the application of Al-Si Powder Metallurgy (P/M) alloy in the thixo extrusion process and to evaluate the properties before and after extrusion. Al-Si P/M alloys were prepared for various Si compositions (1%-7%) and Mg compositions (0.2%-0.8%). The best among the Al-4Si and Al-4Si-0.6Mg were selected based on hardness and density results. Differential Thermal Analysis revealed the solidus and liquidus temperatures to be 557^{o}C and 642^{o}C for Al-Si alloy and 564 ^{o}C and 636 ^{o}C for Al-4Si-0.6Mg alloy respectively. Compaction temperature and Holding time studies have been carried out and the corresponding optimized parameters are found to be 550^{o}C and 60 mins. Thixoextrusion was performed on the hot compacted preforms for three temperatures namely 560 ^{o}C, 580 ^{o}C and 600 ^{o}C respectively. An extrusion ratio of 4:1, strain rates of 0.1s^{-1}, 0.2$s^{-1}$and 0.3s^{-1} and die approach angle of 60^{o} were used for the tests. Extrudates were divided into three regions namely front, middle and end parts to analyze its mechanical and metallurgical properties.

4.2 Al-Si alloy

4.2.1 Optimization of Si Composition

To find the best Si composition, the mass percentage of silicon is varied from 1-7%, while rest of the process parameters was kept constant. Composition above 7% leads to collapse of the billet due to high liquid fraction present in the material as suggested by Zoqui[15]. The effect of silicon on the relative density of the specimen is shown in Fig. 4.1a. Addition of silicon leads to an increase in the relative density up to 4% and then it decreases. This decrease can be attributed to the increased liquid content of the specimen. The liquid content being 35.3%, 43.4%, and 51.6% for 5, 6, and 7 percentages of silicon as predicted by Thermocalc software. Fig.4.1b shows the hardness profile for the Al-Si alloys. The hardness of the compacts increased with the increasing silicon percentage as expected and there was no significant change beyond 4% with only small variations.

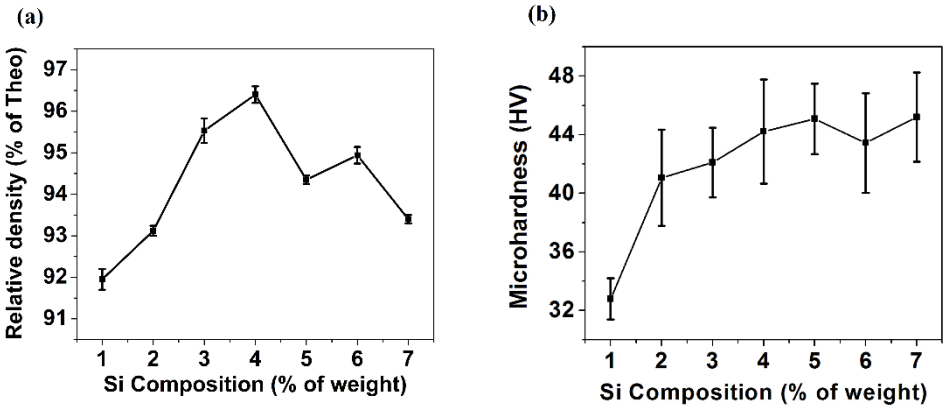

Fig. 4.1a) Silicon composition vs Relative density **b)** Silicon composition vs Microhardness

4.2.2 X-ray Diffraction Analysis

XRD analysis was done to verify the presence of intermetallic phases in the alloy. It is found from Fig. 4.2 that there is no other phase in the Al-4Si alloy except the α-Al phase and the primary Si phase. Similar results are found in the study performed by Akyuz B[15].The binary phase diagram of Al-Si also confirms the absence of any intermetallic phase. As the percentage addition of silicon increases the intensity values also increase which is reflected in the XRD pattern.

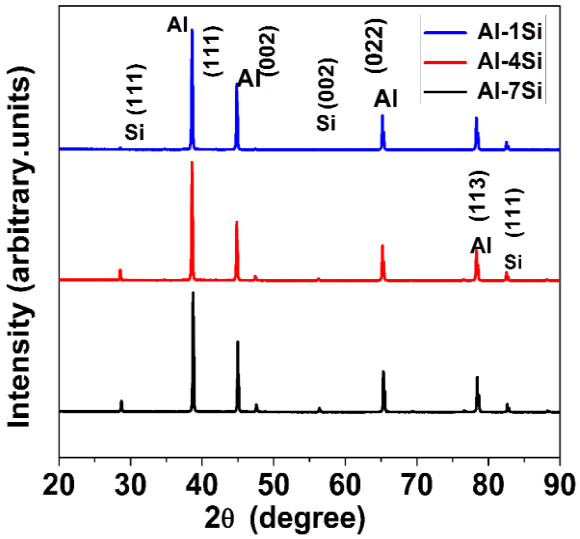

Fig. 4.2: X-ray diffraction pattern of Al-Si alloy

4.2.3 Optical Microscopy and SEM Studies

Metallographic studies including both optical as well as SEM with EDS have been performed. Fig. 4.3a shows the optical microstructure image of the Al-4Si alloy. Conventional casting process produces dendrite microstructures which are not favored because of their weaker mechanical properties [15]. Alloys prepared through P/M technique have globular or near globular structures which are prerequisite for thixo-forming process. Microstructure also reveals the presence of α-Al phase (yellow) and the primary-Si phase (grey). Fig. 4.3b shows the SEM and the EDS results which also confirm the presence of Al and Si elements in the alloy.

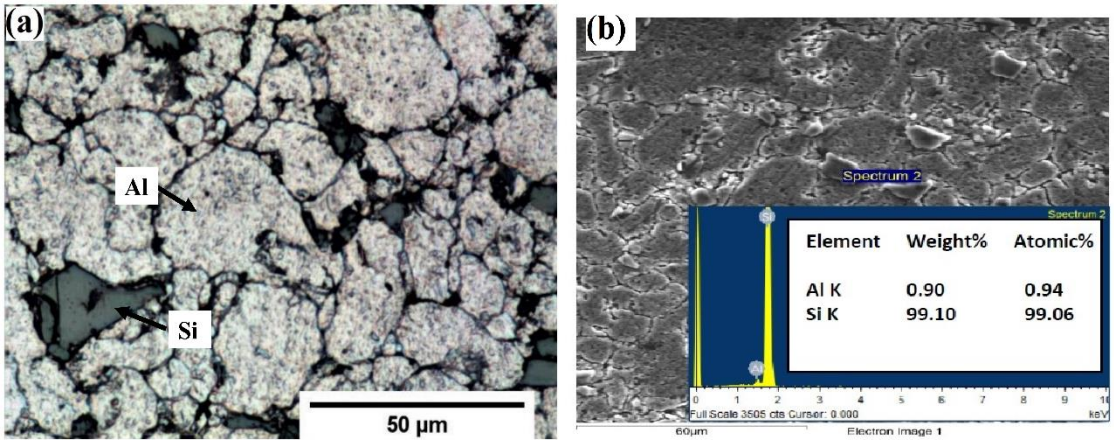

Fig. 4.3a) Optical micrograph of Al-4Si alloy **b)** SEM and EDX graph of Al-4Si alloy

4.2.4 Differential Thermal Analysis

DTA analysis was carried out to find the solidus and liquidus temperature of the sample. The Fig.4. 4 shows two endothermic peaks at 582ºC and 618ºC corresponding to the eutectic melting peak and the α-Al phase melting peak [15]. Solidus temperature and liquidus temperature of the specimen were found to be 557ºC and 642ºC respectively.

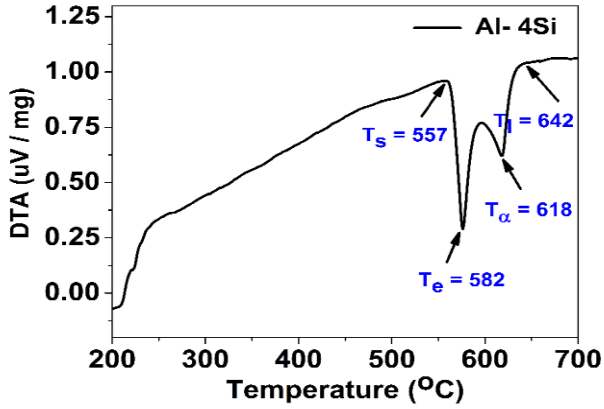

Fig. 4.4: DTA curve profile for Al-4Si alloy

4.2.5 Compaction Temperature Studies

Compaction temperature studies were done for four different temperatures namely 510°C, 530°C, 550°C and 570°C at a constant holding time of 60 mins. Fig.4.5a and b show the density and hardness graphs for the alloy. Fig. 4.6 shows the optical microstructure images of the specimens sintered at 530°C, 550°C and 570°C. Specimens fabricated through hot compaction have reduced porosity and with little shrinkage and swelling defects as compared to cold compaction and the grain size was also smaller. Specimens sintered at 550°C offered a higher relative density of 93% and hardness of close to 50 HV.

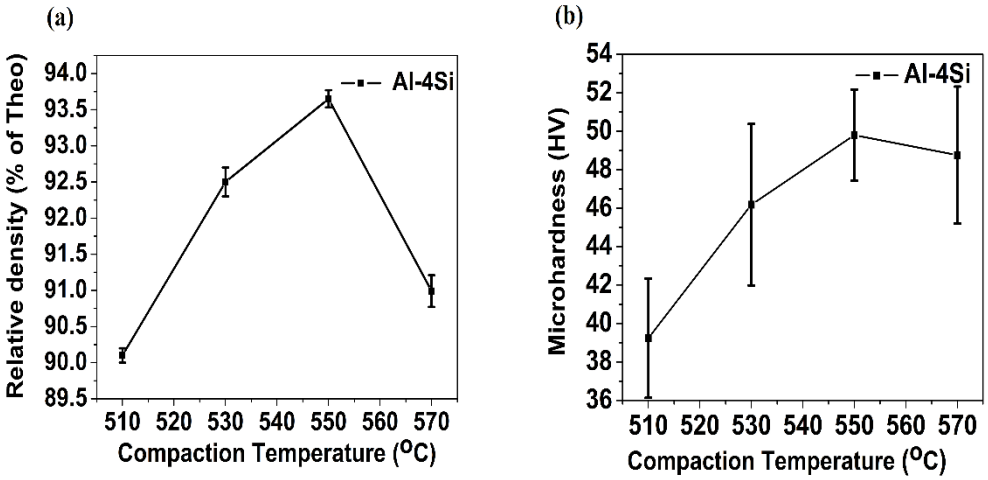

Fig. 4.5a) Compaction temperature vs Relative density

b) Compaction temperature vs Microhardness

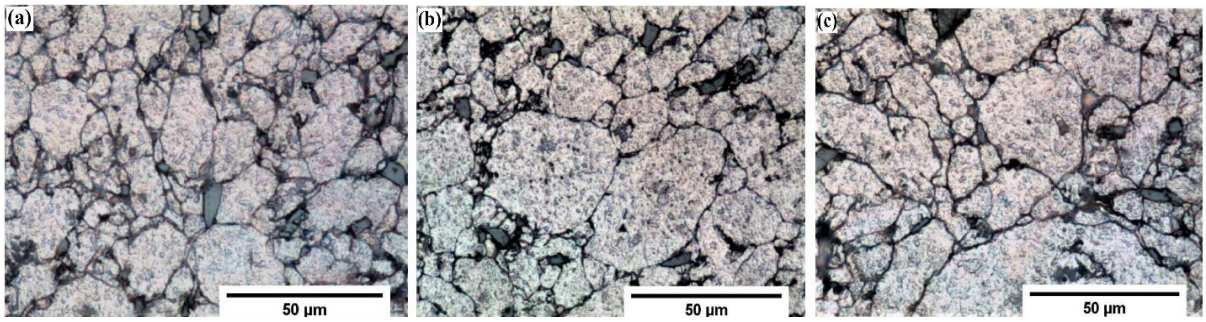

Fig. 4.6: Micrographs for Al-4Si alloy sintered at **a)** 530^{o}C **b)** 550^{o}C **c)** 570^{o}C

4.2.6 Holding Time Studies

Similarly holding time studies were also conducted for 20 mins, 40 mins, 60 mins, and 80 mins at constant temperature of 550^{o}C. The influence of holding time on relative density and holding time on hardness of the specimens are shown in Fig. 4.7a and b. Density increased with increasing time and showed a sudden peak at 80 mins whereas the hardness corresponding to 60 mins showed hardness of around 50HV. Density of the specimen increased because of more quantity of liquid filling the pores and thus making the specimen denser. But the specimens sintered at 80 mins had a poor surface finish because of powder sticking to walls of the die. The microstructure images corresponding to 80 min showed much bigger grains compared to 60 mins. Hence, holding time of 60 mins was chosen as the optimum holding time.

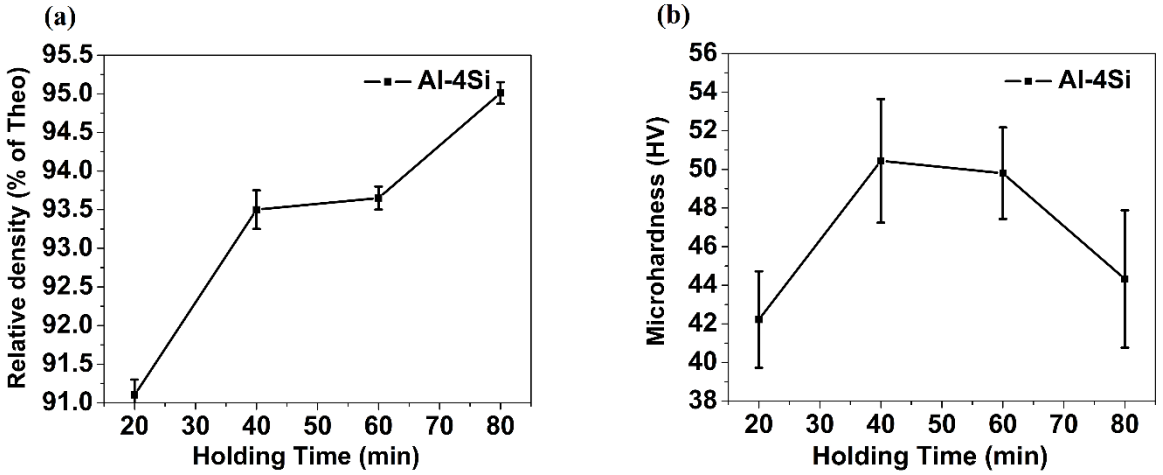

Fig. 4.7a) Holding time vs Relative density **b)** Holding time vs microhardness

4.2.7 Semisolid Extrusion

Thixoextrusion was carried out for temperatures of 560^{o}C, 580^{o}C and 600^{o}C selected from the TG/DTA results. Extruded specimens were free from surface defects. Specimens extruded at 600^{o}C were comparatively longer than the others at 560^{o}C and 580^{o}C because of higher liquid fraction in the specimen. Extrusion was performed for three different temperatures and three different strain rates namely $0.1s^{-1}$, $0.2s^{-1}$and $0.3s^{-1}$.The specimen was divided into three sections namely front end, middle part and rear end for analyzing the properties at different sections.

The solid fraction present in the specimen for any temperature was calculated by using Scheil equation

$$f_s = 1-(T_s-T/T_s-T_l)^{(1/1-k)} \quad \text{----------(4.1)}$$

where k = Partition coefficient = 0.13[173],T_s = Solidus temperature and T_l = Liquidus temperature

The corresponding solid fraction present in the specimen according to Scheil equation for 560^{o}C, 580^{o}C and 600^{o}C are 97%, 77%, 54% respectively.

Microstructural studies were done on the extrudates along the longitudinal direction as well as the traverse direction. Fig. 4.8 shows the microstructure of the specimen along the extrusion direction. Elongated grains are present along the extrusion direction which is the characteristic feature of extrusion process[174], [175]. However, the grain elongation is not uniform throughout the specimen because of the heterogeneous distribution of strain in the extruded specimens. Fibrous microstructure is the favored microstructure which can be found in the OM images.

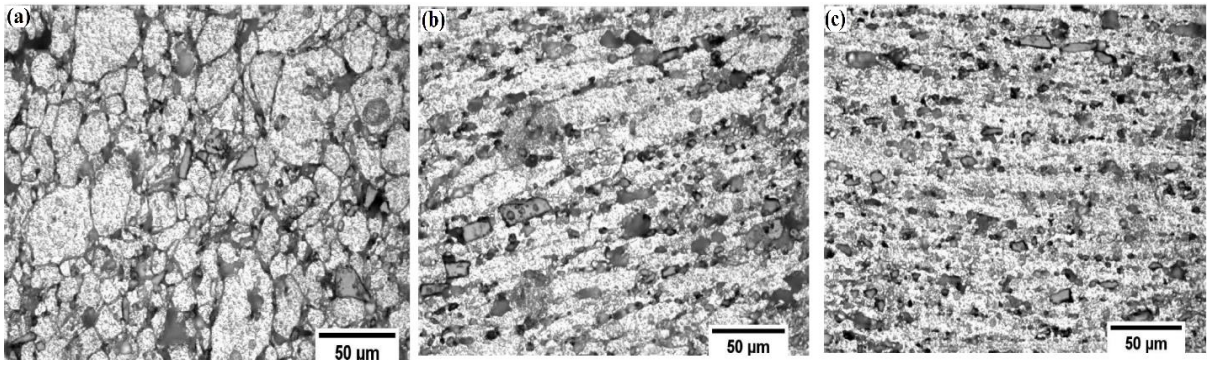

Fig. 4.8: Optical Micrographs along the extrusion direction of specimen extruded at 580^{o}C and strain rate 0.1s^{-1} **a)** front end **b)** middle part **c)** rear end

Hardness profile along the longitudinal direction fluctuates between 30 HV to 40 HV varying all along the length of the specimen. This variation can be attributed to the heterogeneity that exists throughout the specimen and the grain size variation between the center region and the outer periphery region of the specimen because of the differential strain within the sample. Higher hardness values were observed along the middle region whereas extreme values were observed at the front end and the rear end of the samples. Hardness values were also much lower along the extrusion direction as compared with the transverse direction. Fig. 4.9 shows the hardness profile of the extrudate extruded at 580^{o}C and strain rate 0.1s^{-1} along the extrusion direction.

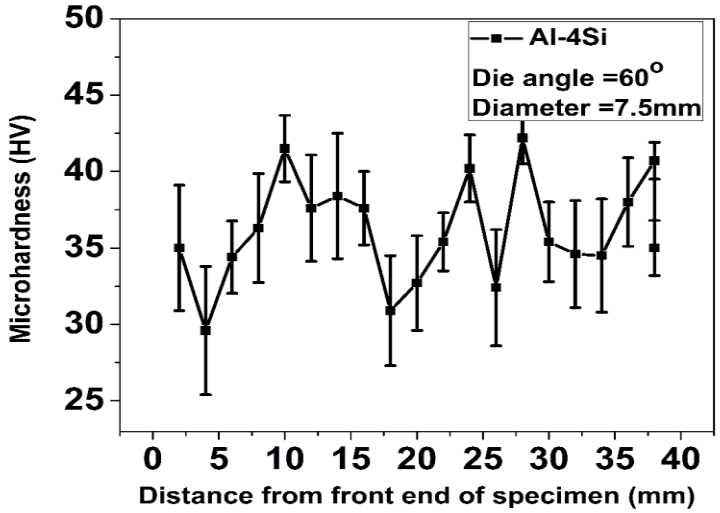

Fig. 4.9: Hardness profile along the length of the extrudates extruded at 580^{o}C and strain rate 0.1s^{-1}

Microstructural studies on the extruded specimen along the transverse direction were done by dividing the specimen into three sections namely front end, middle end, and rear end. It is evident from Fig.4.10 that microstructures at the front and middle ends of the specimens are almost globular whereas the rear end of the specimen had undergone much higher deformation resulting in finer non recrystallised grains[176]. The overall grain size of the extruded specimen is smaller than the hot compacted specimen. This globularity is because of the spherical grains produced by the powder compaction process. And the reduction in grain size was because of the extrusion process.

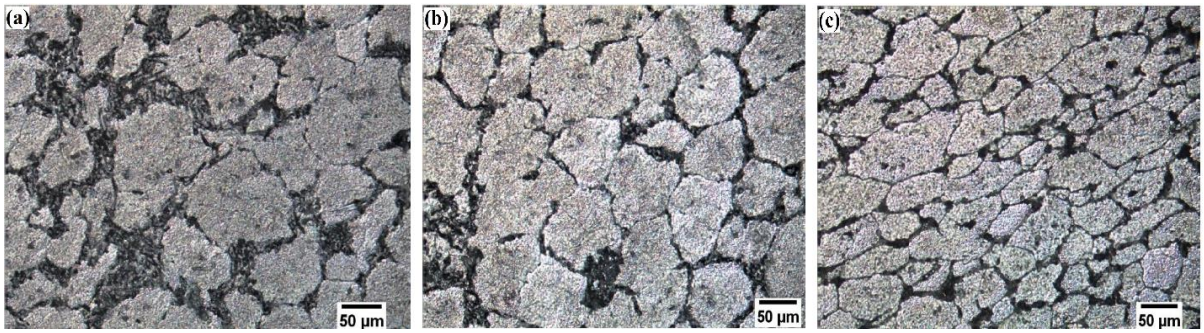

Fig. 4.10 Optical Micrographs s along the transverse direction of specimen extruded at 580^{o}C and strain rate 0.2s^{-1}**a)**front end **b)**middle part **c)**rear end

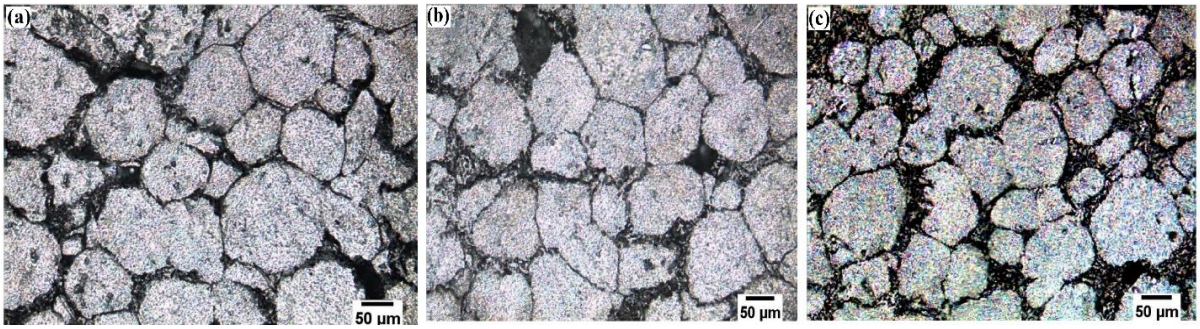

Fig. 4.11 Optical Micrographs along the transverse direction of specimen extruded at 600^{o}C and strain rate 0.2s^{-1} **a)** front end **b)**middle part **c)**rear end

Surprisingly specimens extruded at 600^{o}C showed a near uniform globular microstructure in all the three regions of the extrudate. As the temperature had crossed the eutectic temperature and the liquid content in the specimen had also increased due to the increased extrusion temperature, a near uniform globular microstructure has been achieved at 600^{o}C. Also, at 600^{o}C the silicon particles have transformed from flaky morphology to needle morphology as evident from the optical micrographs shown in Fig. 4.11.

As a result of exchange of heat between the billet material and the die, there is a non-uniform temperature distribution throughout the specimen which causes the segregation of liquid at the front and middle ends of the specimen. Thus, the middle and front ends have globular microstructure suggesting that there was no enough liquid content in the rear end of the specimen and the grains are formed more under the influence of deformation mechanisms suggested by Birol[176].

4.3 Al-Si-Mg alloy

4.3.1 Optimization of Mg Composition

In order to increase the properties of Al-Si alloys, small amounts of magnesium is added. The alloy age hardens and show better properties because of Mg_2Si precipitation [177]. The maximum solubility of Mg in Al-Si alloys in the presence of Mg_2Si is 0.8%. Therefore, mass of Mg is varied from 0.2%-0.8% and the better composition is optimized. Relative density and Hardness profiles for various composition of Mg are shown in Fig. 4.12a and 4.12b. As expected, the addition of Mg decreases the density of the compact compared to the Al-4Si alloys. While the Mg composition corresponding to 0.6% mass gives a marginally higher density. Similarly from the hardness graph, it was found that hardness values increases with the increasing Mg content reaching upto 42 HV which is almost close to the hardness of Al-4Si alloy (44 HV). An increase in the hardness of the sample can be found because of the large number of hard Mg_2Si precipitates as the Mg concentration increases. The composition corresponding to 0.6% of Mg is selected for further analysis based on the density and hardness values.

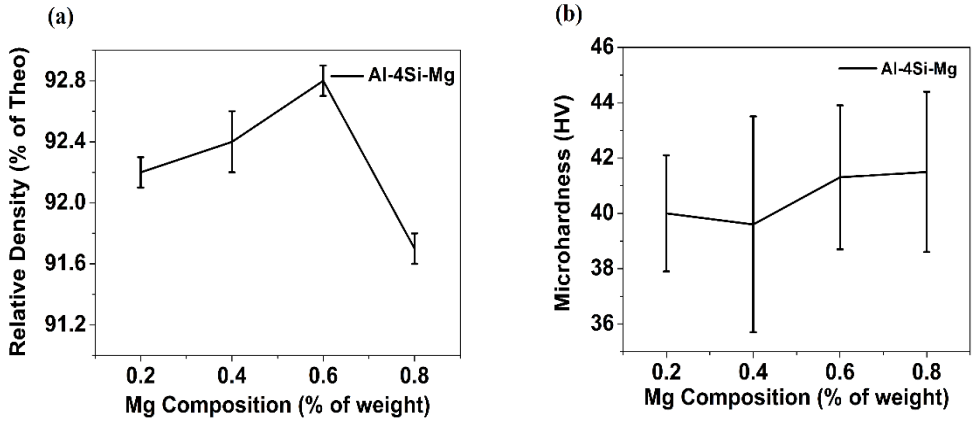

Fig.4.12a) Composition of Mg vs Relative density **b)** Composition of Mg vs Microhardness

4.3.2 Optical Microscopy and SEM Studies

OM images of Al-4Si-0.6Mg are shown in Fig. 4.13a and 4.13b. The image shows the presence of three phases namely α-Al phase (yellow), primary-Si phase (grey) and Mg_2Si phase (Fade appearance). Unetched image of the compact (Fig. 4.13 b) shows the presence of Mg_2Si phase in network like form. Coarse network structures which were not found in the Al-4Si alloys were observed in this Mg alloy. Ternary Al-Si-Mg phase diagram also has only the above mentioned three phases. Further ternary eutectic reaction, $L \rightarrow Al + Si + Mg_2Si$, also occurs under non equilibrium solidification conditions as stated by Hengcheng[178]. Further the author also suggests that Mg_2Si, grows on the habit planes on eutectic silicon flakes. EDS analysis confirm the presence of Al, Si, Mg elements in the alloy. The three-dimensional morphology of the eutectic Mg_2Si phase in the deep-etched Al-4Si-0.6Mg samples as shown in Fig. 4.14 a and Fig. 4.14 b confirms the presence of coarse lamellar structure as found by Ke-Yan Wang[179].

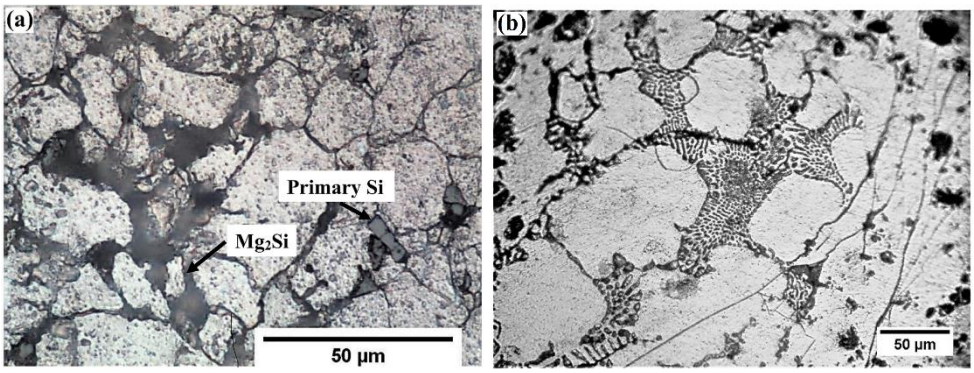

Fig. 4.13 a) Micrograph of Al-4Si-0.6Mg alloy **b)** Unetched image of Al-4Si-0.6Mg alloy

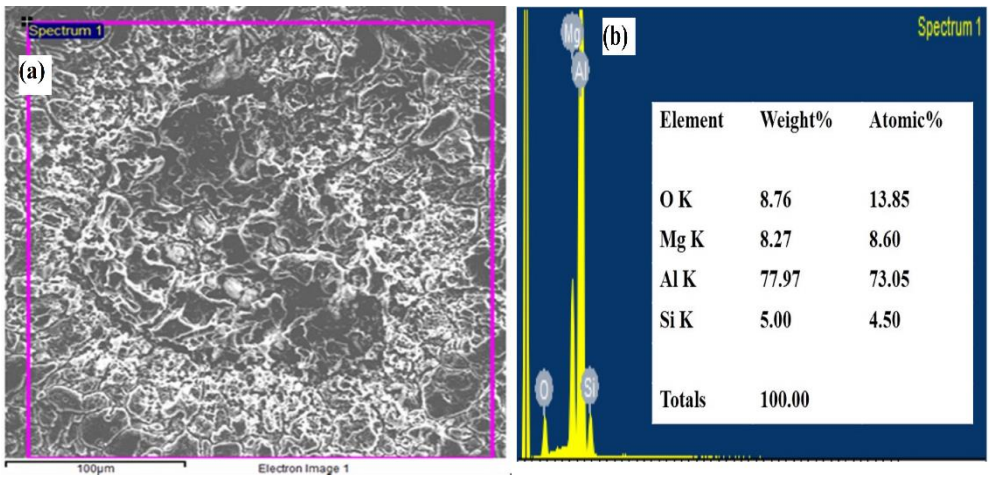

Fig. 4.14a) SEM image of Al-4Si-0.6Mg alloy **b)** EDS analysis of Al-4Si-0.6Mg alloy

4.3.3 Differential Thermal Analysis

Differential thermal Analysis was carried out to find the solidus and liquidus temperature of the alloy. DTA graph of Al-4Si-0.6Mg alloy is shown in Fig. 4.15. Solidus temperature was found to be 564^{o}C and the liquidus temperature being 636^{o}C with the processing temperature range of 72^{o}C. The eutectic temperature of the specimen being 573^{o}C. Clearly the addition of Mg has shifted the eutectic temperature of the specimen by 10^{o}C compared with the Al-4Si alloy (Fig. 4.4). The peak corresponding to the temperature 624^{o}C indicates the formation of α-Al phase. The ternary eutectic reaction involving Al-Si-Mg_2Si was missing as compared with the cast Al-Si-Mg alloys because the peaks might have overlapped with each other as suggested by G.Wang[177].

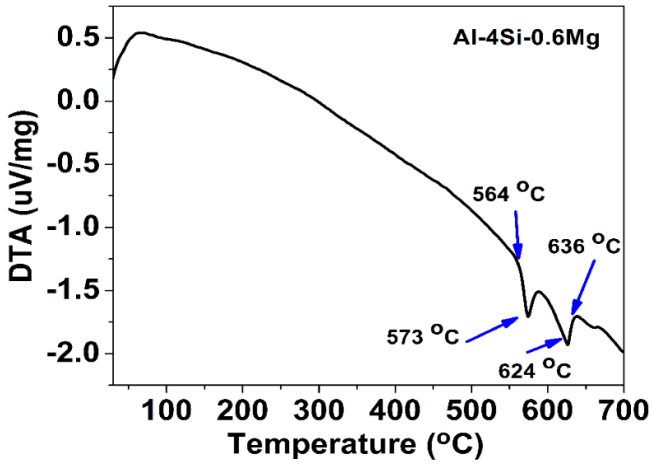

Fig. 4.15: Differential Thermal Analysis curve profile for of Al-4Si-0.6Mg alloy

4.3.4 Compaction Temperature Studies

Compaction temperature has to be optimized for better results. So four different temperatures namely 510^{o}C, 530^{o}C, 550^{o}C and 570^{o}C are selected which are below the eutectic temperature of 573^{o}C. Fig. 4.16a and 4.16b depicts the relationship between the compaction temperature and relative density as well as compaction temperature and microhardness of Al-4Si-0.6Mg alloy. Compaction temperature corresponding to 550^{o}C offered the maximum density of 93.5% and hardness of 43 HV. Microstructural studies on the sintered specimens are shown in Fig. 4.17. Specimens sintered at lower temperatures had coarse Mg_2Si precipitates

(faded appearance) as seen from Fig. 4.17a and b whereas as the temperature nears the eutectic limit Mg_2Si precipitates are finely distributed throughout the specimen.

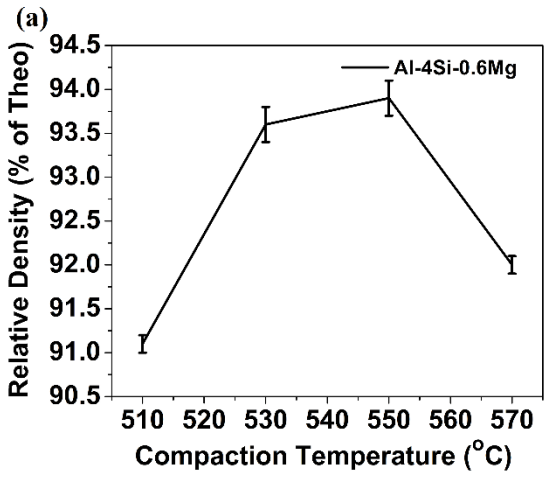

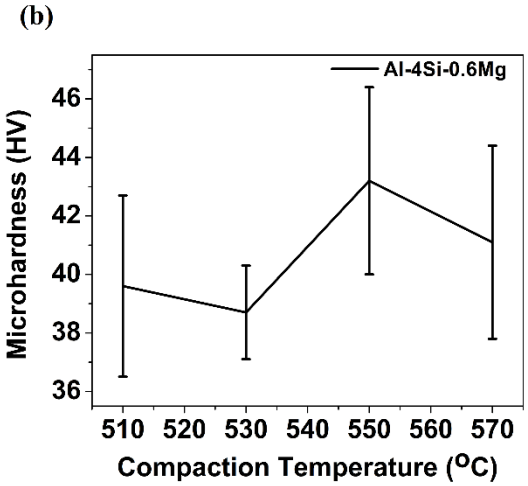

Fig. 4.16a) Compaction temperature vs Relative density

b) Compaction temperature vs Microhardness

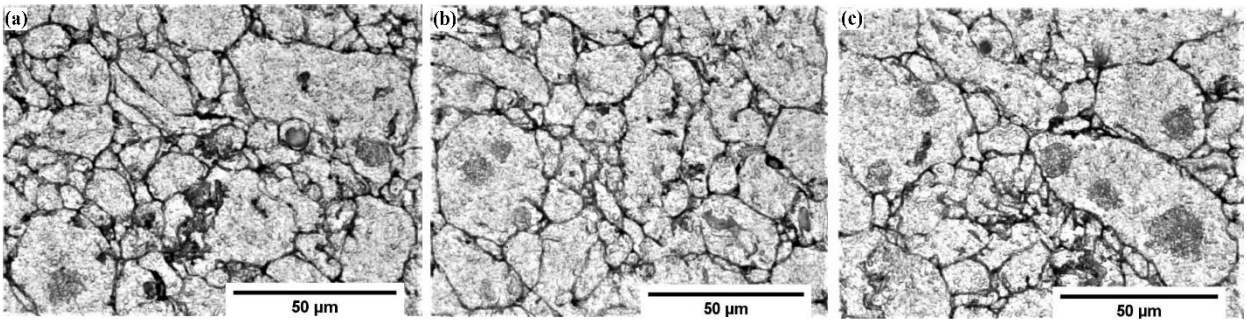

Fig. 4.17 Micrographs for Al-4Si-0.6Mg alloy sintered at **a)** 530°C **b)** 550°C **c)** 570°C

4.3.5 Holding Time Studies

Holding time studies were done for different times of 20 mins, 40 mins, 60 mins and 80 mins at a constant sintering temperature of 550^{o}C. Fig. 4.18a and 18b show the relative density vs holding time profile and microhardness vs sintering time profile of Al-4Si-0.6Mg alloy. Holding time corresponding to 60 mins gave a high density of 93.5% and hardness value of 44HV. Moreover coarsening of grains were observed at higher temperatures. Hence, 60 mins was finalized as the optimum holding time.

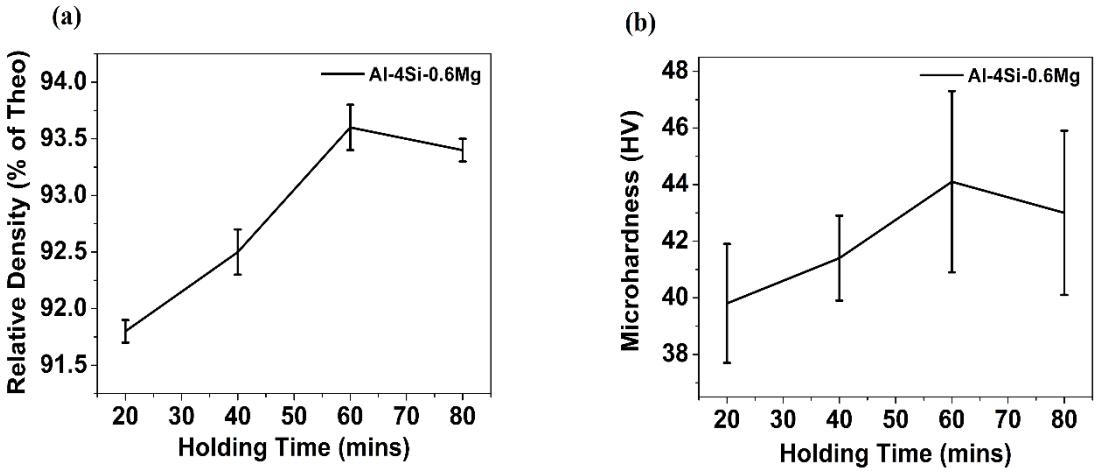

Fig. 4.18a) Holding time vs Relative density **b)** Holding time vs Microhardness

4.3.6 Semisolid Extrusion of Al-Si-Mg

Semisolid extrusion was done for three different temperatures namely 565^{o}C, 585^{o}C, and 605^{o}C respectively. The temperatures were selected so that they fall within the semisolid range of the alloy. Generally thixoextrusion should be carried out between liquid fractions of 0.3%-0.5%. Hot compacts extruded at 605^{o}C have an approximate length of 40-50 mm, while 585^{o}C fall within the length range of 30-40 mm and the specimens extruded at 565^{o}C have much smaller length. The decrease in length is because of the decreased liquid fraction present in the material at that extrusion temperatures. Specimens extruded at 565^{o}C are heavily deformed as seen from the Fig. 4.19 which implies that the material has offered much resistance to the deformation. This is because of the addition of Mg which has increased the strength of the alloy which was not the case with Al-4Si alloy.

The solid fraction present in the specimen was calculated by using Scheil equation as mentioned above in the previous section. Solid fraction corresponds to 565^{o}C, 585^{o}C, and 605^{o}C are 99%, 75%, and 47% respectively. Microstructural studies on the transverse section of the specimens were done. Fig. 4.19 shows the OM images of the front, middle and the rear ends of the specimen extruded at 565^{o}C. The front, middle and rear ends all had a fine near globular microstructure as seen from Fig. 4.19. This is because of insufficient liquid available in the material as evident from the Fig. 4.19 and the heavy deformation process that reduces the size of the grains as compared with the compacted specimens.

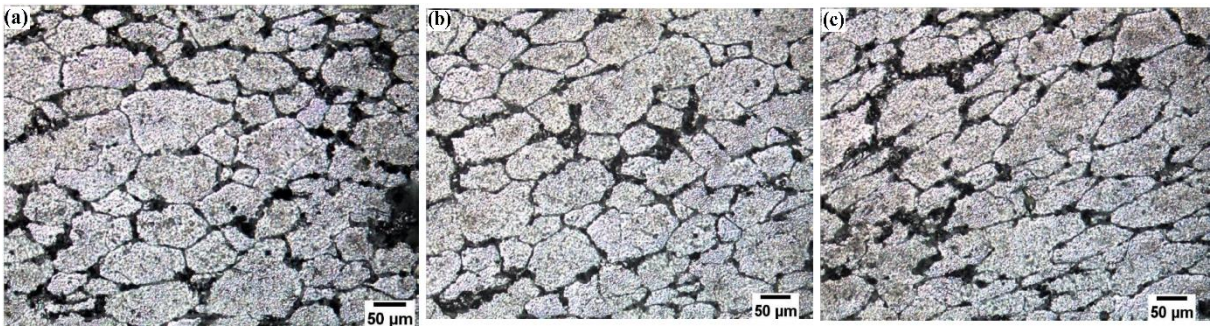

Fig. 4.19 Optical Micrographs along the transverse direction of specimen extruded at 565^{o}C and strain rate 0.2 s^{-1} **a)** front end **b)** middle part and **c)** rear end

Fig. 4.20 shows the OM images of the front end, middle and the rear end of the specimen extruded at 585^{o}C. As the extrusion temperature is well above the eutectic temperature of the alloy and the liquid content in the specimen has also increased, a globular microstructure has been achieved at 585^{o}C. Dynamic recrystallization is the reason attributed to the globular microstructure because of the specimen being subjected to temperature above the eutectic as well as the extrusion process with the ratio of 4:1. The slow cooling rate associated with the process and the continuous dissolution of Mg has led to the increased grain size as compared with 565^{o}C specimens.

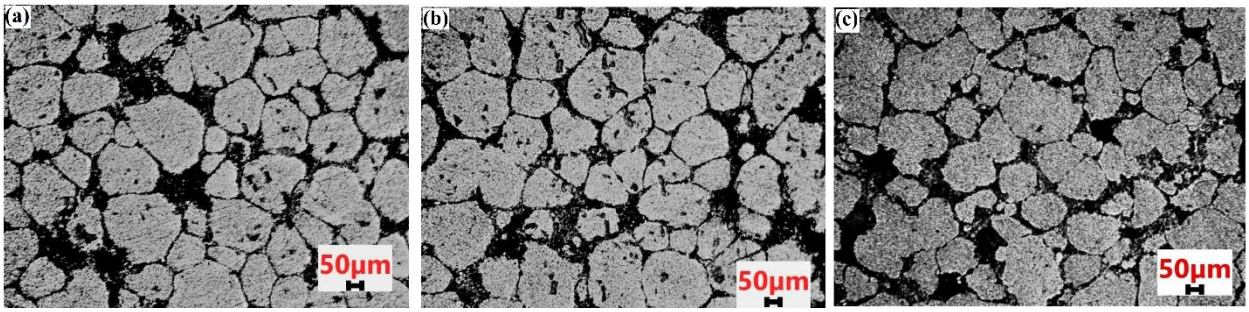

Fig. 4.20 Optical Micrographs along the transverse direction of specimen extruded at 585^{o}C and strain rate 0.2 s^{-1} for **a)** front end **b)** middle part and **c)** rear end

The increase in the size of the α-Al phase results from the increased dissolution of magnesium from the Mg_2Si phase at elevated temperature. Thus, the amount of magnesium left for the crystallization of Mg_2Si phase decreases drastically. Fig. 4.21a and b show the SEM images of the extruded specimen at 605°C and the EDS results. EDS analysis confirm the presence of Si and Mg particles along the grain boundaries. The coarse network shaped Mg_2Si has been converted into more coral reef like microstructure with fine spheroidal shaped Mg_2Si particles. Eutectic silicon flakes grows along 111 crystallographic directions as it is the preferred direction of solidification. Moreover, eutectic silicon acts as the substrate for the crystallization of Mg_2Si phase and hence these particles are concentrated along the grain boundaries. Also, at 585°C and 605°C the silicon particles have transformed from needle morphology to fine spherical morphology as evident from the SEM image.

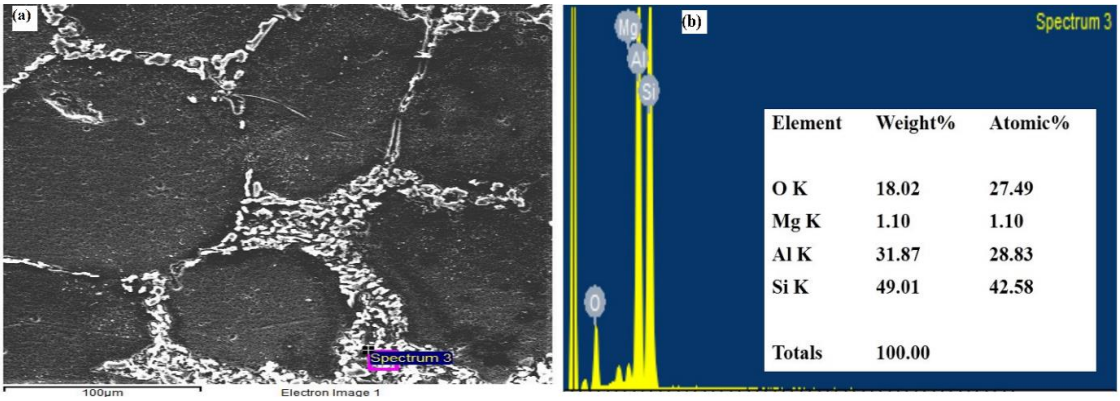

Fig. 4.21a) SEM image ofAl-4Si-0.6Mg alloy **b)** EDS result corresponding to fig 4.21 a Extruded at 585°C and and strain rate of 0.2 s^{-1}

.

4.4. Al-Si alloy vs Al-Si-Mg alloy

Fig. 4.22a and b show the variation of relative density and the microhardness of the full specimen with respect to extrusion temperature. From Fig. 4.22 a, it is concluded that for all the temperatures Al-4Si alloy offered high density compared with Al-4Si-0.6Mg. Among the Al-4Si alloy, the samples extruded at 585^{o}C provided the highest density (94.5%) followed by 565^{o}C. This is because of the presence of high solid content in the specimen which along with extrusion caused an increase in the density of the specimen to make it denser. On the other hand, samples extruded at 600^{o}C had maintained the relative density of 93% which was the initial compaction density. But in case of Al-4Si-0.6Mg alloys the highest density (90%) was given by extrudate at 565^{o}C in which the specimen was well below the eutectic temperature (573^{o}C) and the other extrudates of 585^{o}C and 605^{o}C offering reduced density as expected.

Fig 4.22 b shows the variation of microhardness of the full specimen with respect to extrusion temperature. As far as microhardness is concerned, Al-4Si-0.6Mg alloy had 30% higher hardness than Al-4Si alloy. The hardness variation between different extrusion temperatures for the same alloys was less significant. But between the alloys (Al-4Si-0.6Mg and Al-4Si) there was a considerable change.

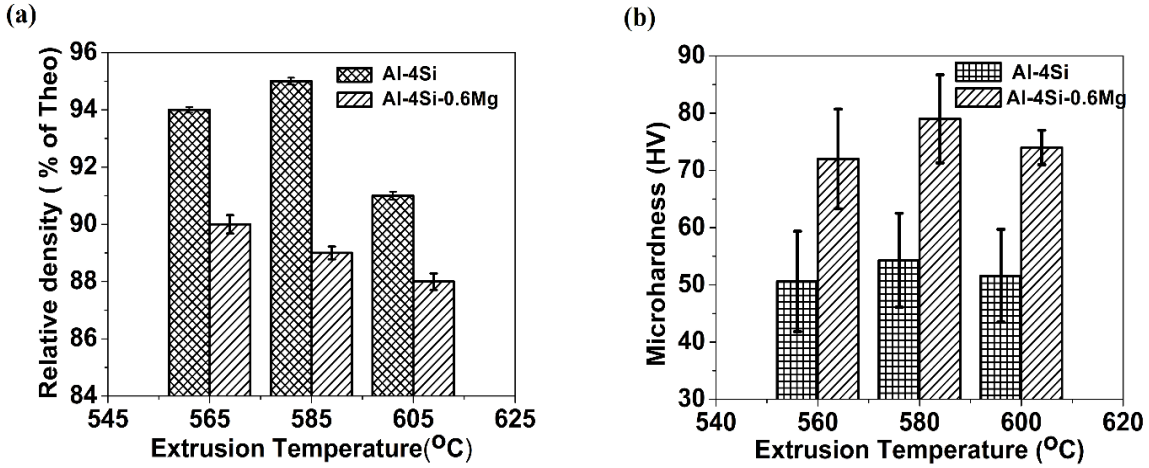

Fig. 4.22a) Relative density as a function of Extrusion temperature **b)** Microhardness as a function of Extrusion temperature

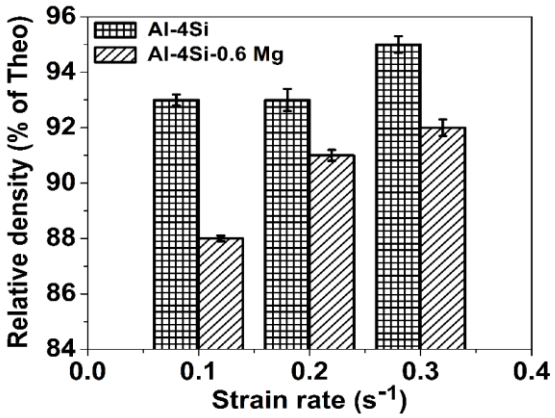

Fig. 4.23: Relative density as a function of strain rate

Fig. 4.23 shows the function of relative density with respect to the applied strain rate on the specimen. The general trend observed is, higher the strain rate higher the relative density especially at strain rate of 0.3 s^{-1}. High strain rate offers least time for the specimens to react thus consolidating the density of the material.

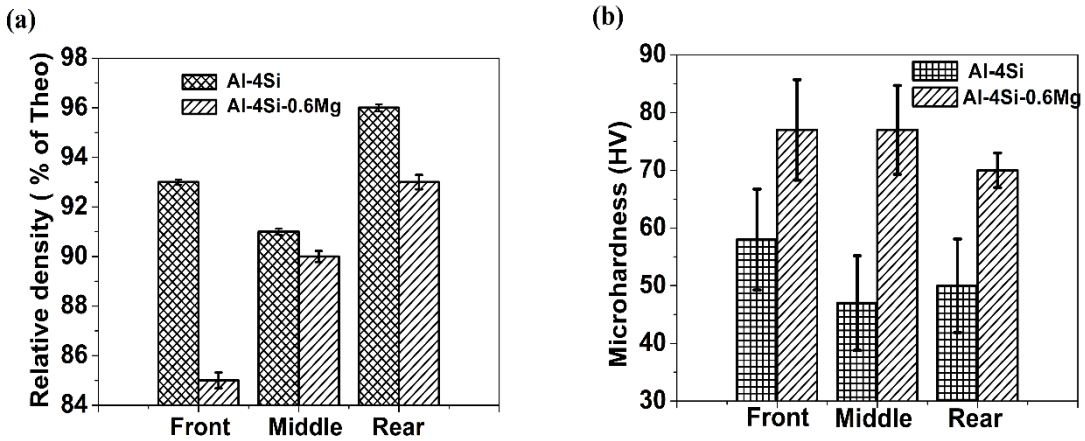

Fig. 4.24a) Relative density as a function of different regions **b)** Microhardness as a function of different regions

Fig. 4.24a shows the function of relative density with respect to different regions in the specimen for Al-4Si alloy and Al-4Si-0.6Mg alloy. Among the different sections, the rear parts had the highest density of 96% for Al-4Si alloy and 93% for Al-4Si-0.6Mg alloy. This was followed by the middle and the front sections. This could be due to the rear end being subjected to high stresses in contrast with the middle and front regions.

Fig. 4.24b shows the function of microhardness with respect to different regions in the specimen for Al-4Si alloy and Al-4Si-0.6Mg alloy. As discussed earlier, cutting across the regions, Al-4Si-0.6Mg alloy showed a marked increase in hardness values over the Al-4Si alloy. This was because of the front and middle regions being at temperatures higher than the rear end which could have led to the increased diffusion of Si in case of Al-4Si alloy and Mg in case of Al-4Si-0.6Mg alloy into the α-Al phase thus increasing the hardness of the specimens.

4.5 Grain Size Analysis

The variation in grain sizes of Al-4Si alloy and Al-4Si-0.6Mg alloy are shown in Table 4.1. The average grain size of raw aluminium powder was 44 µm. Sintered Al-4Si alloy had a reduced grain size of 22 µm whereas Al-4Si-0.6Mg alloy had a slightly coarse grain because of the addition of Mg. Al-4Si alloys extruded at 560^{o}C, 580^{o}C, 600^{o}C had average grain sizes of 30 µm, 81 µm and 90 µm respectively. On the other hand, Al-4Si-0.6Mg alloys had the corresponding grain sizes of 109 µm, 181 µm and 197 µm. Clearly, the addition of Mg had caused a 263%, 123%, 118% corresponding increase in the grain size of Al-4Si-0.6Mg alloy. This was because of pure Mg diffusing into α-Al matrix until it reaches the solubility limit as well as the eutectic melting of Al and Mg_2Si in which Mg_2Si precipitates dissolve into the liquid phase. The remaining Mg_2Si precipitates offer a weak resistance to the grain boundary migration. Thus, allowing further coarsening of α-Al grains. Similarly front middle and rear sections of Al-4Si-0.6Mg alloys show an increase of 192%, 153%, and 143% over their Al-4Si

counterparts. This was largely due to increased availability of liquid content present at the front end of the specimen than the other ends leading to coarser α-Al grains.

Grain Size	Al-4Si alloy	Al-4Si-0.6Mg alloy	% increase
Sintered specimen	22±12μm	48±22μm	118
Extruded specimens			
560 °C	30±10μm	109±36μm	263
580 °C	81±15μm	181±32μm	123
600 °C	90±12μm	197±12μm	118
Section			
Front	56±12μm	164±37μm	192
Middle	65±13μm	165±33μm	153
Rear	44±12μm	107±24μm	143

Table 4.1: Comparison chart showing grain size variation of Al-4Si alloy and Al-4Si-0.6Mg alloy

4.6 Chapter summary

Hot compaction and hot extrusion was carried out for different compositions of Al-Si and Al-Si-Mg alloys. Specimens produced were defect free with high densities and better hardness indicating an increased mechanical properties. Eutectic temperature was found to be the most suitable operating temperature with better die filling capacity and improved properties. Similarly top middle and rear end of the specimens showed varying grain sizes for both Al-Si and Al-Si-Mg alloys.

Chapter-5

Microstructure Modelling of sintered Al-4Si-0.6Mg alloy extruded at semisolid temperature ranges

5.1 Introduction

Microstructure evolution of sintered and extruded samples of Al-4Si-0.6Mg powder alloys at various semi solid temperature ranges of 560^0C, 580 ^{0} C and 600 ^{0} C, holding times such as 600 s,1200 s, and 1800 s and at various strain rates of 0.1 s^{-1}, 0.2s^{-1} and 0.3 s^{-1} were studied. From the stress-strain curves and metallographic studies, Arrhenius grain growth model and Avrami dynamic recrystallization model have been formulated by means of linear regression. Parameters such as peak strain, critical strain, recrystallization fraction and material constants have been found using the above equations. The experimental and calculated values of the various material parameters agree with each other indicating the accuracy of the developed model. Finite element method based simulations were performed using DEFORM 2D software and the average grain size obtained from experiments and simulations were validated by means of average grain size.

5.2. Microstructure modeling

5.2.1 Grain growth model

Fig. 5.1 shows the optical microscopy (OM) images of Al-4Si-0.6Mg alloy at 560^0C with different holding times namely 600 s, 1200 s and 1800 s respectively. From the figure, it is found that the average grain size increases with the increase in holding time. The average grain size of Al-4Si-0.6Mg alloy for different holding times such as 600 s, 1200 s and 1800 s are 56 µm, 61µm, and 70 µm respectively.

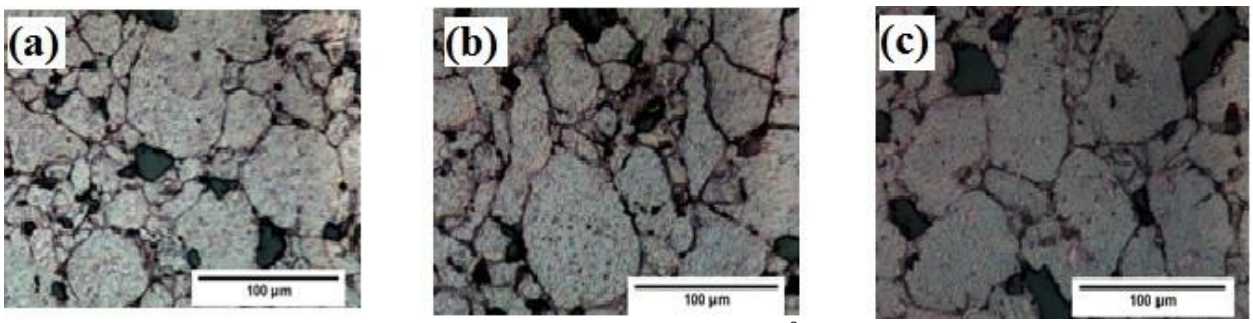

Fig. 5.1: Optical micrographs of Al-4Si-0.6Mg alloy for 560 ^{0}C heating temperature with holding times of **a)** 600 s; **b)** 1200 s; **c)** 1800 s

Fig. 5.2 illustrates the OM images of water quenched samples of Al-4Si-0.6Mg alloy at different heating temperatures namely 560^0C, 580^0C, and 600^0C and at constant holding time of 1200 s. It is found that with increasing heating temperature, the average grain size has increased. The average grain size of Al-4Si-0.6Mg alloy for different heating temperature such as 560^0C, 580^0C, and 600^0C are 56 µm, 350 µm and 420 µm respectively.

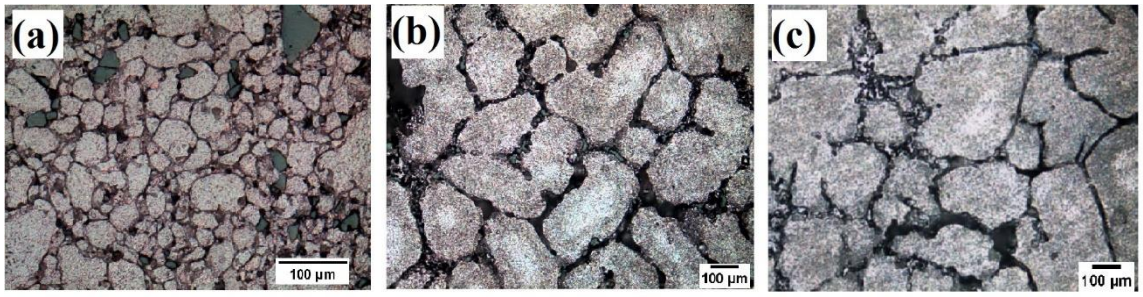

Fig. 5.2: Optical micrographs of Al-4Si-0.6Mg alloy for different heating temperatures of **a)** 560 ^{0}C; **b)** 580 ^{0}C; **c)** 600 ^{0}C with holding times of 1200 s

The grain growth model of Al-4Si-0.6Mg alloy during heating process has been formulated using an Arrhenius type empirical equation [180]as stated below.

$$d^n = d_0^n + Ate^{\frac{-Q}{RT}} \text{ ---------- (5.1)}$$

Where, d (µm) is the final grain size after heat treatment, d_0(µm) is the initial grain size (45 µm) before heat treatment, t is the holding time denoted by s, Q is the activation energy for grain growth denoted by J/mol and R is the universal gas constant given by 8.314 J/mol/K. Specific heating temperature in Kelvin is denoted by T(K) and A and n are the materials constants. Relationship between average grain size, temperature and holding time can be expressed as

$$d^n \alpha Ate^{\frac{-Q}{RT}} \text{---------- (5.2)}$$

The materials constants n and Q are obtained from the slope of the line in ln(t) vs ln(d) plot and (-1000/nRT) vs ln(d) plot, respectively. Fig. 5.3 (a) demonstrates the relationship between holding time and grain size under different heating temperatures. Fig. 5.3 (b) illustrates the relationship between -1000/nRTand ln (d) under different holding times.

At 560°C the microstructure consists of primary Aluminium, primary silicon and primary magnesium. Whereas above 573 °C (eutectic temperature) the microstructure consists of primary aluminium ,eutectic Mg_2Si which is distributed at the grain boundaries as seen from Fig. 5.2 and primary silicon[178]. At the same time, increasing holding time beyond 1800 s may lead to the increase of liquid content rapidly with specimen collapsing and swelling defects. Further, it can be concluded that deformation temperature has much larger effect than holding time on average grain size.

The constitutive equation for grain growth model of Al-4Si-0.6Mg alloy can be formulated as shown in equations (5.3)-(5.5). To ascertain the accuracy of the model, the relative error (δ_r) between the calculated grain size (d_c) and the experimental grain size (d_e) was found using the relation 5.6.

$$d^{5.3705} = d_0^{5.3705} + 5.31e6 * t * e^{\frac{-1578.941}{RT}} \text{---------- (5.3) (560 } ^0\text{C)}$$

$$d^{5.173} = d_0^{5.173} + 2.07e6 * t * e^{\frac{-1578.941}{RT}} \text{---------- (5.4) (580}^0\text{C)}$$

$$d^{4.916} = d_0^{4.916} + 1.029e6 * t * e^{\frac{-1578.941}{RT}} \text{---------- (5.5) (600}^0\text{C)}$$

$$\delta_r = \frac{d_c - d_e}{d_e} * 100 \text{ ---------- (5.6)}$$

Table 5.1 shows the information about the variation between the calculated and experimental grain sizes. It is thus clear from the table that the calculated grain size agree with the experimental ones. The mean relative error between the calculated and experimental grain size at deformation temperature of 560 ^{0}C, 580 ^{0}C, and 600 ^{0}C being less than 10% respectively

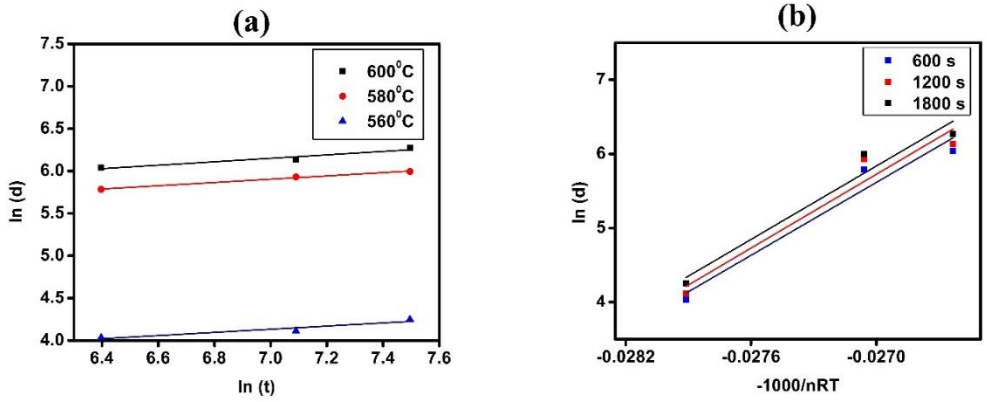

Fig. 5.3: **a)** Relationship between holding time and average grain size for various heating temperatures; **b)** Relationship between -1000/nRT and ln (d) under different holding times

Table 5.1: Comparison between experimental and calculated grain sizes forAl-4Si-0.6Mg alloy

S.No	Time (t) s	Temperature (T) ^{0}C	Grain size		Error %
			Experimental d_e µm	Calculated d_c µm	
1	600	560	56.512	57.959	2.560
2	1200	560	61.131	65.082	6.463
3	1800	560	70.210	69.864	-0.492
4	600	580	325.546	325.501	-0.013
5	1200	580	376.121	372.173	-1.049
6	1800	580	401.576	402.517	0.234
7	600	600	420.231	382.386	-9.005
8	1200	600	461.177	440.284	-4.530
9	1800	600	530.687	478.136	-9.902

5.2.2 Flow stress behavior

Fig. 5.4 shows the true stress–true strain plots for Al-4Si-0.6Mg alloys under different deformation temperatures and at different strain rates namely (a) 0.1 s^{-1}; (b) 0.2 s^{-1}; and (c) 0.3 s^{-1}. It can be observed from Fig. 5.4 that with the increase in the strain, the flow stress increased at the initial stage and then it decreased with deformation. This was due to thermal softening

mechanism which decreased the flow stress values. At higher temperatures, with the further accumulation of the materials strain, the dynamic recrystallization phenomena occur resulting in the decrease of the flow stress. This may be due to vacancy diffusion, slip and subsequent increase in climb mechanisms. Thus, recovery phenomenon supersedes the hardening. It is seen that the flow stress increased with increasing strain rate and decreasing temperature. Flow curves display a peak which is then followed by a gradual decline to a steady state stress which signals the happening of DRX[181]

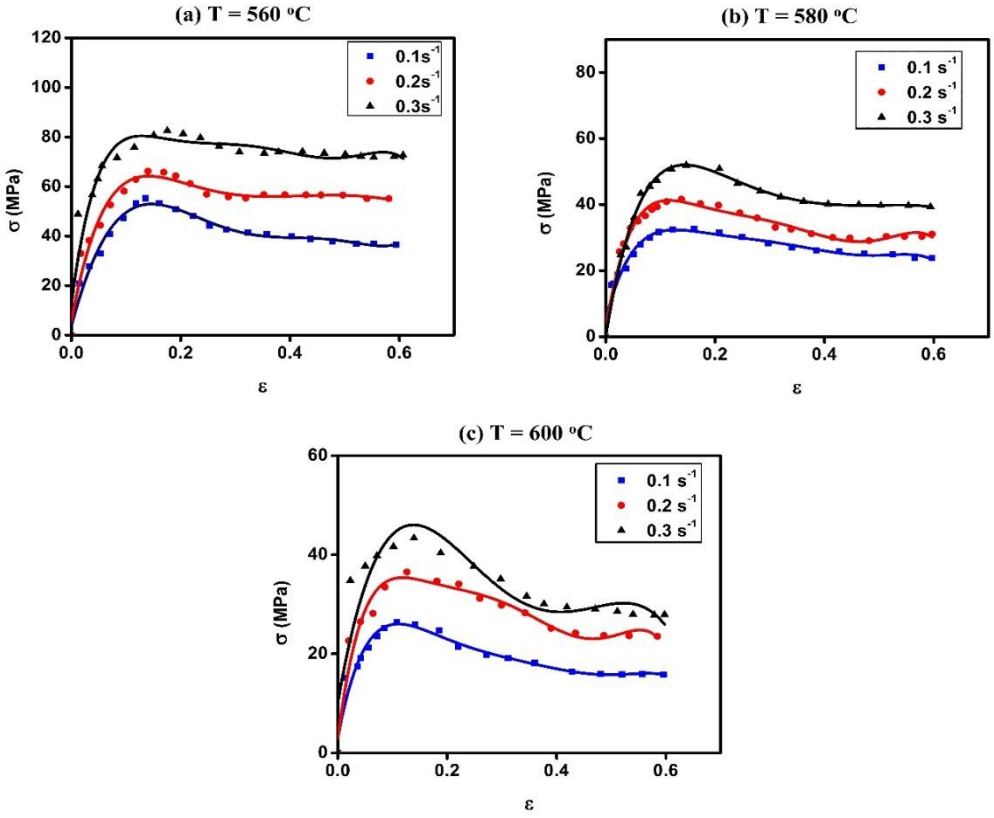

Fig. 5.4: True stress-True strain curves for Al-4Si-0.6Mg alloy under different temperatures of **a)** 560 ^{0}C; **b)** 580 ^{0}C; **c)** 600 ^{0}C

5.2.3. Dynamic recrystallization

Dynamic recrystallization cannot begin until the energy level crosses a threshold value. The threshold value can be denoted by critical strain ε_c, which has been found to be slightly less than the peak strain ε_p[182] (strain at which the stress reaches peak).The mechanism behind the evolution of microstructure is geometric dynamic recrystallisation as observed by Donati et al [183]. Dynamic recrystallization behavior of Al-Si-Mg alloys has been modeled using Johnson Mehl Avrami Kolgrov model (JMAK) as follows

$$\varepsilon_c = a_1 \varepsilon_p \text{----------} (5.7)$$

5.2.4 Prediction of critical stress for DRX initiation

The beginning of DRX process depends on the material's chemical composition and the hot deformation parameters. The DRX phenomenon occurs more easily at higher deformation temperature because it reduces the driving force of the mechanism. Whereas, low strain rate promotes DRX as enough time will be available for accumulation of energy.

In order to find the critical strain, it is necessary to plot the graph between true stress and hardening rate. The inflection point present in the Θ–σ curve indicates the occurrence of DRX. In this study, the method followed by Najafizadeh and Mirzadeh[181]was utilized for finding the critical stress which initiates the DRX phenomenon. The inflection point was found by fitting a third order polynomial equation to the hardening rate vs true stress curves up to the peak point as follows.

Third order polynomial equation corresponding to the plot of true stress vs hardening rate for 560^0C and 0.1 s^{-1} is

$$y = -0.0696x^3 + 9.2038x^2 - 407x + 6544.3 \text{ ----------} (5.8)$$

$$Critical\ stress\ \sigma c = -B/3\,A$$

$$= 9.2038/(3*0.0696)$$

$$= 44.079$$

This above method has been used to find the critical stress values of samples tested at different process conditions in this study. From the flow curves, the critical strain values were found. Fig. 5.5 shows the third order polynomial fit for true stress vs hardening rate plots for samples

tested at different temperatures. Hardening rate equations for the processed conditions are shown in Table 5.2.

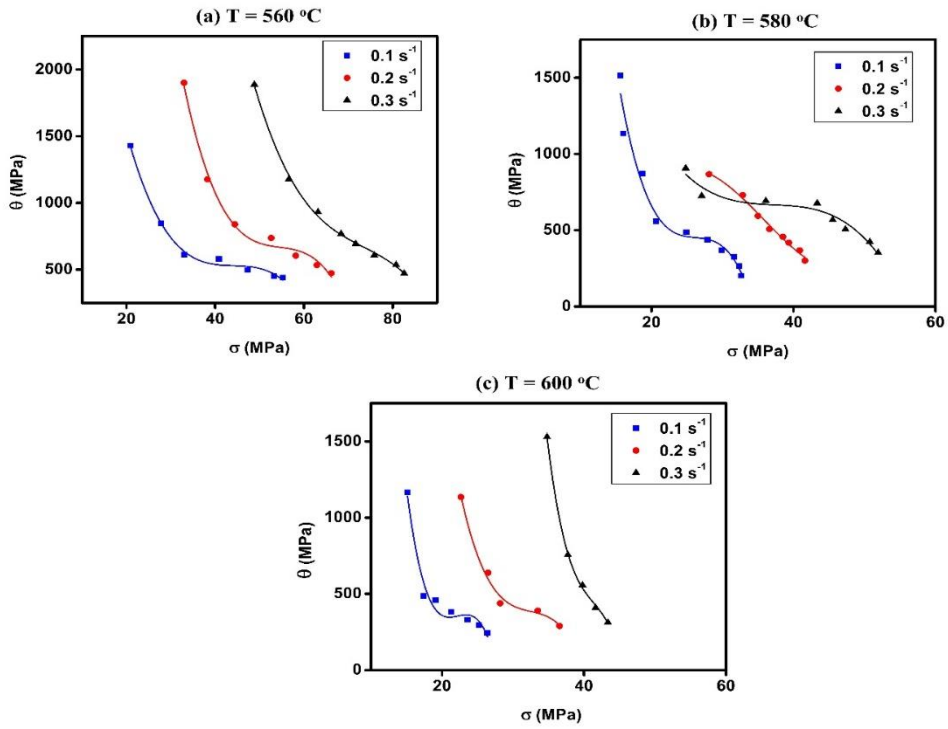

Fig. 5.5: Hardening rate –True stress curves for Al-4Si-0.6Mg alloy **a)** 560 ^{0}C; **b)** 580 ^{0}C; c**)** 600 ^{0}C

Strain rate s^{-1}	Temperature ^{0}C	Hardening rate equation
0.1	560	$\theta = -0.0696x^3 + 9.2038x^2 - 407x + 6544.3$
0.2	560	$\theta = -0.1104x^3 + 18.089x^2 - 992.07x + 18885$
0.3	560	$\theta = -0.0536x^3 + 11.807x^2 - 883.58x + 23116$
0.1	580	$\theta = -0.4709x^3 + 37.626x^2 - 1016.5x + 9726.7$
0.2	580	$\theta = 0.1502x^3 - 16.135x^2 + 530.02x - 4614.3$
0.3	580	$\theta = -0.0913x^3 + 10.19x^2 - 381.13x + 5445.3$
0.1	600	$\theta = -2.423x^3 + 161.46x^2 - 3576.5x + 26687$
0.2	600	$\theta = -0.6902x^3 + 67.246x^2 - 2194.7x + 24375$
0.3	600	$\theta = -2.5606x^3 + 317.59x^2 - 13187x + 183711$

Table 5.2: Hardening rate equations for Al-4Si-0.6Mg alloy at various conditions

S.No	Temperature ^0C	Strain rate s^{-1}	Peak strain	Critical strain
1	560	0.1	0.135	0.080
2	560	0.2	0.168	0.080
3	560	0.3	0.175	0.093
4	580	0.1	0.122	0.063
5	580	0.2	0.138	0.074
6	580	0.3	0.147	0.084
7	600	0.1	0.108	0.065
8	600	0.2	0.126	0.085
9	600	0.3	0.139	0.101

Table 5.3: Peak strain and critical strain for Al-4Si-0.6Mg alloy

The relation between peak strain and the process parameters is given by the relation

$$\varepsilon_p = a_2 {d_0}^{n_1} \dot{\varepsilon}^{m_1} exp(Q_1/RT) \text{ ---------- (5.9)}$$

Where, the initial grain size (45 µm) of the material is denoted by d_0 (µm); strain rate is denoted by έ (s^{-1}); the universal gas constant, is denoted by R (8.314 J/ mol/ K); deformation temperature, is denoted by T (K); while a_1, a_2, n_1, m_1 and Q_1 are the material constants, which can be obtained from the flow curves of the material. The material constants n_1, m_1 and Q_1 are found by plotting the relationship between $\ln(d_0)$ and $\ln(\varepsilon_p)$, $\ln(\dot{\varepsilon})$ and $\ln(\varepsilon_p)$, (1000/RT) and ($\ln\varepsilon_p - n_1 * \ln d_0$) as shown in Fig. 5.6 respectively. The constitutive peak strain equations for various temperatures are shown in Equations 5.10 -5.12. Table 5.4 gives the comparison between experimental and calculated peak strain values for compressed specimens.

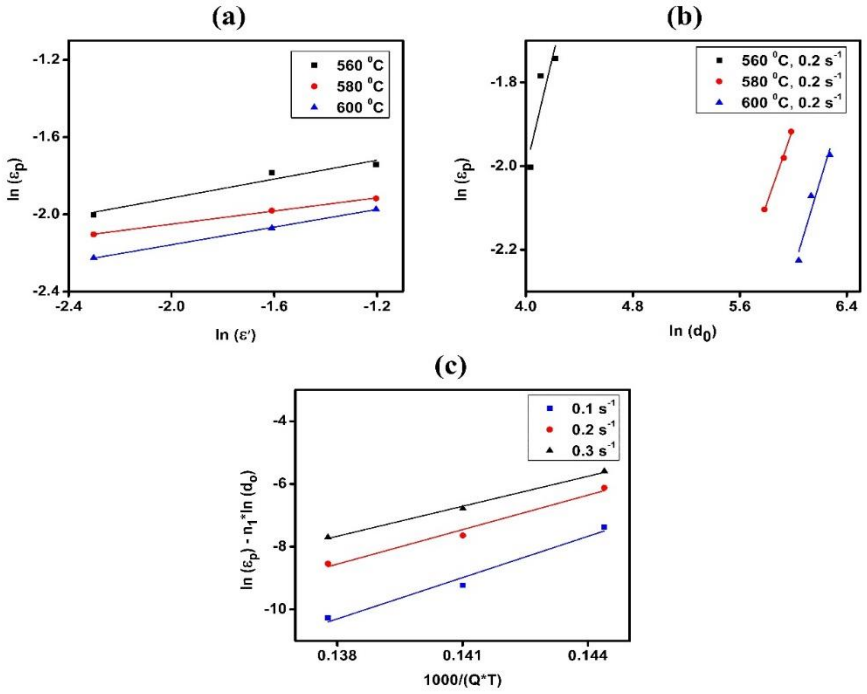

Fig. 5.6: Peak strain dependence on **a)** strain rate **b)** initial grain size and **c)** temperature

.

$$\varepsilon_p = 0.0009 {d_0}^{1.3322} \dot{\varepsilon}^{0.244} exp(399.4/RT) \text{ ---------- (5.10) (560 } ^0\text{C)}$$

$$\varepsilon_p = 0.0008 {d_0}^{0.913} \dot{\varepsilon}^{0.170} \exp(399.4/RT) \text{ ---------- (5.11) (580 } ^0\text{C)}$$

$$\varepsilon_p = 0.00026 {d_0}^{1.054} \dot{\varepsilon}^{0.226} exp(399.4/RT) \text{ ---------- (5.12) (600 } ^0\text{C)}$$

S.No	Temperature ^0C	Strain rate s^{-1}	Peak strain		Error %
			Experimental	Calculated	
1	560	0.1	0.135	0.117	-13.192
2	560	0.2	0.168	0.153	-8.337
3	560	0.3	0.175	0.196	12.219
4	580	0.1	0.122	0.112	-7.939
5	580	0.2	0.138	0.144	4.791
6	580	0.3	0.147	0.162	10.704
7	600	0.1	0.108	0.094	-12.118
8	600	0.2	0.126	0.122	-2.634
9	600	0.3	0.139	0.155	11.995

Table 5.4: Comparison between experimental and calculated peak strain for compressed samples

5.2.5 Model for 50% dynamic recrystallization strain

The DRX volume is usually measured by quantitative metallographic methods. Another method to measure DRX volume is from the stress strain curve of hot deformation test done at constant temperature and strain rate. The latter method is much simpler and faster than the former. As per the earlier researches [184], the dynamic recrystallization fraction can also be framed as follows

$$X_{drex} = \frac{\sigma_p - \sigma}{\sigma_p - \sigma_{ss}} \text{---------- (5.13)}$$

Where σ_p is the peak stress, σ is the instantaneous stress and σ_{ss} is the saturated stress. Saturated stress is found from the plot of Hardening rate vs True stress corresponding to the stress at which hardening rate is zero as shown in Fig. 5.7. Fig. 5.8 shows the true strain vs dynamic recrystallization fraction plot of Al-4Si-0.6Mg alloy. Using the above formula dynamic recrystallization fraction has been found. The strain corresponding to 50% dynamic recrystallization can be easily obtained from Fig 5.8. Table 5.5 shows the 50% recrystallized strain for Al-4Si-0.6Mg alloy.

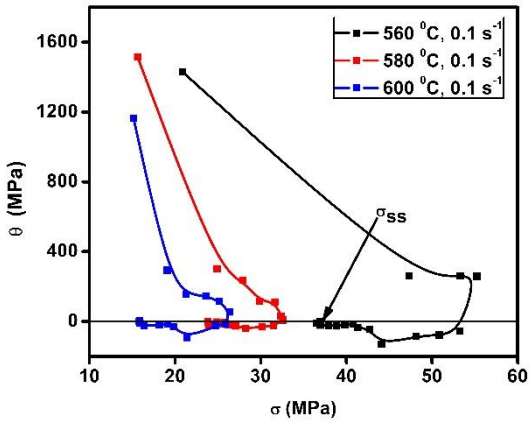

Fig. 5.7: Hardening rate vs True stress for Al-4Si-0.6Mg alloy under various temperatures

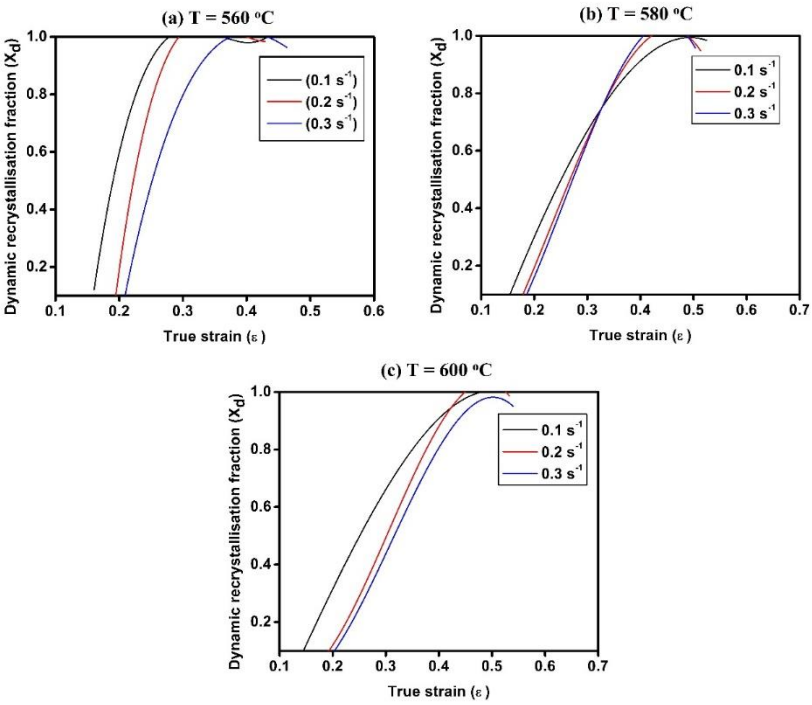

Fig. 5.8: Dynamic recrystallization fraction vs true strain for Al-4Si-0.6Mg alloy under various temperatures

S No	Temperature ^0C	Strain rate s^{-1}	50% recrystallized strain ($\varepsilon_{0.5}$)
1	560	0.1	0.250
2	560	0.2	0.299
3	560	0.3	0.325
4	580	0.1	0.240
5	580	0.2	0.270
6	580	0.3	0.280
7	600	0.1	0.190
8	600	0.2	0.217
9	600	0.3	0.253

Table 5.5:50% dynamic recrystallization strain for Al-4Si-0.6Mg alloy

The relationship between 50% recrystallized strain and the process parameters are expressed as functions of initial grain size (d_0), strain rate ($\acute{\varepsilon}$) and deformation temperature (T).

$$\varepsilon_{0.5} = a_3 {d_0}^{n_3} \acute{\varepsilon}^{m_3} exp(Q_3/RT) \text{---------- (5.14)}$$

Where, a_3, n_3, m_3 and Q_3 are material constants. The material constants n_3, m_3 and Q_3 are found by plotting the relationship between ln (d_0)and ln ($\varepsilon_{0.5}$), ln ($\acute{\varepsilon}$) and ln ($\varepsilon_{0.5}$), (1000/RT) and (ln $\varepsilon_{0.5}$-n_3*lnd_0) as shown in Fig. 5.9. The constitutive equations for 50% recrystallized strain are shown in equations 5.15- 5.17. Table 5.6 shows the comparison chart of experimental and calculated values.

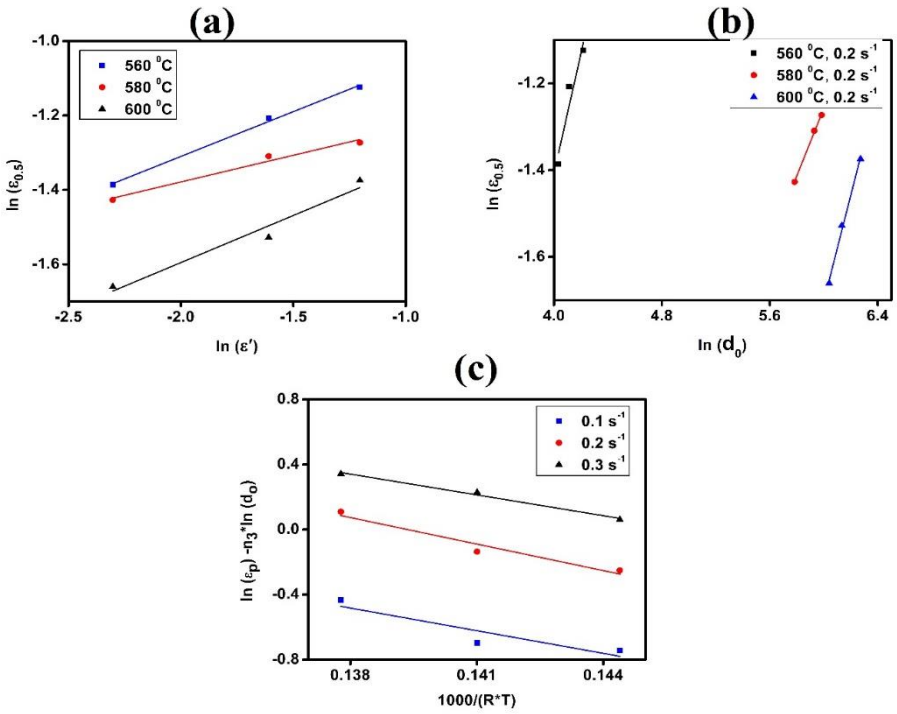

Fig. 5.9: Dependence of $\varepsilon_{0.5}$ on **a)** strain rate **b)** initial grain size and **c)** Temperature

$$\varepsilon_{0.5} = 0.0014 {d_0}^{1.378} \dot{\varepsilon}^{0.24} exp(-35.719/RT) \text{ ---------- (5.15) (560 } ^0\text{C)}$$

$$\varepsilon_{0.5} = 0.0035 {d_0}^{0.778} \dot{\varepsilon}^{0.143} exp(-35.719/RT) \text{---------- (5.16) (580 } ^0\text{C)}$$

$$\varepsilon_{0.5} = 0.00018 {d_0}^{1.22} \dot{\varepsilon}^{0.253} exp(-35.719/RT) \text{---------- (5.17) (600 } ^0\text{C)}$$

Table 5.6: Comparison between 50% dynamic recrystallization strain for experimental and calculated values for compressed samples

	Temperature ^0C	Strain rate s^{-1}	50% recrystallized strain ($\varepsilon_{0.5}$)		Error %
			Experimental	Calculated	
1	560	0.1	0.250	0.208	-16.771
2	560	0.2	0.299	0.273	-8.456
3	560	0.3	0.325	0.349	7.574
4	580	0.1	0.240	0.225	-6.046
5	580	0.2	0.270	0.278	3.290
6	580	0.3	0.280	0.308	10.105
7	600	0.1	0.190	0.158	-16.488
8	600	0.2	0.217	0.211	-2.377
9	600	0.3	0.253	0.278	9.987

Equation 5.18 was used to model the relationship between the dynamically recrystallized grain sizes of the alloy. Using the physical experiments, the material constants were found by plotting the graphs between ln (έ)and ln (d_{rex}), ln (d_0) and ln (d_{rex}), (1000/RT) and ($lnd_{rex} – h_4 * lnd_0$), ln (ε) and ln (d_{rex}). Fig 5.10 shows the relationship between the dynamically recrystallized grain size and the material parameters. The relationship between dynamically recrystallized grain size and the process parameters are

$$d_{rex=}a_4 {d_0}^{h_4} \varepsilon^{n_4} \dot{\varepsilon}^{m_4} exp(Q_4/RT)$$ ---------- (5.18)

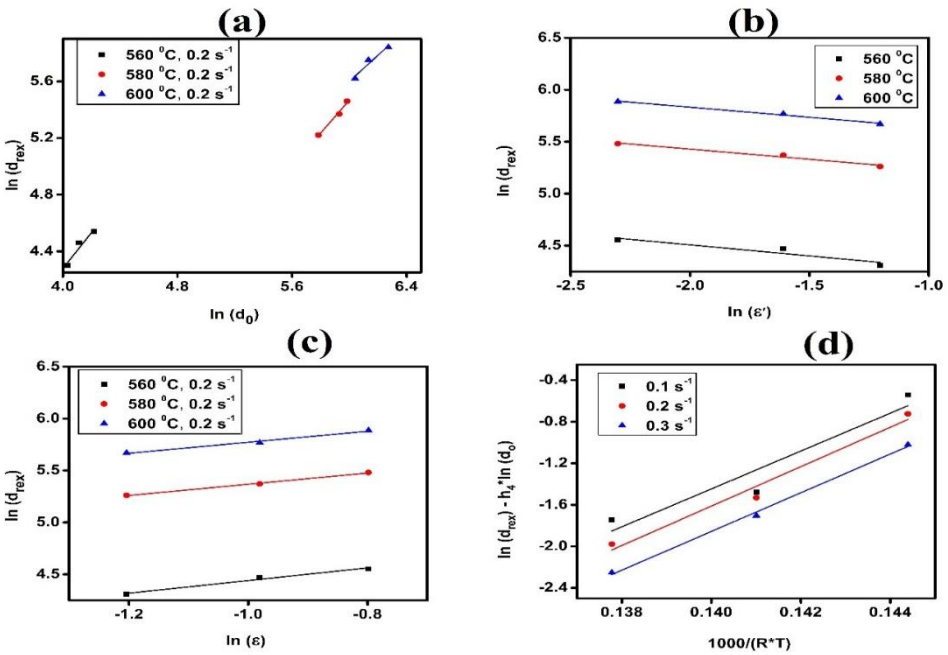

Fig. 5.10: Relationship between dynamically recrystallized grain size and a) initial grain size b) strain rate c) strain d) temperature

$$d_{rex} = 0.591 {d_0}^{1.263} \varepsilon^{0.6} \dot{\varepsilon}^{-0.212_4} exp(141.66/RT)$$---------- (19) (560 ^{0}C)

$$d_{rex} = 0.279 {d_0}^{1.164} \varepsilon^{n_4 0.54} \dot{\varepsilon}^{-0.195} exp(141.66/RT)$$---------- (20) (580 ^{0}C)

$$d_{rex} = 1.366 {d_0}^{0.922} \varepsilon^{0.52} \dot{\varepsilon}^{-0.193} exp(141.66/RT)$$---------- (21) (600 ^{0}C)

S.No	Temperature ^0C	Strain rate s^{-1}	Dynamic recrystallized grain size		Error %
			Experimental µm	Calculated µm	
1	560	0.1	95.232	99.365	4.595
2	560	0.2	87.330	84.8871	-2.797
3	560	0.3	74.332	77.992	4.927
4	580	0.1	240.350	243.404	1.418
5	580	0.2	215.245	228.326	6.198
6	580	0.3	192.663	199.232	3.411
7	600	0.1	360.221	376.130	4.480
8	600	0.2	320.075	326.108	1.908
9	600	0.3	290.226	305.374	5.301

Table 5.7: Comparison between experimental and calculated grain size after dynamic recrystallization for extrusion test

5.2.6 Model for dynamic recrystallization volume fraction

DRX process can be expressed in a sigmoidal fashion with respect to strain as shown in the above literatures[158], [180]. An Avrami type equation shown as follows was utilized to describe the relationship between the DRX fraction X_{drex} and the effective strain ε.

$$X_{drex} = 1 - exp[-\beta_d(\varepsilon - \varepsilon_c/\varepsilon_{0.5})^{k_d}] \text{---------- (5.22)}$$

Where $\varepsilon_{0.5}$is the strain of 50% dynamic recrystallization, K_d and β_d are the recrystallization parameters depending on the material considered and the processing conditions. From equation 22, K_d and β_d can be found. From Fig. 5.11, it can be seen that there exists a linear relationship between $\ln(-\ln(1-X_d))$ and $\ln(\varepsilon-\varepsilon_c/\varepsilon_{0.5})$ under different processing conditions.

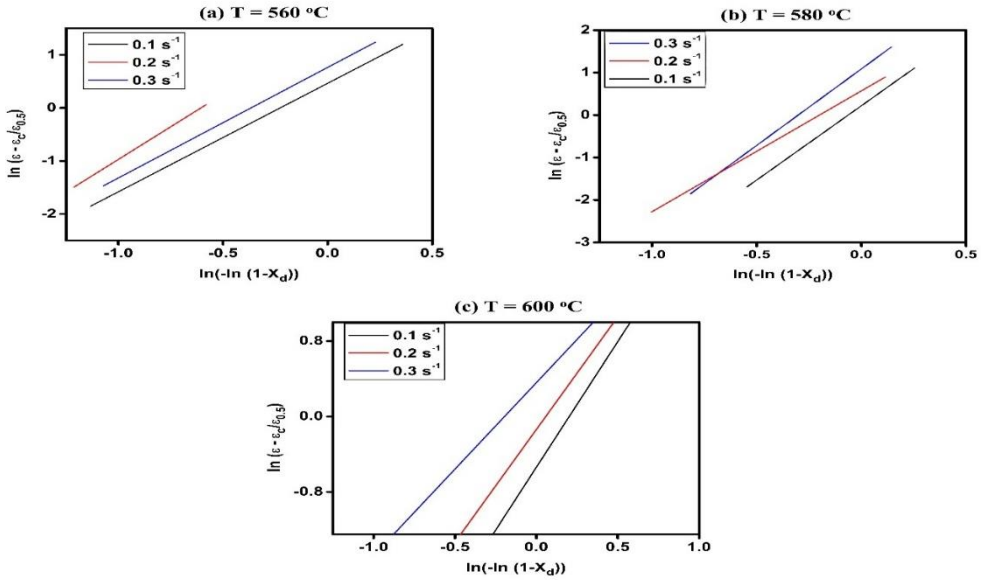

.

Fig. 5.11: Relationship between $\ln(-\ln(1-X_d))$ and $\ln(\varepsilon-\varepsilon_c/\varepsilon_{0.5})$ under different processing conditions.

5.3 Finite Element Simulation

The microstructural modeling of Al-4Si-0.6Mg alloy during hot extrusion process was done using coupled thermo-mechanical finite element method in Deform 2D software. The availability of the above set of equations in the software make it suitable candidate for microstructure prediction. A shear friction factor of 0.3 was used between the tool interface and the billet. The die was modeled as rigid object. Due to the presence of symmetry of the specimens, only one half of the billet has been modeled.

5.3.1 Simulation Results

Fig. 5.12 shows the density plots of the compacted specimen and the extruded specimen. The model employed to calculate the density is Von Mises porosity model. From Fig. 5.12, it can be seen that the maximum density is at the top right corner of the specimen as maximum force and friction acts on it whereas the least density is found at the bottom right corner. This is a typical density profile of the uniaxial single acting compaction process. The maximum density and the minimum density values were found to be 99% and 83% with the average being around 91%. Experimentally measured density value of the same composition using Archimedes principle was found to be 93% which is well within the permissible limits. Similarly the average density of the extruded sample is found to be 95% from simulation results. However, the experimentally measured density was found to be 92%.

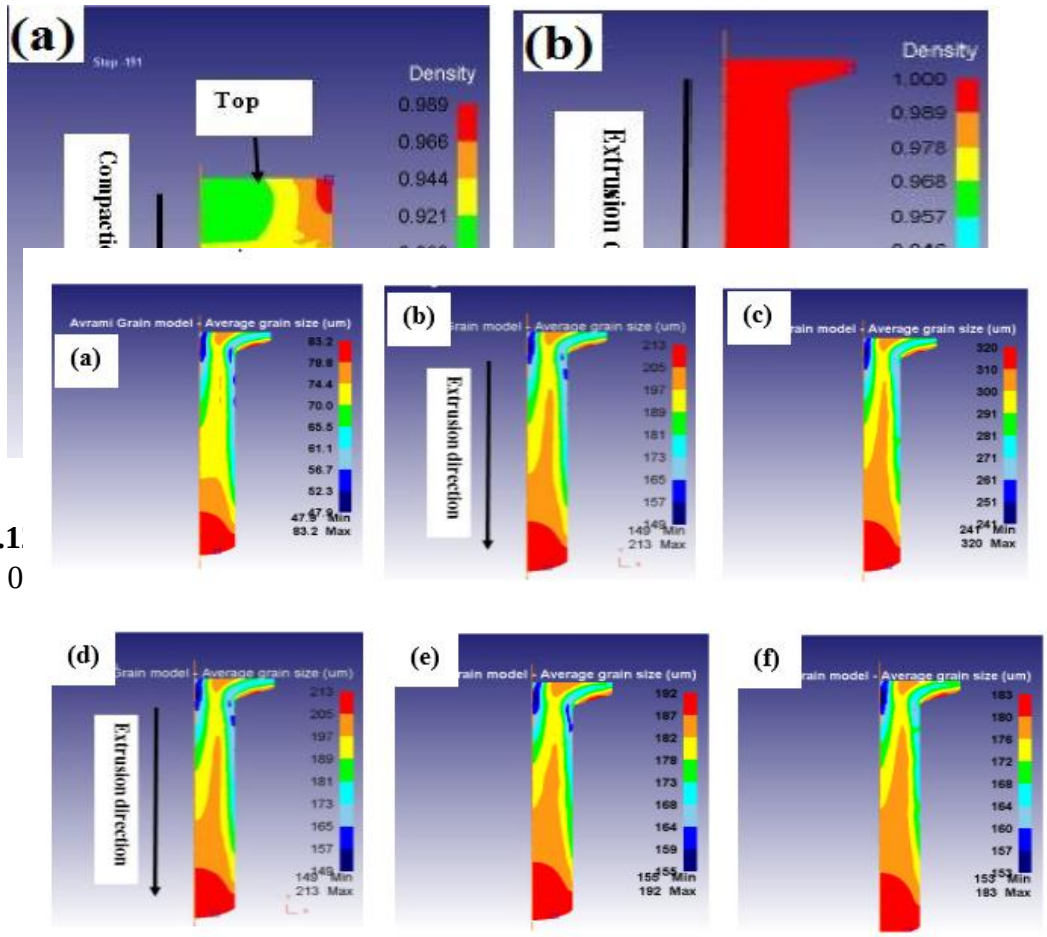

Fig. 5.1 30 ^{0}C and 0

Fig. 5.13: Average grain size plot of extruded Al-4Si-0.6Mg alloy along the longitudinal direction at constant $\varepsilon = 0.1s^{-1}$ for **a)**T =560 ^{0}C **b)** T = 580 ^{0}C **c)** T = 600 ^{0}C and at constant T = 580 ^{0}C for **d)** $\varepsilon = 0.1s^{-1}$ **e)** $\varepsilon = 0.2s^{-1}$ **f)** $\varepsilon = 0.3s^{-1}$

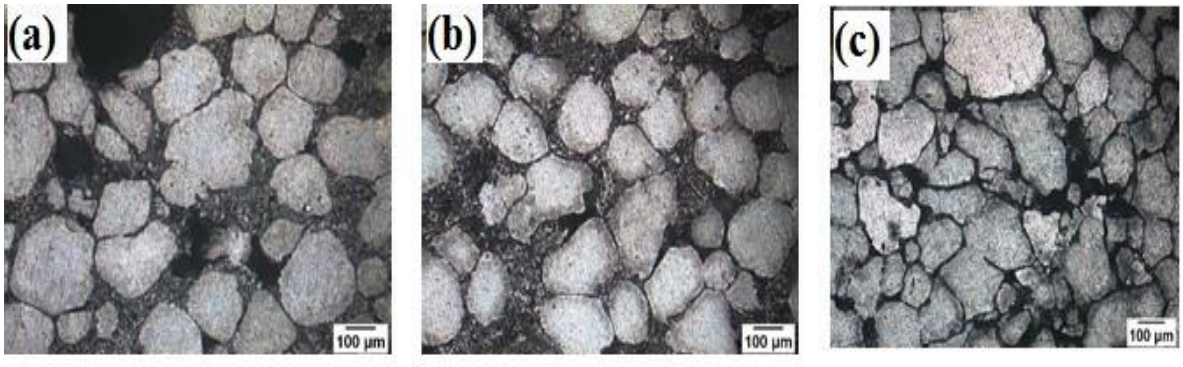

Fig. 5.14: Micrographs of extruded Al-4Si-0.6Mg alloy at **a)** Front end **b)** Middle section and **c)** Rear end

Fig. 5.13 shows the numerically simulated average grain size profile of Al-4Si-0.6Mg alloy for various temperatures and strain rate. The bottom part (in Fig 5.13 b) is found to have an average grain size of 213 µm, the middle part having 190 µm and the top part having180 µm. Significant differences are generally observed at higher strain rates and in the corners of the die where there is inhomogenity in the strain distribution[185]. Average grain size of the specimen increase with increasing temperature when other process parameters like strain rate and die angle were kept constant. High deformation temperature facilitates the formation of DRX grains more easily. This is because of higher kinetic energy induced during deformation[183]. Similarly Fig. 5.14 shows the microstructure images of the specimen extruded along the longitudinal section at three different sections namely front, middle and rear sections. The grain size is found to be 234 µm at the front end, 199 µm at middle section and 170 µm at rear end respectively

5.4 Chapter Summary

Grain growth modelling was carried out using Avrami grain model. Similarly dynamic recrystallization was modelled using JMAK model. Maximum error found was less than 20% in both the models. Recrystallization model included peak strain model critical strain model dynamically recrystallized grain size model, and 50% recrystallized grain model Recrystallization model was further validated with numerical results from deform software.

Chapter-6

Effect of various Mg/Si ratios on microstructure and structural properties of thixoextruded Al-Si-Mg alloys

6.1 Introduction

Al-Si-Mg alloy with different Mg/Si ratios of 0.75, 1, 1.5, and 2 have been extruded and the mechanical and metallurgical properties prior and after extrusion process have been evaluated. Differential thermal analysis was used to determine the solidus and liquidus point temperatures within the range of 560 °C to 580 °C. Extrusion was carried out for three different temperatures namely i) near solidus (t_s), ii) near eutectic (t_e), and iii) near liquidus temperatures (t_l) and three different strain rates ($0.1s^{-1}$, $0.2\ s^{-1}$ and $0.3\ s^{-1}$) respectively.

6.2 Optimization of Mg/Si

The mass composition of Mg/Si was varied for four different ratios of 0.75, 1, 1.5 and 2 respectively with other process parameters being constant. The mass percentage of silicon chosen is 4% (0.28 gms) with the Mg amount being varied as per the required ratio (0.21 gms, 0.28 gms, 0.42 gms and 0.56 gms) while the rest being aluminium. Fig. 6.1a and b shows the relative density plot and microhardness plot with respect to the weight ratios of Mg/Si. Maximum density achieved is about 98.2% for the ratio of 1. Beyond this ratio, there is drop in the relative density for higher ratios. This could be due to increased magnesium content which reduces the overall density. This kind of drop in density has been observed by authors like Yldrium [186]. The hardness plot is found to be more plateaued with peak hardness of 60 HV for R=1.5. The hard intermetallic phases (Mg_2Si) present in the matrix could be the reason behind increase in the structural properties of the compacts [187]. Excess Mg in the alloy would

not precipitate, because super saturated solution of Mg in Al matrix would have reached causing extreme lattice distortion. On the other hand excess Si will precipitate as spherical eutectic Si particles at the grain boundaries [188].

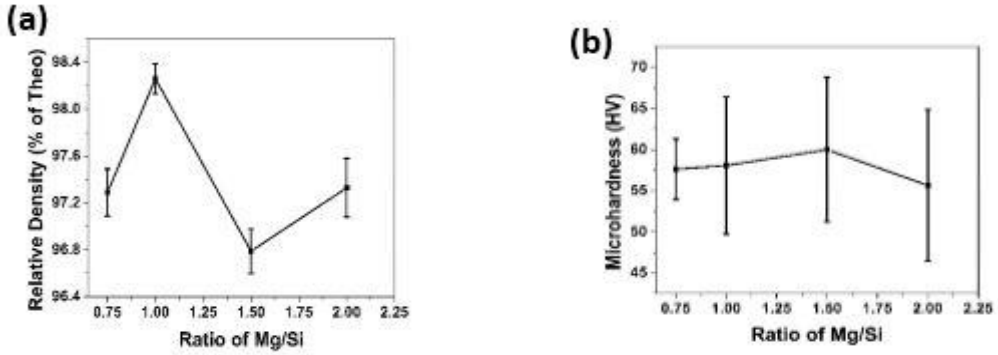

Fig. 6.1a: Mg/Si ratio vs Relative density **b)** Mg/Si ratio vs Microhardness

6.3 Metallographic studies

Fig. 6.2 a,b,c,d depicts the OM images of the hot compacted samples for different ratios (R=0.75,1,1.5,2). Processing through powder metallurgy route enabled the production of spheroidal or near spheroidal grains which is a fundamental requirement for semisolid process. Microscopic images comprise of primary α-Al dendrites with primary silicon particles dispersed throughout the specimen. Unetched samples at lower magnification reveals the presence of bright patched regions within the samples as seen in Fig. 3a and b. The primary Si particles appeared as coarse blocky shaped and eutectic Si formed a needle-like structures. This agreed well with the observations of Vijeesh and Narayan [189], that the microstructure

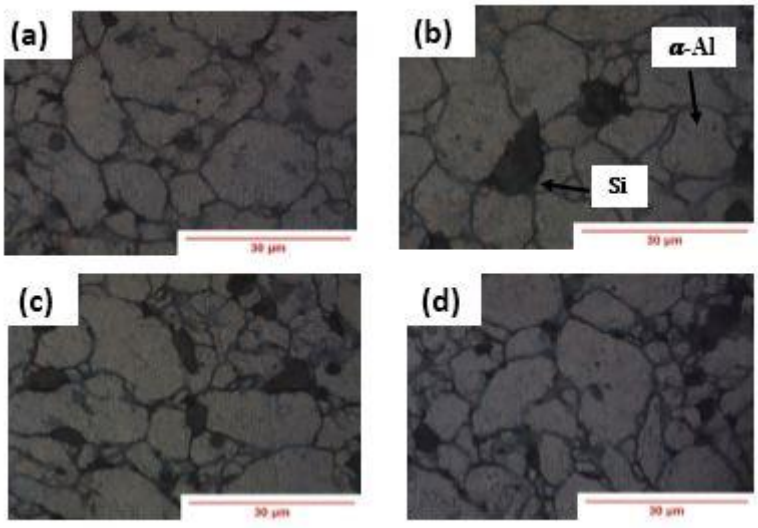

of Al–Si-Mg alloy consists of coarse Si particles along with the needle like eutectic Si at the interdendritic spaces where the morphology depends on the nucleation and cooling rates of the process.

Fig. 6.2: Optical micrographs of Al-Si-Mg alloy **a)** R=0.75 **b)** R=1 **c)** R=1.5 **d)** R=2

Fig. 6.3c and d shows the SEM and EDX analysis of the Al-Si-Mg alloy. SEM with EDX studies on the above regions confirmed the presence of Al, Si, Mg elements. Fig. 3b shows the bamboo-shoot shaped structure which consists of eutectic composition of Al+Si+Mg_2Si as evident from the phase diagram of ternary Al-Si-Mg. Hengcheng suggested that ternary eutectic reaction L → Al+Si+Mg_2Si occurs even under non-equilibrium solidification conditions. Within the network structure, it is hard to differentiate between eutectic Si and Mg_2Si as they could exhibit similar morphology and Mg_2Si grows on these eutectic Si [189] .

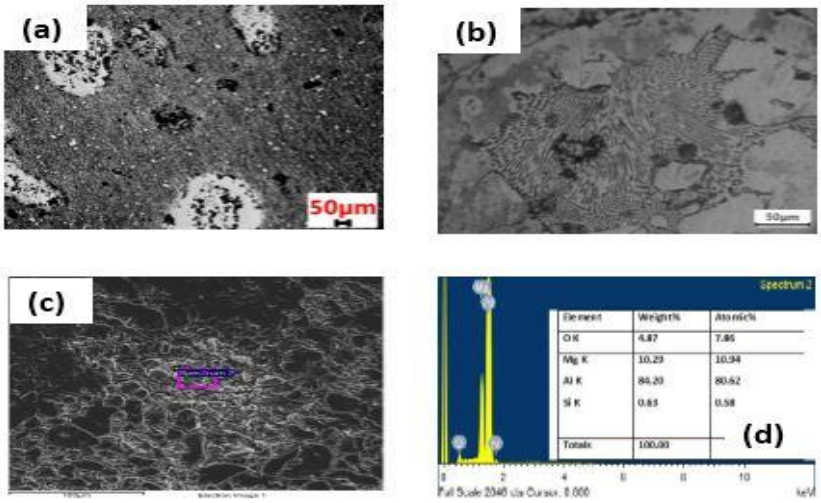

Fig. 6.3a) Macrostructure of Al-Si-Mg alloy **b)** Unetched view of eutectic regions **c)** SEM image of Mg_2Si precipitate **d)** EDX result of alloy

6.4 DTA analysis

DTA analysis provides the solidus and liquidus temperatures for the material. Fig. 6.4 shows the DTA plot for various ratios of R=0.75, 1, 1.5, 2 respectively. For R=1 two endothermic peaks were observed at 562 ^{o}C and 615 ^{o}C. This peak corresponds to the ternary eutectic reaction and the melting of primary $\boldsymbol{\alpha}$-phase of the alloy. Whereas for R=2, the peak has shrunk significantly. Similar peaks were observed in R=1.5 also. Fig 4a shows the solidus temperature as 558 ^{o}C and liquidus temperature as 582 ^{o}C with a range of 24 for Mg/Si ratio of 0.75. For the ratio R=1, the solidus temperature is 549 ^{o}C and the liquidus temperature is 573 ^{o}C with a range of 24. Similarly, for R=1.5 the solidus and liquidus temperatures are 550 ^{o}C and 578 ^{o}C respectively with a range of 28. In the case of R=2, the solidus and liquidus temperatures were 548 ^{o}C and 566 ^{o}C with a range of 18 ^{o}C. It can be seen that, as the ratio R increases, the eutectic temperature decreases. This could be because of the addition of Mg which has shifted the eutectic peak towards left and had a longer time period. This implies that by increasing the mushy zone, the alloy sensitivity towards the processing temperature decreases and thus, better control and an adjustable variation in mechanical properties could be achieved. The ternary eutectic reaction is observed only for Mg contents higher than 0.6% in Al-Si-Mg alloys [190]. Further, excess Si reduces the formation of a greater amount of (Mg + Si) in clusters and zones and Mg_2Si compared with the balanced alloys [191]. Whereas addition of Mg to excess Si alloys leads to reduction in the precipitation of primary Si and increases the size and number of Mg_2Si precipitates.

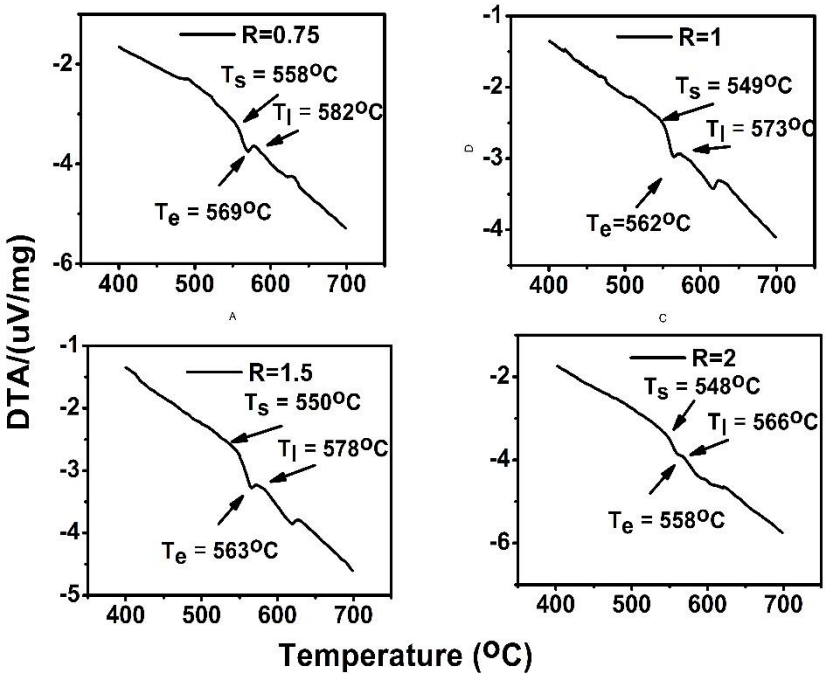

Fig. 6.4: DTA analysis of **a)** R=0.75 **b)** R=1 **c)** R=1.5 **d)** R=2

6.5 Semisolid Extrusion

Semisolid extrusion was carried out for three different temperatures namely i) near solidus (t_s), ii) near eutectic (t_e), and iii) near liquidus temperatures (t_l) and three different strain rates ($0.1s^{-1}$, $0.2\ s^{-1}$ and $0.3\ s^{-1}$) for all the ratios. Specimens extruded were free of macro defects. Specimens extruded at near liquidus and near eutectic temperatures were longer than the specimens at near solidus temperature which could be because of the increased liquid content at these temperatures. Extrudates were demarcated into tail, middle and head regions across the specimen. Further characterization like relative density, hardness and microstructure analysis were done on these regions. Fig. 6.5a shows the images of the extruded specimens for the near solidus temperature (t_s), near eutectic temperature (t_e), and near liquidus temperature (t_l) for the ratio R=0.75 and Fig 1b shows the demarcated regions of the individual specimen.

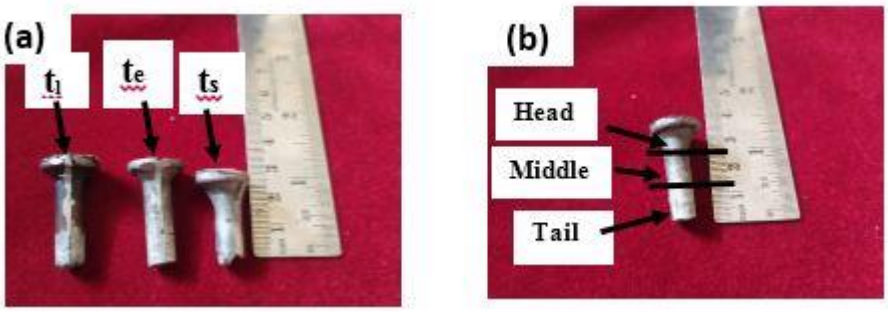

Fig 6.5a): Extruded samples images **b)**: Extruded sample showing different regions

By using Scheil's equation the amount of solid fraction in the sample has been calculated as

$$f_s=1-(T_s-T/T_s-T_l)^{(1/1-k)}$$

Where k is the partition coefficient taken as 0.13 [173]

T_s is the solidus temperature

T_l is the liquidus temperature

T is the extrusion temperature

The respective solid fraction for different ratios and their corresponding temperatures are shown in Table 6.1

Table 6.1: Respective Solid fraction for different ratios and corresponding extrusion temperature

Ratio	Extrusion Temperature (^{o}C)	Solid Fraction (%)
0.75	Near Solidus temperature (560)	94.23
	Near Eutectic temperature (570)	54.91
	Near Liquidus temperature (580)	9.96
1	Near Solidus temperature (555)	70.67
	Near Eutectic temperature (565)	37.25
	Near Liquidus temperature (575)	1.95
1.5	Near Solidus temperature (555)	86.19
	Near Eutectic temperature (565)	51.19
	Near Liquidus temperature (575)	12.23
2	Near Solidus temperature (550)	92
	Near Eutectic temperature (560)	37.25
	Near Liquidus temperature (570)	2.5

6.6 Microstructure Studies

Microstructural evaluation has been carried along the transverse section of the specimen at three regions namely tail, middle and head regions. Fig. 6.6 shows that the microstructure at the tail (Fig. 6.6a) and middle regions (Fig. 6.6b) are more spherical compared to the head region (Fig. 6.6c) where a greater number of grains are available with a distorted structure because of higher forces acting at the head region of the specimen. Since the extrusion has been carried at temperature close to the liquidus temperature, liquid content within the sample has considerably increased and more globular grains have been formed. Similarly, Fig. 6.6 d, e & f shows the microstructure of extruded samples at near eutectic temperature for the ratio R=1.5. The microstructure pattern observed is almost similar to the previous one (Fig 6.6 a, b, c) with the tail and middle region exhibiting spherical structure whereas the head region has more grains compared with the other regions. The number of grains has increased whereas the size of the grains has decreased because of the reduced liquid content. The grey regions (region A) represent the eutectic Si whereas the black regions (region B) represent the Mg_2Si precipitates as seen in B.J Kim work [192]. It has been observed that in Al-Si-Mg alloys the formation of Mg_2Si phases happens when the Mg/Si ratio reaches 1.73 and the area fraction will be equivalent to the amount of Mg present in the alloy[193]. Mg_2Si precipitates also increase the strength of the alloy[194]

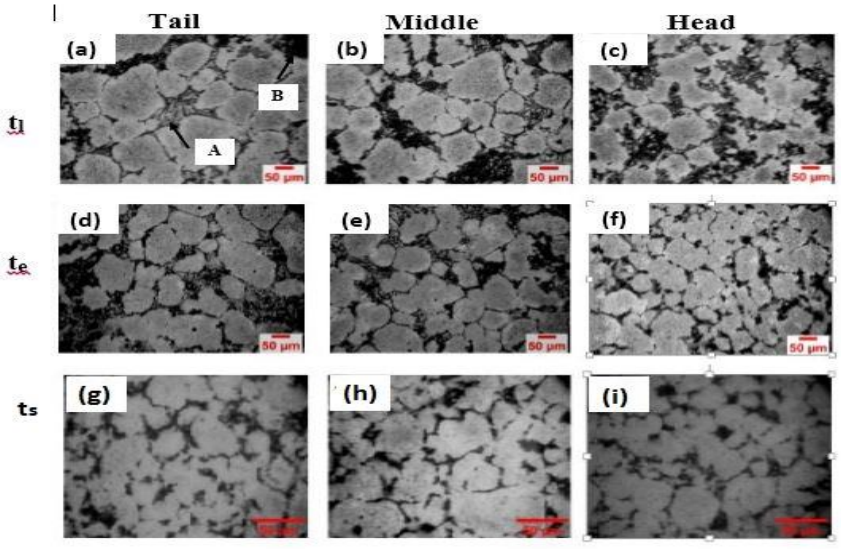

Fig. 6.6: OM images at: near liquidus temperature **a)** tail **b)** middle **c)** head : near eutectic temperature **d)** tail **e)** middle **f)** head: near solidus temperature **g)** tail **h)** middle **i)** head for R=1.5

Fig. 6.6 (g,h,and i) show the micrographs of the extruded samples at 550 ^{o}C. Specimens extruded at 550 ^{o}C shows a more distorted discontinuous grains throughout the specimen because of the lack of enough liquid content in the material. The grain size achieved was close to the compacted specimens size which means a high degree of deformation of grains has happened because of geometric recrystallization as stated by M. Schikorraa [183]

Fig. 6.7 shows the microstructure distribution along three different regions for different ratios of R=0.75, 1, 1.5 and 2 for the near eutectic temperatures of the samples respectively. As the ratio R increases, the grain size decreases which could be because of the increased Mg content [195]. But for the ratio R=2, the size decreases drastically because, at this composition, the semisolid range has almost disappeared which is evident from the DTA analysis (Fig. 6.4d) where the temperature range has shortened with no visible peaks. Samples containing 2.0 wt%

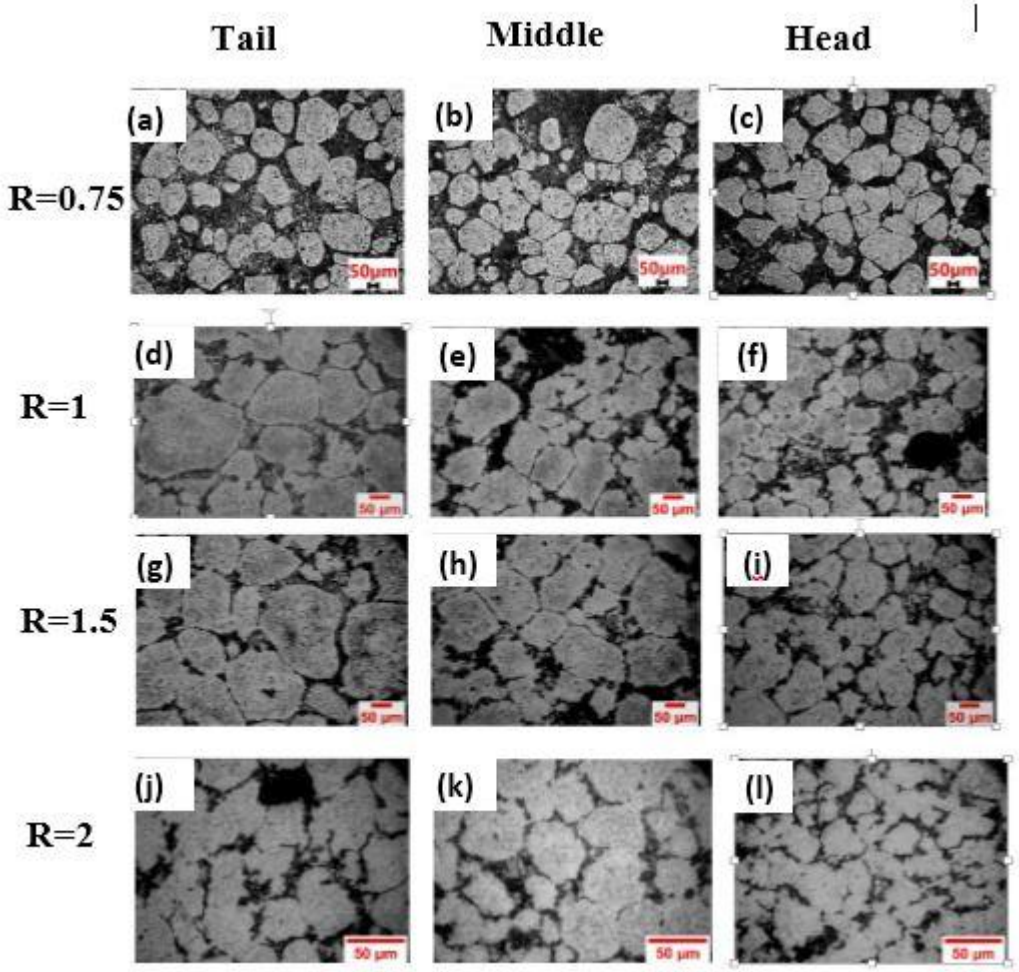

of Mg formed Mg_2Si phase with Chinese script morphology as seen in the work of Yamamotto [196]

Fig 6.7: OM images at near eutectic temperature **a)** R=0.75 tail **b)** R=0.75 middle **c)** R=0.75 head **d)** R=0.75 tail **e)** R=1 middle **f)** R=1 head **g)** R=1.5 tail **h)** R=1.5 middle **i)** R=1.5 head **j)** R=2 tail **k)** R=2 middle **l)** R=2 head

Fig. 6.8 a shows the relative density dependence on different extrusion temperatures of the specimen. It is observed that, irrespective of the ratio, maximum density has been achieved by the specimens extruded at liquidus temperature followed by solidus temperature. Compared with the compacted density (96%- 98%) the extruded specimens have achieved a density in the range of 88%-90% which means the liquid content for all the temperatures have increased. Similarly, for any particular temperature, a higher ratio leads to a higher relative density as seen from Fig. 6.8a.

Fig. 6.8 b shows the microhardness dependence on the extrusion temperatures. Hardness values are high for extrusion temperatures close to the liquidus range. This could be because of increased diffusion taking place at higher temperature leading to the solid solution strengthening of the material. Lower hardness being shown by samples extruded at solidus temperature because of lower rate of Mg diffusion. The increase in hardness values of Al-Mg-Si alloy can also be attributed to the distribution of Mg_2Si particles during solidification.

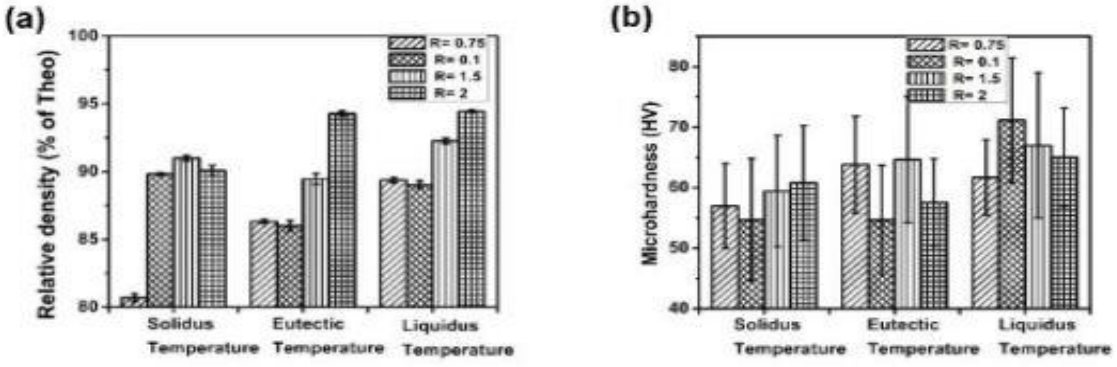

Fig. 6.8a) Extrusion temperature vs Relative density **b)** Extrusion temperature vs Microhardness

Fig. 6.9 a shows the dependence of relative density on different sections of the sample. Higher density was achieved at the top section as well as the middle section of the sample because of heterogeneous pressure distribution. A higher ratio was found to exhibit higher density. Fig. 6.9 b shows the plot of microhardness against the sections of the specimen. It was found that the tail and middle regions exhibited a higher hardness as compared to head region because of the presence of larger α-Al particles in the regions as seen from Fig. 6.7. Thus, the presence of Mg leads to solution strengthening and the presence of hard intermetallic Mg_2Si phase also leads to the increased strength of the material.

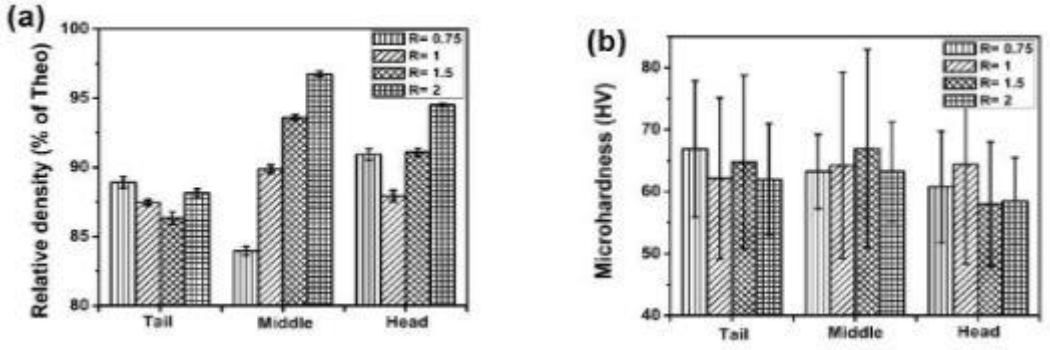

Fig. 6.9a) Different sections vs Relative density **b)** Different sections vs Microhardness

Fig. 6.10a shows the grain size analysis of the samples against the extrusion temperatures. Specimens extruded at the liquidus temperature and eutectic temperature offered the maximum grain size with the solidus temperature offering the minimum grain size. An R of 0.75 offered the maximum grain size while the subsequent ratios showed smaller grain size. It could be drawn that, beyond R=0.75, there is no significant diffusion of Mg into the solid solution because of which there is no further growth of the grain size. Moreover, the amounts of Mg_2Si particles present in matrix also play a lead role in increasing the hardness of the alloy. Hardness can also be affected by the size reduction of α-phase, distribution of Mg_2Si particles and the presence of Mg/Si cluster zones. Similarly, Fig. 6.10 b shows the circularity or shape factor of the grain (How much globular). Globular values close to 1 indicate a near spherical grains whereas far from 1 shows least globular grains. In the present work, liquidus temperature offered higher values of around 0.85 and the eutectic temperatures offered values of around 0.80 which is the next better value. On the other hand, solidus temperature produced least circular grains which could be because of the dynamic recrystallization caused by pure mechanical action.

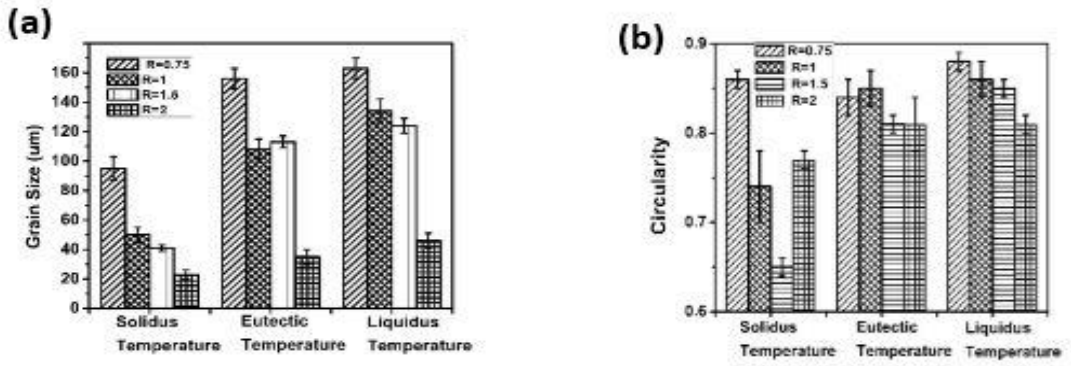

Fig. 6.10a) Extrusion temperature vs Grain size **b)** Extrusion temperature vs Circularity

6.7 Flow stress curves

Fig. 6.11 a,b, c, and d shows the flow stress curves for four different ratios at R=0.75,1,1.5 and 2 of Al-Si-Mg alloys for the three corresponding temperatures. The occurrence of single peak in stress strain curves signifies the presence of DRX phenomenon. Flow curves at solidus temperatures offers the highest peak stress values for all the ratios. Strain hardening mechanisms like dislocations pileups and their interactions leads to high stress requirements for further deformation. But the flow curves at liquidus and eutectic temperatures provide lower stress values. This is because, the dislocation movements increase with increasing temperature. Hence, recovery mechanisms overcome the hardening mechanisms, and thereby decreasing the stress values.

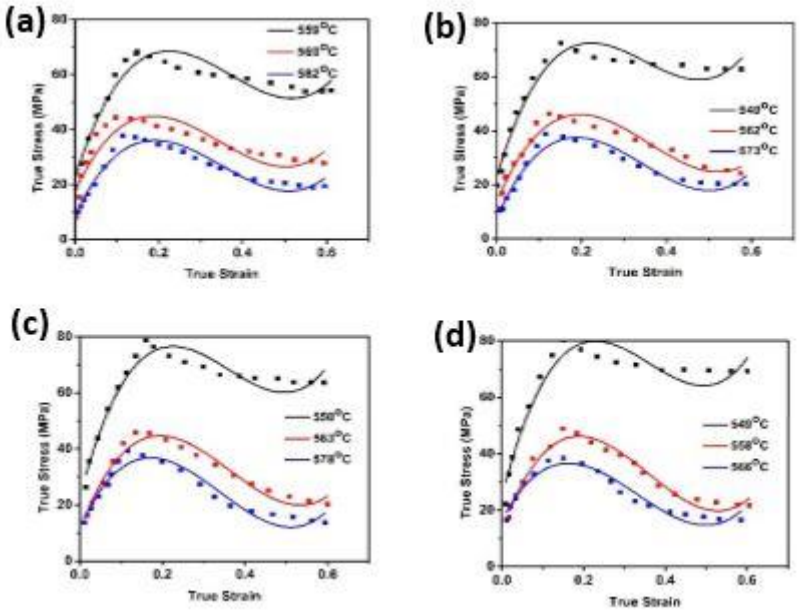

Fig. 6.11: Flow stress curves for Al-Si-Mg alloys for a) R=0.75 b) R=1 c) R=1.5 d) R=2

6.7.1 Prediction of critical strain for DRX

The DRX initiation begins at a critical strain. The onset of DRX can be determined from the inflection points in the plots of work hardening rate versus the true stress. Further, based on the strain hardening rate analysis, characteristic points like peak stress and peak strain can be found from the flow curves. According to Najafizadeh [181] inflection point was found by fitting a third order polynomial to the θ vs σ curves until peak point.

$$\theta = A\sigma^3 + B\sigma^2 + C\sigma + D \text{---------- (6.1)}$$

where A,B,C and D are the constants for the given conditions

At critical stress for initiation of DRX, the second derivative becomes zero. Thus, we have

$$6A\sigma_c + 2B = 0 \text{---------- (6.2)}$$

σ_c =-B/3A. Thus, the strain corresponding to the critical stress is called the critical strain. Fig 6.12 shows the true stress vs hardening rate curves for Al-Si-Mg alloys for different ratios. Critical strain values for various ratios and temperatures are shown in Table 6.2. Table 6.3 depicts the hardening rate equations of the alloy.

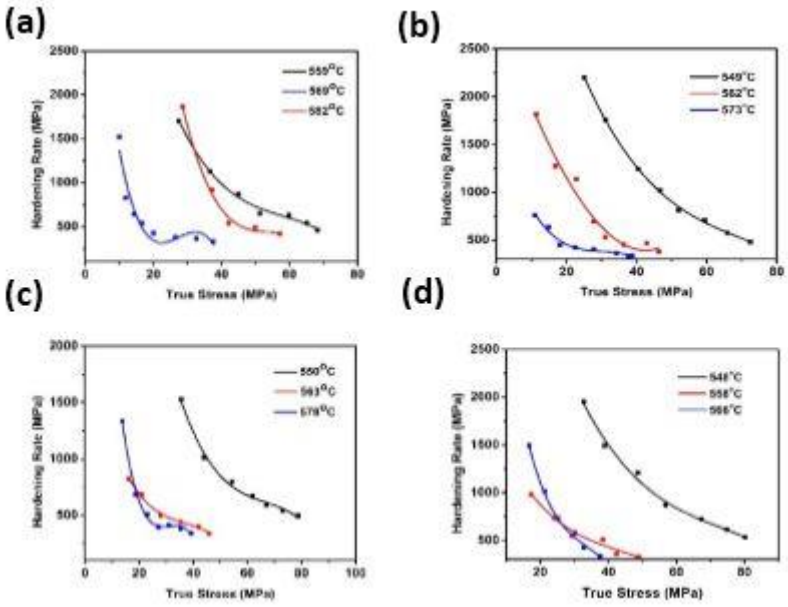

Fig. 6.12: True stress vs Hardening rate curves for Al-Si-Mg alloys for **a)** R=0.75 **b)** R=1 **c)** R=1.5 **d)** R=2

Table 6.2: Critical strain values for different R values

Critical strain	**Temperature**	**0.75**	**1**	**1.5**	**2**
ε_c	Solidus temperature	0.095	0.14	0.113	0.11
	Eutectic temperature	0.125	0.10	0.080	0.11
	Liquidus temperature	0.08	0.78	0.07	0.077

Table 6.3: Hardening rate equations for different R values and temperatures

Ratio	Temperature	Hardening rate equation
0.75	Solidus temperature	$y = -0.0249x^3 + 4.3491x^2 - 265.45x + 6237.1$
	Eutectic temperature	$y = -0.083x^3 + 13.468x^2 - 730.84x + 13695$
	Liquidus temperature	$y = -0.091x^3 + 7.9836x^2 - 232.1x + 2605.6$
1	Solidus temperature	$y = -0.011x^3 + 2.3347x^2 - 179.22x + 5403.9$
	Eutectic temperature	$y = 0.0069x^3 + 0.7775x^2 - 103.34x + 2853.1$
	Liquidus temperature	$y = -0.0505x^3 + 4.5819x^2 - 140.32x + 1831$
1.5	Solidus temperature	$y = -0.0214x^3 + 4.2728x^2 - 293.03x + 7490.6$
	Eutectic temperature	$y = -0.0283x^3 + 3.1339x^2 - 123.01x + 2123.5$
	Liquidus temperature	$y = -0.1863x^3 + 17.43x^2 - 540.31x + 5952.7$
2	Solidus temperature	$y = -0.0114x^3 + 2.4905x^2 - 195.62x + 6066.4$
	Eutectic temperature	$y = -0.0173x^3 + 2.2308x^2 - 107.46x + 2269.7$
	Liquidus temperature	$y = -0.1338x^3 + 13.387x^2 - 472.23x + 6264.6$

6.8 Chapter Summary

Al-Si-Mg alloys having ratio (Mg/Si) R=1.5 showed the presence of binary eutectic (Al+Mg_2Si), and ternary eutectic (Al+Mg_2Si+Si) particles. Similarly for R=2 the material loses its thixotropic property as is evident from the DTA results. Critical strain values decrease with increasing temperature due to thermal softening phenomenon. Grain size for R=0.75 was considerably higher than other ratios as maximum solubility limit could have been reached for this ratio. Beyond this ratio free Mg was not available to be consumed by the alpha phase. Hence, resulting in the decrease of the grain size.

Chapter-7

Prediction of α-Al phase using Deep Learning models on thixoextruded Al-Si-Mg alloys

7.1 Introduction

The UNET was developed initially for the study of biomedical image segmentation. The architecture of the model consists of two different paths where the first path is the contraction or encoder path and the second path is the symmetric expanding or decoder path. The encoder path captures the context of the image and the decoder path enables the localization precisely by employing the transposed convolutions. The implementation of the Unet model was done by utilizing an open source machine learning library Keras under another library Tensor flow by google. The code has been run in open source cloud platform Google colab. Training was done with training parameters such as epochs=100, learning rate=0.01 and batch size =32. The training dataset consists of 80 images whereas the validation set consists of 20 images. The optimizer chosen is Adam. This is one of the best optimizers for image segmentation problems. Optimizer function calculates the gradient of error in back propagation algorithm.

The experiments were carried out on an Intel Core i5-7500 CPU with an NVIDIA GeForce GTX 1050 card. The images of the training set were used to train the neural network, Nearly 90% of the partial images were used for training the neural network after the image cropping process, while the remaining 10% were used to optimize and adapt the parameters of the neural networks during the training.

7.2 Fully Convolutional Neural Network

A fully convolutional network is one of the first architectures without fully interconnected layers. Apart from the fact that it can be trained end-to-end, it can process inputs of any size for individual pixel prediction (e.g. semantic segmentation). It is a general architecture that effectively uses transposed convolutions as a trainable sampling technique.

The Fully Convolutional Neural Network (FCN) is the model that comprises of only convolutional layers and no fully connected dense layers for the image segmentation task. The main idea of FCN is to extract heat map features from the convolution net without converting into dense output like in the case of classification tasks. The successful image classification models like VGG16, Alexnet and GoogLeNet are used as the backbone for FCN variants. The FCN was initially applied on the PASCAL-VOC2011 dataset that has 21 classes of pixels. The coarse feature maps extracted from the heat map generated from the convolution net from a backbone architecture is passed into a 1x1 convolution with 21 filters for pixel wise classification. Then the output of 1x1 convolution layer is up scaled using bilinear interpolation technique. Fig 7.1 shows the segmentation results of FCN model.

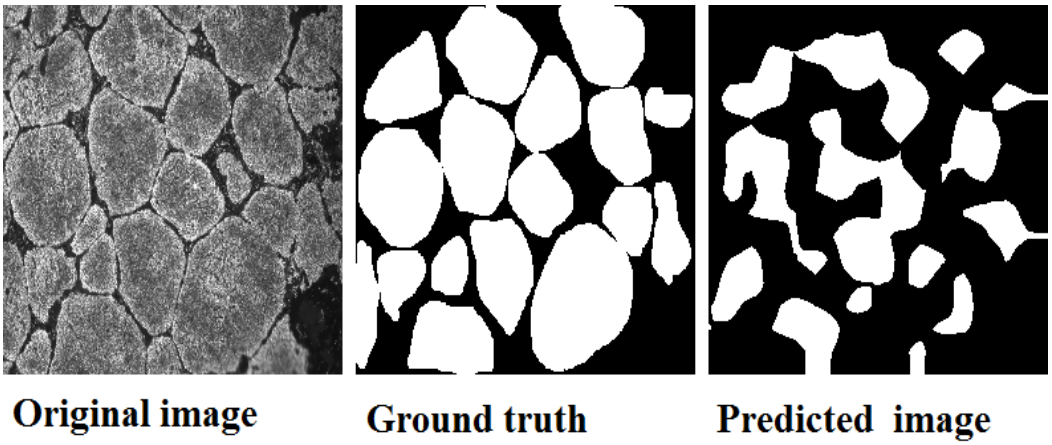

Fig. 7.1: Segmentation result of FCN

However, the output of FCN is coarse and fine details and boundary delineation are missing. The coarse nature of the output are mainly due to the striding and the loss of finer details along the way in deeper layers. This problem is addressed by introducing skip ahead connections from lower layers to the higher layers. The skip connections have relevant up-sampling filters to convert their input to match their output spatial dimensions. The other way to improve predictions from coarse to finer is to decrease the stride size but that would ultimately incur computational costs. The FCN was the first in line of architecture to apply CNN fully end-to-end to solve the segmentation problems and it was followed suit by various models including Unet and its variants that exploit the FCN idea. Fig. 7.2a) and b) shows the loss and accuracy graphs of FCN model

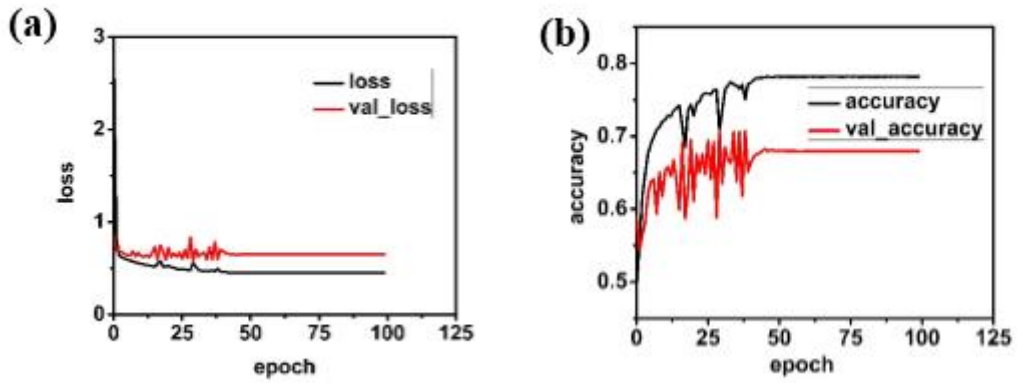

Fig. 7.2 a) Loss curves of FCN **b)** Accuracy curves of FCN

7.3 Unet

The main idea is to get FCN to keep the high level functions in the early layer of the decoder. To do this, they introduce long skip connections to localize the segmentations. In this way, high resolution features (but semantically low) from the encoder path are combined and reused with the up sampling output. Unet is also a symmetrical architecture.

Unet is a very popular architecture originally designed for biomedical image segmentation problem. Since microstructure image segmentation closely resembles the biomedical image segmentation problem, the Unet can be applied for microstructure image segmentation also. Unet architecture is named after its U shaped structure with contracting and expanding path. The contracting phase consists of Convolutional Neural Networks (CNNs) and max pooling layers stacked together. The expanding phase consists of up-convolution operations applied to feature maps. Here, each convolution has 3x3 kernel filter to learn the feature maps from the inputs and it is followed by the non-linear element-wise activation ReLU. It is further followed by a max pooling layer of kernel 2x2 and stride of 2, effectively down sampling the feature maps by a factor of 2.

The decoder layers up sample the feature maps with up-convolutions and they reduce the feature maps count by a factor of 2. The decoder layers are just inverse of encoder layers along with feature maps being concatenated from the corresponding encoder layer through skip connections mechanism. The skip connection mechanism enables the network to learn fine features like boundary delineation that are lost while down sampling happens at the

encoder layers. The feature maps concatenated through skip connections are cropped due to the loss of boundary pixels in every convolution layer. It should be noted here that the convolutions applied are unpadded convolutions. So naturally there is a loss at the boundary pixels. Unet is found to be very efficient in segmentation even with lower amount of annotated data. Fig. 7.1 shows the segmentation results of Unet model. Fig. 7.2a) and b) shows the loss and accuracy graphs of Unet model.

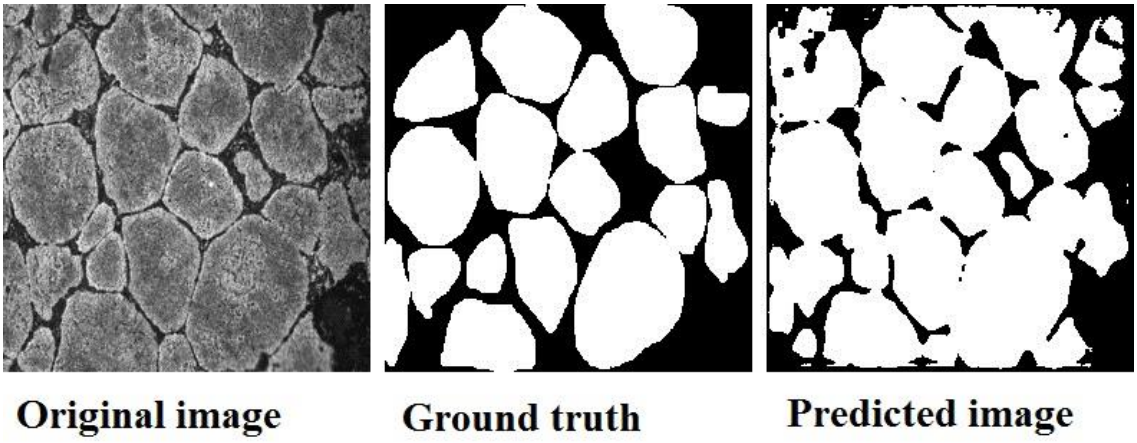

Fig. 7.3: Segmentation result of UNET

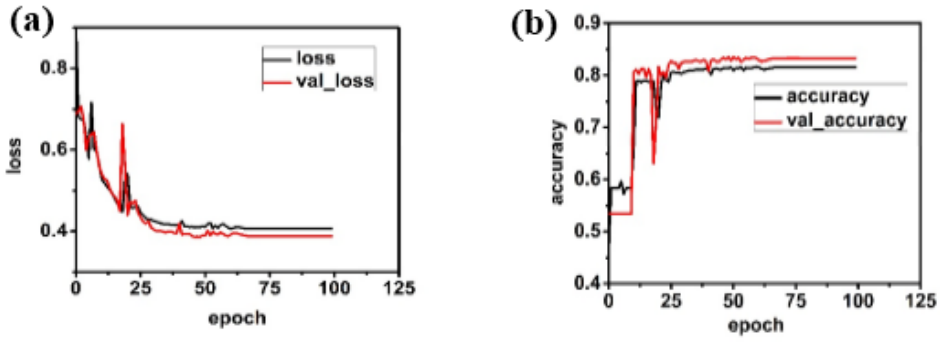

Fig. 7.4 a) Loss curves of Unet **b)** Accuracy curves of Unet

7.4 Segnet

Segnet belongs to the encoder decoder style of neural network architecture. It contains 13 Convolutional Neural Network (CNN) layers in the encoder part and corresponding equal 13 up-sampling decoder layers. Finally, the features are fed into a pixel-wise classifier. The 13-CNN layer encoder is inspired from the first 13 CNN layer of VGG16 for object classification. Therefore, the pre-trained weights of VGGNet can also be used here as a transfer learning technique. The highly convolutional encoder-decoder architecture reduces the trainable parameters considerably making the training faster and inference easier. It is estimated in the original paper that Segnet architecture reduces parameter space from 134Million to 14.7Million when compared with other related and recent architectures. The final classification layer contains soft max activation to classify each pixel into its corresponding class probability. Depending upon the problem of semantic segmentation and its classes the final classifier weights may differ. Fig. 7.1 shows the segmentation results of Segnet model

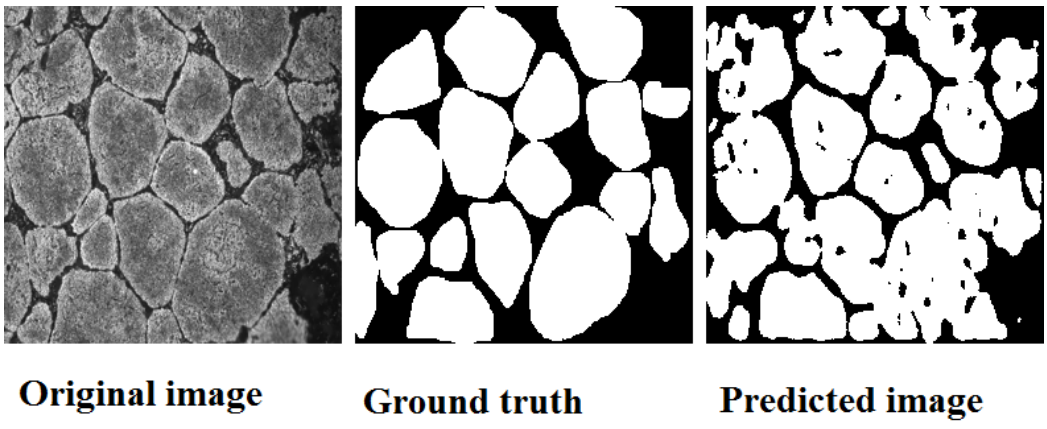

Fig. 7.5: Segmentation result of Segnet

Each encoder layer performs convolution with filters to extract feature maps. Those feature maps are then batch normalized to reduce the co-variant shift in the data. They are then passed into an element-wise ReLU unit that add non-linearity to the model's learning. The ReLU operation is just the maximum of zero and its input, effectively altering the negative values to zero and keeping the same positive values. After the ReLU operation, max pooling is applied with kernel of 2x2 and a non-overlapping stride of 2, and the max pooling operation reduces the dimensions of the input by a factor of 2. The model stores max pooling indices with 2bits for each pooling operation. This information of max pooling indices is later used in the up sampling operations in the corresponding decoder layers. This mechanism of storing max pooling indices and reusing them in the decoder layers reduces the scarcity in the decoder output and also alleviates the loss of boundary details introduced by max pooling layers. Boundary delineation is vital for the class of segmentation problems. The max pooling indices uses only 2bits to store each pooling operation thereby results in lesser memory footprint of the model and also suits for quicker inference. Fig. 7.2a) and b) shows the loss and accuracy graphs of Segnet model

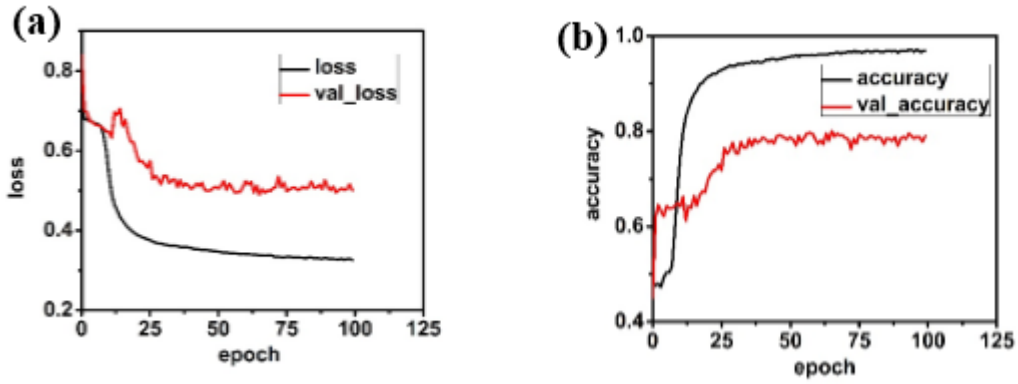

Fig. 7.6:a) Loss curves of Segnet **b)** Accuracy curves of Segnet

7.5 ResUnet++

ResUnet++ is a semantic segmentation model based on ResNet (Residual Neural Network) 16 and U-Net. The ResUnet++ network integrates residual module and U-Net network, which is able to effectively overcome excessive parameters and gradient dispersion caused by the deepened network layer. In addition, the new residual learning unit in ResUnet is easy to train, which not only improves the training speed of the model, but also allows the network to get fewer parameters without reducing accuracy. Fig. 7.1 shows the segmentation results of Resunet++ model

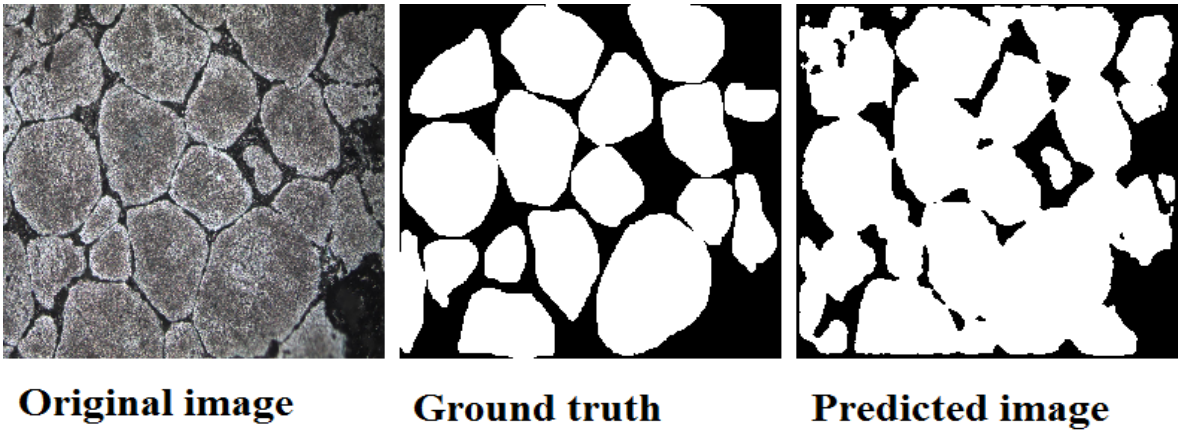

Fig. 7.7: Segmentation result of ResUNet++

ResUnet++ stands on top of residual network ResNet and Unet for segmentation. It derives the combined strength of Resnet and Unet. Further ResUnet++ employs residual blocks, squeeze and excite blocks, Atrous Spatial Pyramid Pooling (ASPP) and attention layers to achieve the state of the art performance in segmentation tasks. The residual connections in the model makes it suitable for deeper layer training overcoming the vanishing gradient and degradation problems that plaque deeper networks. The residual connections further reduces the training cost also. The Resnet image classification model that proposed the residual connections for deeper neural network training is the backbone of ResUnet++.

Each residual unit in the architecture consists of Batch normalization used to reduce internal covariant shift, convolutional layer with filters for feature extraction and ReLU activation for non-linear function of the model. The filters used in the convolutions have 3x3 kernel and an identity mapping from encoder input to output. Instead of using max pooling to reduce spatial

dimensions here strided convolution is applied in the first convolution of the encoder block. Each encoder block is passed through a squeeze and excitation block that assigns weights to feature maps and thereby enhancing relevant feature maps and suppressing the irrelevant ones. ASPP acts as a bridge between the encoder layer and the decoder layer, introducing broader context into the feature maps by convolutions. The decoder blocks also have residual units whereas they have attention layer as their entry unit. The attention layer in the decoder block enhances the feature maps by the attention mechanism.

The decoder blocks have up sampling mechanism by nearest neighborhood and a corresponding skip connection from the encoder block. The output of the decoder block is again fed into a ASPP block and then 1x1 convolution with sigmoid activation is applied to produce the segmentation mask. The contributions of ResUnet++ model are the squeeze and excitation layer, ASPP and attention layer into the segmentation pipeline. Fig. 7.2a) and b) shows the accuracy and loss graphs of Resunet++ model. Table 7.1 shows the comparison chart of the scores for the above models.

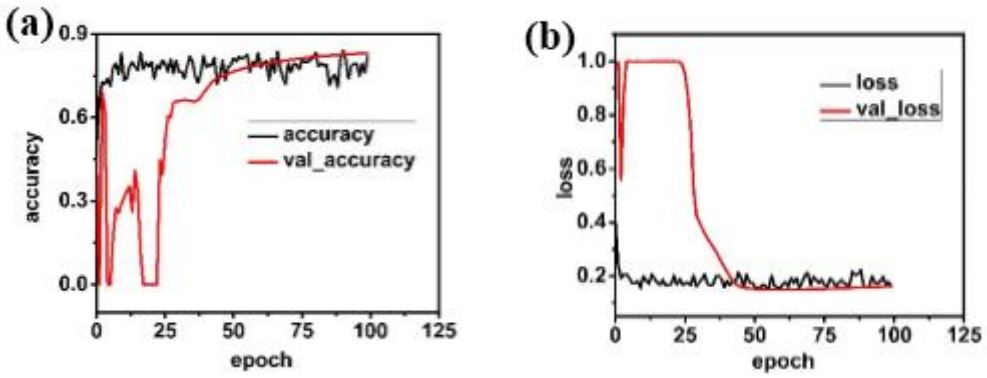

Fig. 7.8: a) Accuracy curves of Resunet++ **b)** Loss curves of Resunet++

To make a quantitative comparison between the experimental results and the predicted ones, we introduce four quantitative statistical indicators: (a) true positive (TP): a pixel that is essentially a α region and is precisely identified as α region; (b) false negative (FN): a pixel that is actually a α region but is recognized as a background point; (c) true negative (TN): a pixel that is essentially a background point and is precisely identified as a background point;

(d) false positive (FP): a pixel that is essentially a background point but is recognized as a $\boldsymbol{\alpha}$ region; According to the four quantitative statistical indicators defined above, the assessment criterion we can evaluate including IOU and DICE score as follows

The IOU is defined by IOU = TP / (TP + FN + FP)

Dice= 2TP / ((TP+FP) + (TP+FN))

SCORE / MODEL	FCNN	UNET	SEGNET	RESNET
IOU	**0.51**	**0.72**	**0.72**	**0.85**
DICE	**0.68**	**0.83**	**0.83**	**0.62**

Table 7.1: Comparison table based on IOU and Dice score

7.6 Chapter Summary

Four different deep learning models have been used for $\boldsymbol{\alpha}$ phase identification from Optical microscope images. Among these FCNN offered, the least score which can be seen from the predicted image whereas signet and resnet++ predicted the features with much better accuracy.

CHAPTER 8
Conclusions

8.1 Summary of the research findings

The composition corresponding to 4% Si and 0.6% Mg were found to be the optimal one with the sintering temperatue and time being 550 ^{o}C and 60 min. The hot compacts thus fabricated had a minimum density of 92% Al-4Si-0.6Mg alloy and 94% for Al-4Si alloy.

Specimens extruded at 580 ^{o}C and a strain rate of 0.3 s^{-1} offered the highest density for both the Al-4Si alloy and Al-4Si-0.6Mg alloy.

Microstructural analysis along the longitudinal direction revealed the presence of fibrous grains and globular α-Al phase and the primary-Si phase along the transverse direction. Al-4Si alloy had a needle shaped silicon particles whereas addition of Mg converted this morphology into spheroidal shape which could be found from the SEM image. Similarly the grain size also increased because of the addition of Mg.

Addition of Mg decreased the relative density of the extruded Al-4Si alloy by 1%-2%. But the hardness of the Al-4Si-0.6Mg alloy got increased by approximately 30%. Samples extruded close to the eutectic temperature had better relative density and hardness values along with the maximum material being conserved.

Flow stress curves of Al-4Si-0.6Mg alloy shows that, up to peak strain, the dominant mechanism is work hardening which increases the stress values. After that, the stress decreases and reaches a stable state which can be attributed to the DRV and DRX mechanism.

Grain growth modelling revealed that holding temperature had much larger significance than holding time. Beyond 600^{0}C, the specimens were not stable and the microstructures were fluctuating in terms of properties.

Experimental versus calculated values for grain growth model, peak strain, critical strain, dynamically recrystallized grain size, and 50% recrystallized grain were found to agree well with each other with maximum error being 19%.

Experimental and numerical methods were modelled and validated for predicting the grain size in extrusion of powdered Al-4Si-0.6Mg alloy. The obtained models were applied to the numerical models and they agree well with the experimental values. Coarse grains were observed for temperatures above 580 ^{0}C when other process parameters like die angle and strain rate were kept constant.

The results indicate that the bottom section of the extruded profile has coarse grains because of the presence of higher liquid content whereas smaller grains at the top end of the specimen because of the insufficient liquid and the higher forces acting at the top end of the specimen.

Al-Si-Mg alloys are fabricated by powder forming process. A spheroidal morphology of $\boldsymbol{\alpha}$-Al grains was characterized in the Al-Si-Mg alloy. Interdendritic regions consist of binary eutectic (Al+Mg_2Si), and ternary eutectic (Al+Mg_2Si+Si) particles.

Specimens extruded at temperatures close to eutectic temperatures offered high hardness, better relative density, more spherical grains compared with the liquidus temperature.

Al-Si-Mg alloys with Mg/Si (R) ratio of up to 1.5 offered better mechanical properties with a clear thixotropic range. For R=2 there was a significant loss in thixotropic property which can be seen in DTA (Fig. 6.4) and the grain size reduction from Fig. 6.10.

Among the deep learning models for phase prediction, FCNN model offered the least prediction with IOU score of 0.51 which could be because of being one of the earliest models developed. On the other hand ResUnet++ offered a score of 0.85.

Models were not able to predict the lighter grain boundaries with much higher accuracy. Resunet++ and Unet predicted the boundaries with reasonable accuracy. But even though Segnet model had higher values it over predicted the dark spots in the images.

8.2 Scope for future work

The extensive research effort on the deformation characteristics of P/M processed Al-Si-Mg preforms utilizing experimental and modelling under various deformation conditions during hot extrusion can be applied to a wide range of dimensions of future research work as shown below:

1) Addition of rare earth elements to modify the grain size as well as the mechanical properties of Al-4%Si-0.5%Mg after hot extrusion.

2) Failure studies on the compacted samples and extruded samples could be done both experimentally and numerically.
3) Dislocation based microstructure modelling both experimentally and numerically would provide better understanding of the mechanisms affecting the evolution of grains in Al-Si-Mg alloys.
4) Further advanced deep learning algorithms can be used for identification of morphological features of Si in the images thereby enabling better identification of features can be carried out.
5) Automatic segmentation of the images can also be investigated to reduce the human error involved in it.

References

[1] T. Dursun and C. Soutis, “Recent developments in advanced aircraft aluminium alloys,” *Mater. Des.*, vol. 56, pp. 862–871, 2014.

[2] L. Zhu, N. Li, and P. R. N. Childs, “Light-weighting in aerospace component and system design,” *Propuls. Power Res.*, vol. 7, no. 2, pp. 103–119, 2018.

[3] C.-C. Huang and J.-H. Cheng, “An investigation into the forming limits of sintered porous materials under different operational conditions,” *J. Mater. Process. Technol.*, vol. 148, no. 3, pp. 382–393, 2004.

[4] S. Nafisi and R. Ghomashchi, *Semi-solid processing of aluminum alloys*. Springer, 2016.

[5] R. E. Sanders, “Technology innovation in aluminum products,” *JOM*, vol. 53, no. 2, pp. 21–25, 2001.

[6] H. J. McQueen and N. D. Ryan, “Constitutive analysis in hot working,” *Mater. Sci. Eng. A*, vol. 322, no. 1–2, pp. 43–63, 2002.

[7] I. Tamura, H. Sekine, and T. Tanaka, *Thermomechanical processing of high-strength low-alloy steels*. Butterworth-Heinemann, 2013.

[8] G. T. Halmos, *Roll forming handbook*. Crc Press, 2005.

[9] H. J. McQueen, “Historical aspects of thermomechanical processing for steels,” in *Materials science forum*, 2007, vol. 539, pp. 4397–4404.

[10] G. E. Dieter and D. J. Bacon, *Mechanical metallurgy*, vol. 3. McGraw-hill New York, 1976.

[11] R. N. Lumley, I. J. Polmear, and A. J. Morton, “Temper developments using secondary ageing,” in *Materials forum*, 2004, vol. 28, pp. 85–95.

[12] T. R. Prabhu, “An overview of high-performance aircraft structural Al alloy-AA7085,” *Acta Metall. Sin. (English Lett.)*, vol. 28, no. 7, pp. 909–921, 2015.

[13] J. T. STALEY, “Physical Metallurgy and the Effect of Alloying Additions in Aluminum Alloys,” *Handb. Alum.*, p. 81, 2003.

[14] L. A. Lourençato and E. J. Zoqui, “Evolution of Microstructure in Semi-Solid of Al-

2wt% Si-0.5 wt% Mg and Al-4wt% Si-05wt% Alloys during Isothermal Holding," in *Advanced Materials Research*, 2015, vol. 1082, pp. 152–166.

[15] S. Hashmi, *Comprehensive materials processing*. Newnes, 2014.

[16] C. Suryanarayana, "Mechanical alloying and milling," *Prog. Mater. Sci.*, vol. 46, no. 1–2, pp. 1–184, 2001.

[17] R. M. German, "Powder metallurgy science," *Met. Powder Ind. Fed. 105 Coll. Rd. E, Princeton, N. J. 08540, U. S. A, 1984. 279*, 1984.

[18] J. Campbell, *Complete casting handbook: metal casting processes, metallurgy, techniques and design*. Butterworth-Heinemann, 2015.

[19] S. Müller, T. Schubert, F. Fiedler, R. Stein, B. Kieback, and L. Deters, "Properties of sintered P/M aluminium composites," *Proc. Eur.*, pp. 325–330, 2011.

[20] R. M. German, "Powder metallurgy of iron and steel," *John! Wiley Sons, Inc, 605 Third Ave, New York, NY 10016, USA, 1998. 496*, 1998.

[21] P. W. Lee *et al.*, "ASM handbook," *Volume*, vol. 7, pp. 287–301, 1998.

[22] A. S. M. international H. Committee, "ASM Handbook: Powder Metal Technologies and Applications Vol. 7," *ASM Int.*, 1998.

[23] H. V Atkinson, "Modelling the semisolid processing of metallic alloys," *Prog. Mater. Sci.*, vol. 50, no. 3, pp. 341–412, 2005.

[24] Z. Fan, "Semisolid metal processing," *Int. Mater. Rev.*, vol. 47, no. 2, pp. 49–85, 2002.

[25] A. de Figueredo, *Science and technology of semi-solid metal processing*. North American Die Casting Assoc., 2001.

[26] D. Liu, H. V Atkinson, P. Kapranos, and H. Jones, "Effect of heat treatment on properties of thixoformed high performance 2014 and 201 aluminium alloys," *J. Mater. Sci.*, vol. 39, no. 1, pp. 99–105, 2004.

[27] D. Liu, H. V Atkinson, P. Kapranos, W. Jirattiticharoean, and H. Jones, "Microstructural evolution and tensile mechanical properties of thixoformed high performance aluminium alloys," *Mater. Sci. Eng. A*, vol. 361, no. 1–2, pp. 213–224, 2003.

[28] D. Liu, H. V Atkinson, and H. Jones, “Thermodynamic prediction of thixoformability in alloys based on the Al–Si–Cu and Al–Si–Cu–Mg systems,” *Acta Mater.*, vol. 53, no. 14, pp. 3807–3819, 2005.

[29] M. R. Ghomashchi, “Die filling and solidification of Al-Si alloy in high pressure die casting,” *Scand. J. Metall.*, vol. 22, no. 2, pp. 61–67, 1993.

[30] M. R. Ghomashchi, “High-pressure die casting: effect of fluid flow on the microstructure of LM24 die-casting alloy,” *J. Mater. Process. Technol.*, vol. 52, no. 2–4, pp. 193–206, 1995.

[31] G. J. Baxter, Q. Zhu, and C. M. Sellars, “Effects of magnesium content on hot deformation and subsequent recrystallization behavior of aluminum-magnesium alloys,” in *Proceedings of International Conference on Aluminum Alloys (ICAA)*, 1998, vol. 6, pp. 1233–1238.

[32] S. H. Cho, Y. S. Kim, Y. C. Yoo, S. H. Rhim, and S. I. Oh, “The prediction of deformation resistance of Al6061 during hot deformation,” *J. Kor. Inst. Met. Mater*, vol. 36, no. 4, pp. 502–508, 1998.

[33] W. J. Kwak, K. J. Lee, O. J. Kwon, and S. M. Hwang, “Prediction of recrystallization behaviors in hot forging by the finite element method,” *J. Kor. Soc. Technol. Plast.*, vol. 5, no. 4, pp. 305–319, 1996.

[34] J. R. Cho, W. B. Bae, W. J. Hwang, and P. Hartley, “A study on the hot-deformation behavior and dynamic recrystallization of Al–5 wt.% Mg alloy,” *J. Mater. Process. Technol.*, vol. 118, no. 1–3, pp. 356–361, 2001.

[35] G. Lange, “Der Wärmehaushalt beim Strangpressen,” *Int. J. Mater. Res.*, vol. 62, no. 8, pp. 571–577, 1971.

[36] M. Zhou *et al.*, “Experiment and finite element analysis of compaction densification mechanism of Ag-Cu-Sn-In mixed metal powder,” *Powder Technol.*, vol. 313, pp. 68–81, 2017.

[37] B. Wikman, A. Svoboda, and H.-Å. Häggblad, “A combined material model for numerical simulation of hot isostatic pressing,” *Comput. Methods Appl. Mech. Eng.*, vol. 189, no. 3, pp. 901–913, 2000.

[38] D.-C. Chen and C.-S. You, “Finite element simulation on high extrusion-ratio

hydrostatic extrusion of porous material," in *Advanced Manufacturing Processes and Technologies Conference*, 2009, pp. 11–20.

[39] S. Y. Wang, P. Z. Zhang, S. Y. Zhou, D. B. Wei, F. Ding, and F. K. Li, "A computer vision based machine learning approach for fatigue crack initiation sites recognition," *Comput. Mater. Sci.*, vol. 171, p. 109259, 2020.

[40] Z. Chen and S. Daly, "Deformation twin identification in magnesium through clustering and computer vision," *Mater. Sci. Eng. A*, vol. 736, pp. 61–75, 2018.

[41] B. L. DeCost and E. A. Holm, "Characterizing powder materials using keypoint-based computer vision methods," *Comput. Mater. Sci.*, vol. 126, pp. 438–445, 2017.

[42] Y. LeCun, Y. Bengio, and G. Hinton, "Deep learning. nature 521 (7553), 436-444," *Google Sch. Google Sch. Cross Ref Cross Ref*, 2015.

[43] J. Long, E. Shelhamer, and T. Darrell, "Fully convolutional networks for semantic segmentation," in *Proceedings of the IEEE conference on computer vision and pattern recognition*, 2015, pp. 3431–3440.

[44] V. Badrinarayanan, A. Kendall, and R. Cipolla, "Segnet: A deep convolutional encoder-decoder architecture for image segmentation," *IEEE Trans. Pattern Anal. Mach. Intell.*, vol. 39, no. 12, pp. 2481–2495, 2017.

[45] O. Ronneberger, P. Fischer, and T. Brox, "U-net: Convolutional networks for biomedical image segmentation," in *International Conference on Medical image computing and computer-assisted intervention*, 2015, pp. 234–241.

[46] H. Zhao, X. Qi, X. Shen, J. Shi, and J. Jia, "Icnet for real-time semantic segmentation on high-resolution images," in *Proceedings of the European conference on computer vision (ECCV)*, 2018, pp. 405–420.

[47] S. M. Azimi, D. Britz, M. Engstler, M. Fritz, and F. Mücklich, "Advanced steel microstructural classification by deep learning methods," *Sci. Rep.*, vol. 8, no. 1, pp. 1–14, 2018.

[48] M. Li, D. Chen, S. Liu, and F. Liu, "Grain boundary detection and second phase segmentation based on multi-task learning and generative adversarial network," *Measurement*, vol. 162, p. 107857, 2020.

[49] P. Kapranos, “Semi-solid metal processing–a process looking for a market,” in *Solid State Phenomena*, 2008, vol. 141, pp. 1–8.

[50] F. H. Froes, “P/M Aerospace, Defense and Demanding Applications--1995,” 1995.

[51] H. J. Rack, “Fabrication of high performance powder-metallurgy aluminum matrix composites,” *Mater. Manuf. Process*, vol. 3, no. 3, pp. 327–358, 1988.

[52] W. C. Harrigan, “Scaling up particulate-reinforced aluminum composites for commercial production,” *JOM*, vol. 43, no. 8, pp. 32–35, 1991.

[53] P. S. Gilman, “Discontinuously reinforced aluminum: Ready for the 1990s,” *JOM-Journal Miner. Met. Mater. Soc.*, vol. 43, no. 8, p. 7, 1991.

[54] M. S. Zedalis, J. D. Bryant, P. S. Gilman, and S. K. Das, “High-temperature discontinuously reinforced aluminum,” *JOM*, vol. 43, no. 8, pp. 29–31, 1991.

[55] G. Bockstiegel and O. Svensson, “INFLUENCE OF LUBRICATION, DIE MATERIAL AND TOOL DESIGN UPON DIE-WEAR IN THE COMPACTING OF IRON POWDERS,” 1971.

[56] J. Z. Wang, X. H. Qu, H. Q. Yin, M. J. Yi, and X. J. Yuan, “High velocity compaction of ferrous powder,” *Powder Technol.*, vol. 192, no. 1, pp. 131–136, 2009.

[57] J. Robertson, J.-T. Im, I. Karaman, K. T. Hartwig, and I. E. Anderson, “Consolidation of amorphous copper based powder by equal channel angular extrusion,” *J. Non. Cryst. Solids*, vol. 317, no. 1–2, pp. 144–151, 2003.

[58] J. Duszczyk and D. Bialo, “The compaction of metal powders in rotary die pressing,” *Powder Met. Int.*, vol. 11, no. 3, pp. 103–105, 1979.

[59] G. B. Schaffer, T. B. Sercombe, and R. N. Lumley, “Liquid phase sintering of aluminium alloys,” *Mater. Chem. Phys.*, vol. 67, no. 1–3, pp. 85–91, 2001.

[60] M. L. Delgado, E. M. Ruiz-Navas, E. Gordo, and J. M. Torralba, “Enhancement of liquid phase sintering through Al–Si additions to Al–Cu systems,” *J. Mater. Process. Technol.*, vol. 162, pp. 280–285, 2005.

[61] J. M. Martín and F. Castro, “Liquid phase sintering of P/M aluminium alloys: effect of processing conditions,” *J. Mater. Process. Technol.*, vol. 143, pp. 814–821, 2003.

[62] M. Gagné, “Behavior of powder mix constituents during cold and warm compaction,”

Adv. Powder Metall. Part. Mater., vol. 1, p. 3, 1997.

[63] J. Chmelar, B. Nelson, H. Rutz, and M. Lutz, "An evaluation of the AncorDense single compaction process and HPP processing techniques on fine pitched spur and helical gears," in *1994 International Conference and Exhibition on Powder Metallurgy and Particulate Materials*, 1994, pp. 73–88.

[64] T. Miller and F. Hanejko, "Development of a Warm Compacted Automatic Transmission Torque Converter Hub," 1997.

[65] H. S. Kim, "Yield and compaction behavior of rapidly solidified Al–Si alloy powders," *Mater. Sci. Eng. A*, vol. 251, no. 1–2, pp. 100–105, 1998.

[66] H. V Atkinson, P. Kapranos, D. Liu, S. A. Chayong, and D. H. Kirkwood, "Thixoforming of normally wrought aluminium alloys," in *Materials Science Forum*, 2002, vol. 396, pp. 131–136.

[67] G. A. Kosnikov, O. L. Figovsky, and A. S. Eldarkhanov, "Liquid phase production technologies of metal matrix composites," *Int. Lett. Chem. Phys. Astron.*, vol. 6, 2014.

[68] X. Zhang, T. Chen, H. Qin, and C. Wang, "A comparative study on permanent mold cast and powder thixoforming 6061 aluminum alloy and SiCp/6061Al composite: Microstructures and mechanical properties," *Materials (Basel).*, vol. 9, no. 6, p. 407, 2016.

[69] O. C. Ferrel and G. Hirt, *Business: A changing world*. Tata McGraw-Hill Education, 2000.

[70] M. Garat, S. JACOB, L. MAENNER, and C. SZTUR, "Etat de l'art du thixomoulage dans le monde," *Hommes et fonderie*, no. 309, pp. 12–17, 2000.

[71] Y. Wu, G.-Y. Kim, I. E. Anderson, and T. A. Lograsso, "Fabrication of Al6061 composite with high SiC particle loading by semi-solid powder processing," *Acta Mater.*, vol. 58, no. 13, pp. 4398–4405, 2010.

[72] A. Bolouri and C.-G. Kang, "Thixoforging of wrought aluminum thin plates with microchannels," *Metall. Mater. Trans. A*, vol. 45, no. 5, pp. 2575–2589, 2014.

[73] K. Lange, "Handbook of metal forming," *McGraw-Hill B. Company, 1985*, p. 1216, 1985.

[74] M. Kiuchi, S. Sugiyama, and K. Arai, “Study of Metal Forming in the Mashy State 2nd Report: Extrusion of Tube, Bar and Wire of Alloys in Mashy State,” in *Proceedings of the Twentieth International Machine Tool Design and Research Conference*, 1980, pp. 79–86.

[75] M. Kiuchi and S. Sugiyama, “A new method to detect solid fractions of mushy/semi-solid metals and alloys,” *CIRP Ann.*, vol. 43, no. 1, pp. 271–274, 1994.

[76] M. Ketabchi, M. Amin Shafaat, I. Shafaat, and M. Abbasi, “Effect of cooling rate on mechanical properties of 7075 aluminum rods extruded in semisolid state,” *J. Eng. Mater. Technol.*, vol. 136, no. 2, p. 21002, 2014.

[77] A. Neag, V. Favier, M. Pop, E. Becker, and R. Bigot, “Effect of experimental conditions on 7075 aluminium response during thixoextrusion,” in *Key Engineering Materials*, 2012, vol. 504, pp. 345–350.

[78] A. Neag, V. Favier, R. Bigot, and D. Frunză, “Study on thixo-extrusion of semi-solid aluminium,” in *Solid State Phenomena*, 2008, vol. 141, pp. 659–664.

[79] Z. Dazhi, L. Guimin, and C. Jianzhong, “Semi-solid extrusion of aluminum alloy ZL116,” 中国铸造, 2008.

[80] G. P. Simpson and T. J. Culkin, “Laser cutting,” *ASM Handbook.*, vol. 14, pp. 735–742, 1988.

[81] K. Laue and H. Stenger, “Extrusion, American society for metals,” *Met. Park. Ohio*, 1981.

[82] S. L. Semiatin, *Metalworking: bulk forming*, vol. 14. Asm International, 2005.

[83] T. Sheppard, “Temperature and speed effects in hot extrusion of aluminium alloys,” *Met. Technol.*, vol. 8, no. 1, pp. 130–141, 1981.

[84] T. Sheppard, “Extrusion of Aluminium Alloys”, Kluwer Academic Publishers, The Netherlands, pp. 220,” 1999.

[85] C. E. Pearson and R. N. Parkins, *The extrusion of metals*. Chapman & Hall, 1960.

[86] C. P. Hinesley and H. Conrad, “Effects of temperature and ram speed on the flow pattern in axisymmetric extrusions of 2024 Al alloy,” *Mater. Sci. Eng.*, vol. 12, no. 1,

pp. 47–58, 1973.

[87] S. Sohrabpour, A. H. Shabaik, and E. G. Thomsen, “Local friction coefficients in axisymmetric extrusions of aluminum,” 1970.

[88] Z. Zimerman and B. Avitzur, “Metal flow through conical converging dies—a lower upper bound approach using generalized boundaries of the plastic zone,” 1970.

[89] H. W. L. Phillips, *Annotated equilibrium diagrams of some aluminium alloy systems*, no. 25. Institute of metals, 1959.

[90] T. Sheppard, “Homogenization and extrusion conditions for specific alloys,” in *Extrusion of Aluminium Alloys*, Springer, 1999, pp. 205–252.

[91] S. J. Paterson and T. Sheppard, “Structural changes occurring during thermal treatments during extrusion of Al–Cu–Mg–Mn–Si (AA 2014) alloy,” *Met. Technol.*, vol. 9, no. 1, pp. 389–398, 1982.

[92] T. Nakamura, “Steady State Deformation and Dynamic Restoration Processes During High Strain Rate and High Temperature Deformation in Metals and Alloys,” in *High Velocity Deformation of Solids*, Springer, 1979, pp. 108–119.

[93] G. Scharf, D. Achenbach, and W. Gruhl, “Beeinflussung der Grobkornbildung bei Preßprofilen aus Aluminiumlegierungen,” *Int. J. Mater. Res.*, vol. 60, no. 6, pp. 515–520, 1969.

[94] W. Gruhl and H. Cordier, “Das Spannungsrißkorrosionsverhalten der AlZnMg-Legierungen,” *Aluminium*, vol. 44, pp. 403–411, 1968.

[95] J. Zasadzinski, W. Libura, J. Richert, and W. Z. Misiolek, “Modeling of temperature-speed parameters in aluminum extrusion,” *Light Met. age*, vol. 50, no. 7–8, pp. 60–64, 1992.

[96] P. Venugopal, S. Venkatraman, R. Vasudevan, and K. A. Padmanabhan, “Some failure studies in the hooker extrusion of sintered iron powder metallurgical preforms,” *J. Mech. Work. Technol.*, vol. 16, no. 2, pp. 165–174, 1988.

[97] S. O. Onuh, M. Ekoja, and M. B. Adeyemi, “Effects of die geometry and extrusion speed on the cold extrusion of aluminium and lead alloys,” *J. Mater. Process. Technol.*, vol. 132, no. 1–3, pp. 274–285, 2003.

[98] J. S. Ajiboye and M. B. Adeyemi, “Effects of die land on the cold extrusion of lead alloy,” *J. Mater. Process. Technol.*, vol. 171, no. 3, pp. 428–436, 2006.

[99] P. Tiernan and B. Draganescu, “Statistical modelling of surface hardness and roughness in cold extrusion of aluminium,” *Int. J. Manuf. Res.*, vol. 3, no. 4, pp. 452–470, 2008.

[100] M. Shahzad and L. Wagner, “Influence of extrusion parameters on microstructure and texture developments, and their effects on mechanical properties of the magnesium alloy AZ80,” *Mater. Sci. Eng. A*, vol. 506, no. 1–2, pp. 141–147, 2009.

[101] R. Das, U. S. Dixit, and S. Deb, “Effect of Extrusion Ratio, Die Land Length and Lubrication on Hardness and Surface Roughness in Multi-Hole Extrusion,” *J. Manuf. Technol. Res.*, vol. 4, no. 1/2, p. 35, 2012.

[102] G. Huang, X. Guo, Y. Han, L. Wang, W. Lu, and D. Zhang, “Effect of extrusion dies angle on the microstructure and properties of (TiB+ TiC)/Ti6Al4V in situ titanium matrix composite,” *Mater. Sci. Eng. A*, vol. 667, pp. 317–325, 2016.

[103] M. M. Peres *et al.*, “Hot extrusion of nanostructured Al alloy powder: extrusion ratio and temperature effect on the microstructure and mechanical properties,” in *Materials Science Forum*, 2008, vol. 570, pp. 91–96.

[104] C. Zhang, G. Zhao, Z. Chen, H. Chen, and F. Kou, “Effect of extrusion stem speed on extrusion process for a hollow aluminum profile,” *Mater. Sci. Eng. B*, vol. 177, no. 19, pp. 1691–1697, 2012.

[105] Z. Z. Chen, Z. L. Lou, and X. Y. Ruan, “Finite volume simulation and mould optimization of aluminum profile extrusion,” *J. Mater. Process. Technol.*, vol. 190, no. 1–3, pp. 382–386, 2007.

[106] R. N. Lumley, J. Buha, I. J. Polmear, A. J. Morton, and A. Crosky, “Secondary precipitation in aluminium alloys & its role in modern heat treatment,” in *Materials science forum*, 2006, vol. 519, pp. 283–290.

[107] M. F. Ashby, “A. Kelly and RB Nicholson Strengthening Methods in Crystals. 1971, 137 Amsterdam.” Elsevier Publishing Co.

[108] P. A. Flinn, “Strengthening Mechanisms in Solids,” *ASM, Met. Park. Ohio*, p. 17, 1962.

[109] R. W. Armstrong and T. N. Baker, “Yield, flow and fracture of polycrystals,” *ed. TN Bak. Appl. Sci. Publ. UK*, vol. 2, 1983.

[110] R. N. Wright and M. S. Paulson, “Constitutive equation development for high strain deformation processing of aluminum alloys,” *J. Mater. Process. Technol.*, vol. 80, pp. 556–559, 1998.

[111] X. G. Fan and H. Yang, “Internal-state-variable based self-consistent constitutive modeling for hot working of two-phase titanium alloys coupling microstructure evolution,” *Int. J. Plast.*, vol. 27, no. 11, pp. 1833–1852, 2011.

[112] C. Junhui, Y. He, S. Zhichao, L. Hongwei, L. Zhijun, and S. Changwu, “Flow behavior and constitutive model using piecewise function of strain for TC11 alloy,” *Rare Met. Mater. Eng.*, vol. 41, no. 3, pp. 397–401, 2012.

[113] M. Zhan *et al.*, “A method for establishing the plastic constitutive relationship of the weld bead and heat-affected zone of welded tubes based on the rule of mixtures and a microhardness test,” *Mater. Sci. Eng. A*, vol. 527, no. 12, pp. 2864–2874, 2010.

[114] M. R. Rokni, A. Zarei-Hanzaki, A. A. Roostaei, and A. Abolhasani, “Constitutive base analysis of a 7075 aluminum alloy during hot compression testing,” *Mater. Des.*, vol. 32, no. 10, pp. 4955–4960, 2011.

[115] Z. Zeng, S. Jonsson, and Y. Zhang, “Constitutive equations for pure titanium at elevated temperatures,” *Mater. Sci. Eng. A*, vol. 505, no. 1–2, pp. 116–119, 2009.

[116] C. M. Sellars and W. J. McTegart, “On the mechanism of hot deformation,” *Acta Metall.*, vol. 14, no. 9, pp. 1136–1138, 1966.

[117] X. Huang, H. Zhang, Y. Han, W. Wu, and J. Chen, “Hot deformation behavior of 2026 aluminum alloy during compression at elevated temperature,” *Mater. Sci. Eng. A*, vol. 527, no. 3, pp. 485–490, 2010.

[118] D. W. Wolla, M. J. Davidson, and A. K. Khanra, “Constitutive modeling of powder metallurgy processed Al–4% Cu preforms during compression at elevated temperature,” *Mater. Des.*, vol. 65, pp. 83–93, 2015.

[119] S. Liu, J. You, X. Zhang, Y. Deng, and Y. Yuan, “Influence of cooling rate after homogenization on the flow behavior of aluminum alloy 7050 under hot compression,” *Mater. Sci. Eng. A*, vol. 527, no. 4–5, pp. 1200–1205, 2010.

[120] S. Serajzadeh, “A mathematical model for evolution of flow stress during hot deformation,” *Mater. Lett.*, vol. 59, no. 26, pp. 3319–3324, 2005.

[121] J. Wang, J. Chen, Z. Zhao, and X. Ruan, “Hot deformation behavior and flow stress model of F40MnV steel,” *J. Cent. South Univ. Technol.*, vol. 14, no. 1, pp. 19–23, 2007.

[122] X.-S. Li, L. Wu, C. Jun, and H.-B. Zhang, “New approach for modeling flow stress of aluminum alloy 6A10 considering temperature variation,” *Trans. Nonferrous Met. Soc. China*, vol. 20, no. 8, pp. 1482–1487, 2010.

[123] M. A. J. Taleghani, E. M. R. Navas, M. Salehi, and J. M. Torralba, “Hot deformation behaviour and flow stress prediction of 7075 aluminium alloy powder compacts during compression at elevated temperatures,” *Mater. Sci. Eng. A*, vol. 534, pp. 624–631, 2012.

[124] S. Chen, K. Chen, G. Peng, and J. I. A. Le, “Effect of initial microstructure on hot workability of 7085 aluminum alloy,” *Trans. Nonferrous Met. Soc. China*, vol. 23, no. 4, pp. 956–963, 2013.

[125] J. Li, S. Jian, X. Yan, B. Mao, and L. Yan, “Microstructure evolution of 7050 aluminum alloy during hot deformation,” *Trans. Nonferrous Met. Soc. China*, vol. 20, no. 2, pp. 189–194, 2010.

[126] Y. Y. Zong, D. B. Shan, and Z. Shi, “Study on hot deformation behaviour and constitutive equation of 4032 Al alloy,” *Mater. Res. Innov.*, vol. 15, no. sup1, pp. s470–s474, 2011.

[127] Y. Deng, Z. Yin, and J. Huang, “Hot deformation behavior and microstructural evolution of homogenized 7050 aluminum alloy during compression at elevated temperature,” *Mater. Sci. Eng. A*, vol. 528, no. 3, pp. 1780–1786, 2011.

[128] J. J. Fisher Jr, L. S. Kramer, and J. R. Pickens, “Aluminum alloy 2519 in military vehicles,” *Adv. Mater. Process.*, vol. 160, no. 9, pp. 43–47, 2002.

[129] L. Kramer, T. P. Blair, S. D. Blough, J. J. Fisher, and J. R. Pickens, “Stress-corrosion cracking susceptibility of various product forms of aluminum alloy 2519,” *J. Mater. Eng. Perform.*, vol. 11, no. 6, pp. 645–650, 2002.

[130] H. Li, X. Liang, F. Li, F.-F. Guo, L. I. Zhou, and X.-M. Zhang, “Effect of Y content on

microstructure and mechanical properties of 2519 aluminum alloy," *Trans. Nonferrous Met. Soc. China*, vol. 17, no. 6, pp. 1194–1198, 2007.

[131] Z. Yang, Y. C. Guo, J. P. Li, F. He, F. Xia, and M. X. Liang, "Plastic deformation and dynamic recrystallization behaviors of Mg–5Gd–4Y–0.5 Zn–0.5 Zr alloy," *Mater. Sci. Eng. A*, vol. 485, no. 1–2, pp. 487–491, 2008.

[132] M. L. Wang, P. P. Jin, J. H. Wang, and L. Han, "Characterization of the Hot Deformation Behavior of a Al-Si Alloy Using Processing Maps," in *Advanced Materials Research*, 2014, vol. 873, pp. 3–9.

[133] D. Odoh, Y. Mahmoodkhani, and M. Wells, "Effect of alloy composition on hot deformation behavior of some Al-Mg-Si alloys," *Vacuum*, vol. 149, pp. 248–255, 2018.

[134] Ø. Grong and H. R. Shercliff, "Microstructural modelling in metals processing," *Prog. Mater. Sci.*, vol. 47, no. 2, pp. 163–282, 2002.

[135] H. Grass, C. Krempaszky, T. Reip, and E. Werner, "3-D Simulation of hot forming and microstructure evolution," *Comput. Mater. Sci.*, vol. 28, no. 3–4, pp. 469–477, 2003.

[136] N. Bontcheva, G. Petzov, and L. Parashkevova, "Thermomechanical modelling of hot extrusion of Al-alloys, followed by cooling on the press," *Comput. Mater. Sci.*, vol. 38, no. 1, pp. 83–89, 2006.

[137] F. J. Humphreys and M. Hatherly, *Recrystallization and related annealing phenomena*. Elsevier, 2012.

[138] H. R. Shercliff and A. M. Lovatt, "Modelling of microstructure evolution in hot deformation," *Philos. Trans. R. Soc. London. Ser. A Math. Phys. Eng. Sci.*, vol. 357, no. 1756, pp. 1621–1643, 1999.

[139] D.-W. Suh, S.-Y. Lee, K.-H. Lee, S.-K. Lim, and K. H. Oh, "Microstructural evolution of Al–Zn–Mg–Cu–(Sc) alloy during hot extrusion and heat treatments," *J. Mater. Process. Technol.*, vol. 155, pp. 1330–1336, 2004.

[140] L. De Pari Jr and W. Z. Misiolek, "Theoretical predictions and experimental verification of surface grain structure evolution for AA6061 during hot rolling," *Acta Mater.*, vol. 56, no. 20, pp. 6174–6185, 2008.

[141] W. Z. Misiolek and W. R. Van Geertruyden, “Combined numerical simulation and microstructure characterization for prediction of physical properties in extruded aluminum alloys,” in *Key Engineering Materials*, 2010, vol. 424, pp. 1–8.

[142] W. H. Van Geertruyden, H. M. Browne, W. Z. Misiolek, and P. T. Wang, “Evolution of surface recrystallization during indirect extrusion of 6xxx aluminum alloys,” *Metall. Mater. Trans. A*, vol. 36, no. 4, pp. 1049–1056, 2005.

[143] Z. Peng and T. Sheppard, “Individual influence of forming parameters on surface recrystallization during aluminium extrusion,” *Model. Simul. Mater. Sci. Eng.*, vol. 12, no. 1, p. 43, 2003.

[144] X. Duan and T. Sheppard, “Simulation and control of microstructure evolution during hot extrusion of hard aluminium alloys,” *Mater. Sci. Eng. A*, vol. 351, no. 1–2, pp. 282–292, 2003.

[145] M. Schikorra, L. Donati, L. Tomesani, and A. E. Tekkaya, “Microstructure analysis of aluminum extrusion: grain size distribution in AA6060, AA6082 and AA7075 alloys,” *J. Mech. Sci. Technol.*, vol. 21, no. 10, pp. 1445–1451, 2007.

[146] L. Donati, A. Segatori, M. El Mehtedi, and L. Tomesani, “Grain evolution analysis and experimental validation in the extrusion of 6XXX alloys by use of a lagrangian FE code,” *Int. J. Plast.*, vol. 46, pp. 70–81, 2013.

[147] Y. Y. Zong, L. Chen, Z. G. Zhao, and D. B. Shan, “Flow lines, microstructure, and mechanical properties of flow control formed 4032 aluminum alloy,” *Mater. Manuf. Process.*, vol. 29, no. 4, pp. 466–471, 2014.

[148] W. W. Ren, C. G. Xu, X. L. Chen, and S. X. Qin, “Microstructure and critical strain of dynamic recrystallization of 6082 aluminum alloy in thermal deformation,” in *IOP Conference Series: Materials Science and Engineering*, 2018, vol. 369, no. 1, p. 12022.

[149] C. De Boor and G. J. Fix, “Spline approximation by quasiinterpolants,” *J. Approx. Theory*, vol. 8, no. 1, pp. 19–45, 1973.

[150] Y.-S. Jang, D.-C. Ko, and B.-M. Kim, “Application of the finite element method to predict microstructure evolution in the hot forging of steel,” *J. Mater. Process. Technol.*, vol. 101, no. 1–3, pp. 85–94, 2000.

[151] N. Bontcheva and G. Petzov, “Microstructure evolution during metal forming processes,” *Comput. Mater. Sci.*, vol. 28, no. 3–4, pp. 563–573, 2003.

[152] R. Kuziak, M. Glowacki, and M. Pietrzyk, “Modelling of plastic flow, heat transfer and microstructural evolution during rolling of eutectoid steel rods,” *J. Mater. Process. Technol.*, vol. 60, no. 1–4, pp. 589–596, 1996.

[153] N. Bontcheva and G. Petzov, “Total simulation model of the thermo-mechanical process in shape rolling of steel rods,” *Comput. Mater. Sci.*, vol. 34, no. 4, pp. 377–388, 2005.

[154] E. Nes and T. Furu, “Application of microstructurally based constitutive laws to hot deformation of aluminium alloys,” *Scr. Metall. Mater.*, vol. 33, no. 1, 1995.

[155] E. D. Sweet, S. K. Caraher, N. V Danilova, and X. Zhang, “Effects of extrusion parameters on coarse grain surface layer in 6xxx series extrusions,” in *Proceedings of the Eighth International Aluminum Extrusion Technology Seminar*, 2004, vol. 1, pp. 115–126.

[156] S. R. Claves, W. Z. Misiolek, and R. M. Kelly, “Effect of Die Design on microstructure of Extruded Aluminum,” in *PROCEEDINGS OF INTERNATIONAL ALUMINUM EXTRUSION TECHNOLOGY SEMINAR*, 2000, vol. 1, pp. 225–232.

[157] H. Ahmed, M. A. Wells, D. M. Maijer, B. J. Howes, and M. R. Van Der Winden, “Modelling of microstructure evolution during hot rolling of AA5083 using an internal state variable approach integrated into an FE model,” *Mater. Sci. Eng. A*, vol. 390, no. 1–2, pp. 278–290, 2005.

[158] L. Deng, X. Y. Wang, J. C. Xia, and H. T. Guo, “Microstructural Modeling and Simulation of Al-2.8 Cu-1.4 Li Alloy during Elevated Temperature Deformation,” *Metall. Mater. Trans. A*, vol. 42, no. 8, pp. 2509–2515, 2011.

[159] T. Ishikawa, H. Sano, Y. Yoshida, N. Yukawa, J. Sakamoto, and Y. Tozawa, “Effect of extrusion conditions on metal flow and microstructures of aluminum alloys,” *CIRP Ann.*, vol. 55, no. 1, pp. 275–278, 2006.

[160] X. Duan, X. Velay, and T. Sheppard, “Application of finite element method in the hot extrusion of aluminium alloys,” *Mater. Sci. Eng. A*, vol. 369, no. 1–2, pp. 66–75, 2004.

[161] M. M. Marín, A. M. Camacho, and J. A. Pérez, “Influence of the temperature on

AA6061 aluminum alloy in a hot extrusion process," *Procedia Manuf.*, vol. 13, pp. 327–334, 2017.

[162] L. F. Mondolfo, "Aluminum Alloys: Structure and Properties. London: Butter Worths." Boston Press, 1976.

[163] A. Campbell, P. Murray, E. Yakushina, S. Marshall, and W. Ion, "New methods for automatic quantification of microstructural features using digital image processing," *Mater. Des.*, vol. 141, pp. 395–406, 2018.

[164] Q. D. Sun, S. F. Gao, J. W. Huang, and W. Chen, "Metallographical image segmentation and compression," in *Applied Mechanics and Materials*, 2012, vol. 152, pp. 276–280.

[165] J. Gola *et al.*, "Advanced microstructure classification by data mining methods," *Comput. Mater. Sci.*, vol. 148, pp. 324–335, 2018.

[166] V. H. C. de Albuquerque, A. R. de Alexandria, P. C. Cortez, and J. M. R. S. Tavares, "Evaluation of multilayer perceptron and self-organizing map neural network topologies applied on microstructure segmentation from metallographic images," *NDT E Int.*, vol. 42, no. 7, pp. 644–651, 2009.

[167] V. H. C. de Albuquerque, C. C. Silva, T. I. de S. Menezes, J. P. Farias, and J. M. R. S. Tavares, "Automatic evaluation of nickel alloy secondary phases from SEM images," *Microsc. Res. Tech.*, vol. 74, no. 1, pp. 36–46, 2011.

[168] O. Chapelle, B. Scholkopf, and A. Zien, "Semi-supervised learning (chapelle, o. et al., eds.; 2006)[book reviews]," *IEEE Trans. Neural Networks*, vol. 20, no. 3, p. 542, 2009.

[169] Z. Qiu, K. Sugio, and G. Sasaki, "Classification of Microstructures of Al–Si Casting Alloy in Different Cooling Rates with Machine Learning Technique," *Mater. Trans.*, p. MT-MBW2020002, 2021.

[170] D. Chen, P. Zhang, S. Liu, Y. Chen, and W. Zhao, "Aluminum alloy microstructural segmentation in micrograph with hierarchical parameter transfer learning method," *J. Electron. Imaging*, vol. 28, no. 5, p. 53018, 2019.

[171] D. Chen, D. Guo, S. Liu, and F. Liu, "Microstructure instance segmentation from aluminum alloy metallographic image using different loss functions," *Symmetry*

(Basel)., vol. 12, no. 4, p. 639, 2020.

[172] J. Fluhrer, "DEFORM (TM) 2D Version 8.1 User's Manual," *Sci. Form. Technol. Corp. Columbus, Ohio*, 2015.

[173] C. FRANCISCO, H. R. R. HERNANDEZ, J. MARTIN, and R. MACKAY, *AL-SI ALLOYS: Automotive, Aeronautical, and Aerospace Applications*. SPRINGER, 2019.

[174] M. Campillo, M. T. Baile, S. Menargues, E. Martín, and A. Forn, "A357 Aluminium Cast Alloys for Extrusion Processes," in *Solid State Phenomena*, 2013, vol. 192, pp. 454–459.

[175] A. Forn *et al.*, "Thixoextrusion of A357 aluminium alloy," *Trans. Nonferrous Met. Soc. China*, vol. 20, pp. s1005–s1009, 2010.

[176] Y. Birol, E. A. Guven, and L. J. Capan, "Extrusion of EN AW-2014 alloy in semisolid state," *Mater. Sci. Technol.*, vol. 27, no. 12, pp. 1851–1857, 2011.

[177] Q. G. Wang and C. J. Davidson, "Solidification and precipitation behaviour of Al-Si-Mg casting alloys," *J. Mater. Sci.*, vol. 36, no. 3, pp. 739–750, 2001.

[178] L. Hengcheng, S. Yu, and S. Guoxiong, "Restraining effect of strontium on the crystallization of Mg2Si phase during solidification in Al–Si–Mg casting alloys and mechanisms," *Mater. Sci. Eng. A*, vol. 358, no. 1–2, pp. 164–170, 2003.

[179] K.-Y. Wang *et al.*, "Improving microstructure and mechanical properties of hypoeutectic Al-Mg2Si alloy by Gd addition," *J. Alloys Compd.*, vol. 813, p. 152178, 2020.

[180] C. M. Sellars and J. A. Whiteman, "Recrystallization and grain growth in hot rolling," *Met. Sci.*, vol. 13, no. 3–4, pp. 187–194, 1979.

[181] H. Mirzadeh and A. Najafizadeh, "Prediction of the critical conditions for initiation of dynamic recrystallization," *Mater. Des.*, vol. 31, no. 3, pp. 1174–1179, 2010.

[182] P. EI and J. JJ, "Critical strain for dynamic recrystallization in variable strain rate hot deformation," *Isij Int.*, vol. 43, no. 5, pp. 692–700, 2003.

[183] L. Donati, J. S. Dzwonczyk, J. Zhou, and L. Tomesani, "Microstructure prediction of hot-deformed aluminium alloys," in *Key Engineering Materials*, 2008, vol. 367, pp. 107–116.

[184] F. Yin, L. Hua, H. Mao, X. Han, D. Qian, and R. Zhang, “Microstructural modeling and simulation for GCr15 steel during elevated temperature deformation,” *Mater. Des.*, vol. 55, pp. 560–573, 2014.

[185] A. L. M. Costa, H. S. Valberg, and W. Z. Misiolek, “Scale Effect in FEM Simulation of Axisymmetric Hot Micro-Extrusion of Aluminum Alloys,” in *ASME International Mechanical Engineering Congress and Exposition*, 2016, vol. 50688, p. V014T11A029.

[186] M. Yıldırım and D. Özyürek, “The effects of Mg amount on the microstructure and mechanical properties of Al–Si–Mg alloys,” *Mater. Des.*, vol. 51, pp. 767–774, 2013.

[187] E. Sjölander and S. Seifeddine, “The heat treatment of Al–Si–Cu–Mg casting alloys,” *J. Mater. Process. Technol.*, vol. 210, no. 10, pp. 1249–1259, 2010.

[188] X. Xu, Z. Yang, Y. Ye, G. Wang, and X. He, “Effects of various Mg/Si ratios on microstructure and performance property of Al-Mg-Si alloy cables,” *Mater. Charact.*, vol. 119, pp. 114–119, 2016.

[189] V. Vijeesh and K. N. Prabhu, “Computer aided cooling curve analysis and microstructure of cerium added hypereutectic Al–Si (LM29) alloy,” *Trans. Indian Inst. Met.*, vol. 67, no. 4, pp. 541–549, 2014.

[190] S. Nafisi, D. Emadi, and R. Ghomashchi, “Impact of Mg addition on solidification behaviour of Al–7% Si alloy,” *Mater. Sci. Technol.*, vol. 24, no. 6, pp. 718–724, 2008.

[191] A. K. Gupta, D. J. Lloyd, and S. A. Court, “Precipitation hardening in Al–Mg–Si alloys with and without excess Si,” *Mater. Sci. Eng. A*, vol. 316, no. 1–2, pp. 11–17, 2001.

[192] B. J. Kim, S. S. Jung, J. H. Hwang, Y. H. Park, and Y. C. Lee, “Effect of eutectic Mg2Si phase modification on the mechanical properties of Al-8Zn-6Si-4Mg-2Cu cast alloy,” *Metals (Basel).*, vol. 9, no. 1, p. 32, 2019.

[193] C. H. Caceres, C. J. Davidson, J. R. Griffiths, and Q. G. Wang, “The effect of Mg on the microstructure and mechanical behavior of Al-Si-Mg casting alloys,” *Metall. Mater. Trans. A*, vol. 30, no. 10, pp. 2611–2618, 1999.

[194] B. Baradarani and R. Raiszadeh, “Precipitation hardening of cast Zr-containing A356 aluminium alloy,” *Mater. Des.*, vol. 32, no. 2, pp. 935–940, 2011.

[195] Q. Li, B. Li, J. Li, T. Xia, Y. Lan, and T. Guo, “Effects of the addition of Mg on the microstructure and mechanical properties of hypoeutectic Al–7% Si alloy,” *Int. J. Met.*, vol. 11, no. 4, pp. 823–830, 2017.

[196] K. Yamamoto *et al.*, “Effect of Mg content on age-hardening response, tensile properties, and microstructures of a T5-treated thixo-cast hypoeutectic Al–Si alloy,” *Mater. Sci. Eng. A*, vol. 798, p. 140089, 2020.

Research Outcomes

1) Abeyram M Nithin, M. J. Davidson, C.S.P Rao **“*Mechanical and Metallurgical Studies on Thixoextruded Al-Si alloys*”** Published in Journal of Materials Engineering and Performance, September 2020 29(6378–6389) (SCI IF=1.5) DOI 10.1007/s11665-020-05143-8.

2) Abeyram M Nithin, M. J. Davidson, C.S.P Rao "***Microstructure Modeling of sintered Al-4Si-0.6Mg alloy extruded at semisolid temperature ranges*****"** Published in Part E**:** Journal of Process Mechanical Engineering, September 2021 (SCI IF=1.49) DOI 10.1177/09544089211042484

3) Abeyram M Nithin, M. J. Davidson, C.S.P Rao "***Effect of various Mg/Si ratio on microstructure, structural properties on thixoextruded Al-Si- Mg alloys"*** Silicon (accepted)